OPTIMIZING FUTURE CMB OBSERVATORIES AND MEASURING GALAXY CLUSTER MOTIONS WITH THE ATACAMA COSMOLOGY TELESCOPE

A Dissertation

Presented to the Faculty of the Graduate School

of Cornell University

in Partial Fulfillment of the Requirements for the Degree of

Doctor of Philosophy

by

Patricio Andres Gallardo Matamala

December 2019

OPTIMIZING FUTURE CMB OBSERVATORIES AND MEASURING GALAXY CLUSTER MOTIONS WITH THE ATACAMA COSMOLOGY TELESCOPE

Patricio Andres Gallardo Matamala , Ph.D.

Cornell University 2019

Cosmic Microwave Background (CMB) experiments are a great tool to probe the universe's history and content. In the recent decade, great progress in large format detector array technologies has allowed increased sensitivity and sky coverage, which has enabled very precise measurements. The next generation of CMB experiments will offer larger focal planes, which will allow measurements with exquisite precision. In this thesis, the following studies are presented:

The development of a silicon meta-material deep reactive ion etched anti-reflection coating for use in sub-millimeter wavelengths.

Characterization of the aliased detector noise performance of the Atacama Cosmology Telescope (ACT), a current polarization sensitive six-meter telescope that observes the CMB at arcminute resolution.

Optical models developed to describe the pickup and sidelobes characteristics of the ACT. These models are currently being used to optimize the design of the Simons Observatory, a next generation six-meter telescope with increased sensitivity.

Studies of the motions of clusters of galaxies via the pairwise kinetic Sunyaev-Zeldovich effect (the frequency-distortion of the cold CMB light due to the interaction with the hot inter-cluster ionized gas), with data from ACT.

BIOGRAPHICAL SKETCH

Patricio Gallardo is an experimental physicist who works on cosmology. He grew up in Quinta Normal, Santiago, Chile and went to Universidad Católica de Chile for college to study Electrical Engineering. There he fulfilled an additional major in Astronomy graduating from both majors in 2011. In his undergraduate thesis he studied the optics of the Atacama Cosmology Telescope and experimentally probed its spillover and sidelobes. In 2012 he worked at the University of Pennsylvania building the first polarimeter array for ACT, ACTPol. Then he moved to the high Atacama Desert in northern Chile to be part of the team that installed the receiver in the telescope which saw first light later that year.

In 2013 he started his PhD studies at Cornell University, where he developed an micron scale anti-reflection coating for sub-millimeter silicon optics which will be used in the CCAT-prime telescope, characterized the noise properties of the new Advanced ACTPol instrument to optimize its sensitivity, modeled the sidelobe response of the Atacama Cosmology Telescope and studied the motions of galaxy clusters, the largest gravitationally bound objects in the universe, using the kinetic Sunyaev-Zeldovich effect with data from ACTPol.

To my parents.

I miss you immensely.

To my sister.

Who always supported me.

To Alexandra.

Who married me.

ACKNOWLEDGEMENTS

Writing an acknowledgments section is risky business. The author runs the risk of missing people who discretely played an important role. For the sake of brevity I will bound my acknowledgments to the people I interacted most frequently with. I almost certainly will miss someone inadvertently.

I am indebted to my advisor Michael Niemack for trusting in my talent and helping me develop the skills needed for the work presented here. I thank useful comments from my graduate committee members Rachel Bean and Julia Thom-Levy.

From our lab at Cornell I thank Nick Cothard for continuing our work on anti-reflection coatings and expanding it to the use in conjunction with metal-mesh filters, Francesco de Bernardis for his work in the pairwise kSZ effect, Cody Duell for his interest on time domain astronomy with ACT, Shawn Henderson for his restless work on TES readout, Brian Koopman for useful discussions on telescope optics and Eve Vavagiakis for her work on the Sunyaev-Zeldovich effects.

From outside our lab at Cornell, the work presented here received useful input from Nicholas Battaglia, Victoria Calafut, Simon Dicker, Jon Gudmundsson, Patty Ho, Michele Limon, Marius Lungu, Jeff McMahon, Sigurd Naess, Lyman Page, Roberto Pudu, Sara Simon, Bob Thornton and Ed Wollack .

All the people mentioned in this page in one way or another made the work presented here better. For the mistakes, oversights and wrong assumptions, I take full blame.

TABLE OF CONTENTS

LIST OF TABLES

LIST OF FIGURES

PREFACE

In science, and in particular in physics we live exciting times. Humankind has never produced so much knowledge as we are producing today. I have been fortunate enough to be a graduate student when two of the most important discoveries of the century have been reported. The detection of gravitational waves [11] and the first reported image of a black hole [4]. However, despite our great advances, great problems still seem frustratingly elusive in the field of physics. What is dark matter? What is dark energy? How can we detect them directly? What kind of field caused inflation? What is the neutrino's mass?. Throughout observation experimental cosmologists have a chance to shine some light into these questions (and undoubtedly open new ones). I have the privilege of contributing with my work to teams of scientists that are working to figure these and other questions out. In the following pages I summarize what I have worked on for six years to join a collective of scientists planning and building the next generation of ground based cosmic microwave background experiments.

CHAPTER 1

INTRODUCTION

1.1 A brief description of our Universe's History

Our current cosmological model has been built with evidence from many sources. Here I give a brief summary. I mostly base this discussion on [17, 39, 57].

1.1.1 The expanding universe

The discovery of the Cosmic Microwave Background is one of the foundational stones on which our scientific cosmological understanding rests. In 1965 Arno Penzias and Robert Wilson [53, 15] using a microwave antenna at Bell Labs found that the microwave sky had an isotropic background radiation. This background radiation was shown with latter measurements to have a well fitted black body spectrum [23]

$$I = \frac{2hf^3}{c^2} \frac{1}{exp(hf/kT) - 1} \tag{1.1}$$

with a temperature of

$$T_0 = 2.7255 \pm 0.0006\,\mathrm{K} \tag{1.2}$$

and mean energy of

$$E_{mean} = 6.3 \times 10^{-4}\,\mathrm{eV}. \tag{1.3}$$

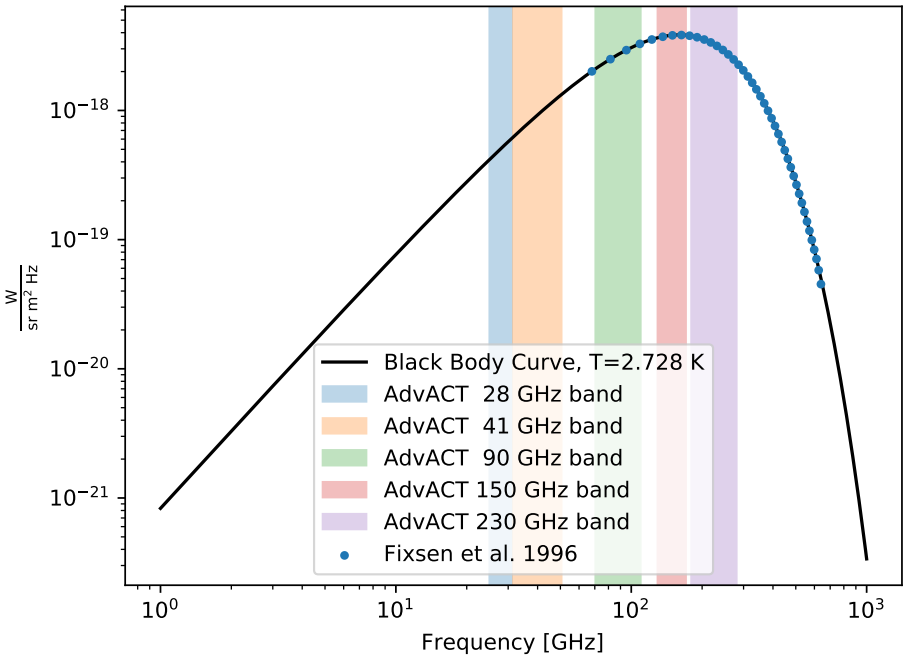

Figure 1.1: Black body curve for the CMB temperature. Points show data extracted from [23].

The peak of the CMB power distribution lies in the far infrared part of the electromagnetic spectrum as shown in Figure 1.1. More specifically, the CMB light peaks at a wavelength of $\lambda = 1.5\,\text{mm}$.

The existence of the CMB is an important piece of evidence for our cosmological model. It means that when the universe was younger, it had a much higher temperature and all matter was ionized making it opaque. At the moment where the universe became transparent from this opaque ionized state it had a temperature of 2970 K. Today's value of the CMB temperature is a factor of 1090 lower. The expansion of the universe allowed it to cool off from this hot and dense initial state.

The expansion history of the universe can be described using Einstein's

equations. In this framework, the scale of the universe at a given time is parametrized with the function $a(t)$ which equals 1 today and was smaller earlier in the universe's history. The scale parameter scales with redshift as

$$a(t) = \frac{1}{1+z}. \tag{1.4}$$

The way we measure distances is given by the metric (ds), which depends on the universe curvature and the scale factor. The metric of an expanding universe can be described following a Robertson-Walker metric

$$ds^2 = -c^2dt^2 + a(t)^2\left[dr^2 + S_k(r)^2 d\Omega^2\right] \tag{1.5}$$

where κ is the curvature parameter and

$$S_k = \begin{cases} Rsin(r/R) & (\kappa = +1) \\ r & (\kappa = 0) \\ R\sinh(r/R) & (\kappa = \text{-}1)\,, \end{cases} \tag{1.6}$$

where R is the radius of curvature. This space-time is homogeneous and isotropic. This metric also satisfies the Hubble law for proper distances, which comes from the radial part of 1.5, which yields

$$\dot{d}_p = \frac{\dot{a}}{a} d_p \tag{1.7}$$

and then the Hubble constant is in our formalism

$$H_0 = \left(\frac{\dot{a}}{a}\right)_{t=t_0} \tag{1.8}$$

which has a current value of 67.7 ± 0.5 km/s/Mpc as reported by Planck [2]. Note that different techniques have reported different values (3σ) for the Hubble constant (see Figure 1.2). The leading methods used to determine it are: the CMB anisotropies, the Distance Ladder in optical astronomy, gravitational wave

detections and time dalays between images of strong gravitational lensing. This discrepancy in the measured Hubble constant is somewhat euphemistically known as the "Hubble constant *tension*".

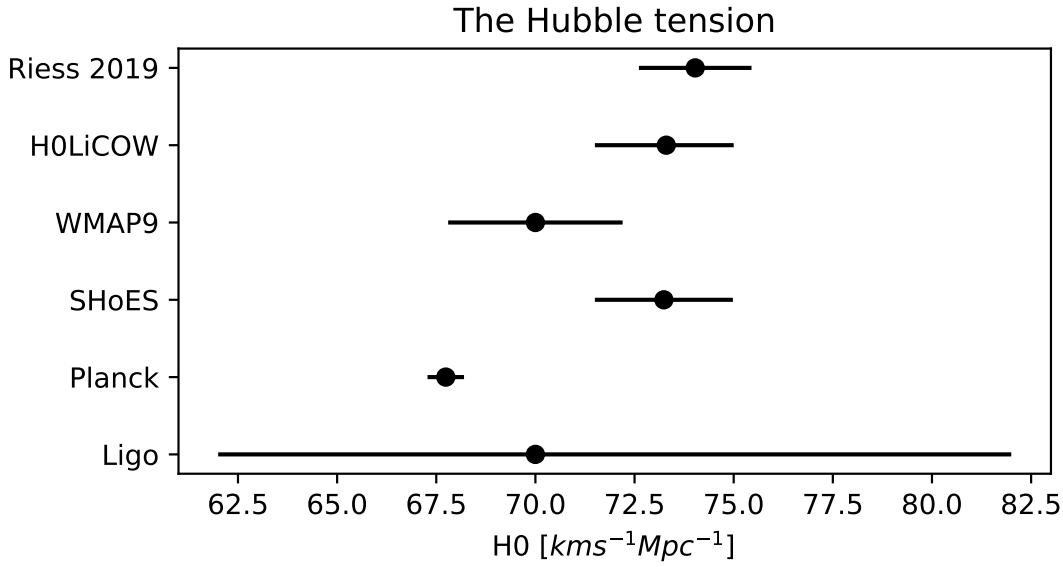

Figure 1.2: The Hubble tension. Values extracted from [43, 62, 54].

1.1.2 The Friedmann Equation

The Friedmann equation links the energy density of the universe with its dynamical state (a and $\dot{a}$). The general relativity form of the Friedmann equation is

$$\left(\frac{\dot{a}}{a}\right)^2 = \frac{8\pi G}{3c^2}\epsilon(t) - \frac{\kappa c^2}{R_0^2}\frac{1}{a(t)^2} \tag{1.9}$$

where ϵ is the energy density. It is common practice to express the energy density with the Ω notation

$$\Omega(t) = \frac{\epsilon(t)}{\epsilon_c(t)} \tag{1.10}$$

where $\epsilon_c(t) = \frac{3c^2}{8\pi G}H_0^2$. And then the Friedmann Equation becomes

$$1 - \Omega(t) = -\frac{\kappa c^2}{R_0^2 a(t)^2 H(t)^2}. \tag{1.11}$$

1.1.3 The fluid equation and the equations of state

In order to solve for a and ϵ two more equations are needed. Using the first law of thermodynamics one can show that the Friedmann equation becomes the acceleration equation

$$\frac{\ddot{a}}{a} = -\frac{4\pi G}{3c^2}(\epsilon + 3P). \tag{1.12}$$

The universe is not made of only one kind of particle, it is instead composed of a combination of particles, each one with a different equation of state. This equation of state is a relation of the form

$$P = P(\epsilon) \tag{1.13}$$

which lets us solve for a, ϵ and P. This equation of state can be complicated and for brevity it is not discussed in detail here, it usually has the form $P = w\epsilon$. For relativistic particles (like photons) $w = 1/3$, while non relativistic particles have a $w \sim 0$. A component of the universe with $w < -1/3$ is referred as dark energy.

1.1.4 Time evolution of the scale factor

If we consider the contribution to the energy density coming from matter with density $\epsilon_m = \epsilon_{m0}a^{-3}$, radiation with density $\epsilon_r = \epsilon_{r0}a^{-4}$ and a cosmological constant $\epsilon_\Lambda = \epsilon_{\Lambda 0}$, the Friedmann equation will take the form

$$\frac{H^2}{H_0^2} = \frac{\Omega_{r0}}{a^4} + \frac{\Omega_{m,0}}{a^3} + \Omega_{\Lambda 0} + \frac{1 - \Omega_0}{a^2} \tag{1.14}$$

which can be integrated to

$$H_0 t = \int_0^a \frac{da}{\sqrt{\Omega_{r,0} a^{-2} + \Omega_{m0} a^{-1} + \Omega_{\Lambda,0} a^2 + (1 - \Omega_0)}}. \tag{1.15}$$

We will revisit this equation in the data analysis of the kSZ effect.

1.1.5 The big picture

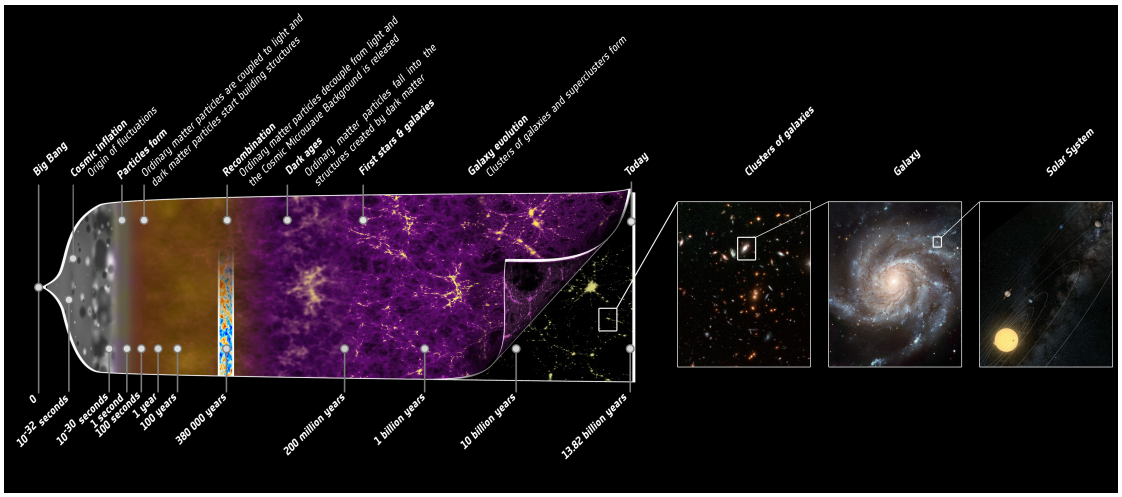

Figure 1.3: Our universe's history. Credit: ESA. [21]

Started about a century ago, scientific cosmology has advanced tremendously. We went from having no theory of how the universe got the state we see today to having one that can be tested by observation. In the following paragraphs, I will briefly summarize what we know today. Figure 1.3 from ESA [21] will serve as a guide.

Early in the history of the universe the energy density was composed of matter, radiation and dark energy. The matter component is made of all known elementary particles plus a dominant fraction made of dark matter (some matter-

like particle with very weak electromagnetic interactions). The radiation component of the energy density was made of photons, neutrinos and relativistic particles. And the cosmological constant term with negative pressure seems to have played no importance in the very early stages, though it is responsible for its acceleration today.

In this early stage of the universe's expansion history, matter and radiation were thermalized. The high energy state of the medium ionized all matter. All lines of sight ended in an interaction with an electron and the medium was opaque.

The universe expanded and wavelengths stretched, cooling off the medium. The temperature decreased following the relation $T(z) = T_0(1 + z)$, where z is the redshift and T_0 is the temperature today.

Small over-densities were carried out throughout expansion and gravitational instability created the structure that we see today: stars, galaxies and clusters of galaxies.

Initially the universe was radiation dominated, with most of the energy density in photons, neutrinos and relativistic kinetic energy. Later on, the universe cooled down enough that the energy density was shared among the radiation component and the matter component of it (matter-radiation equality). Then, as the universe kept cooling down, the energy density budget became dominated by its matter component. Relatively heavier particles had much of the energy density of the universe, i.e.: dark matter and mostly protons and deuterons. When the temperature reached $\sim$ 1eV, atoms formed (this stage is called recombination) and radiation was then too cool to ionize them, it was then when the

universe became transparent and the CMB photons we detect today were released. This happened when the scale factor was roughly 1000 times smaller than today ($z \sim 1000$). After the last scattering that released the CMB, the universe was dark. Matter kept being neutral and the matter dominance slowed down the expansion. The universe was a quiet and dark place until the first stars started igniting. Possibly, supernova explosions started happening injecting energy to the inter-cluster medium, and ionizing the universe, to reach the state in which we observe it today.

Now we are in an era of cosmic acceleration ($z < 2$), with roughly 70% of the energy density causing the acceleration, 25% in the form of dark matter and only 5% in the form of baryonic matter. Explaining what dark matter and dark energy are is one of the greatest challenges physics faces today.

1.2 The Cosmic Microwave Background

Serendipitously discovered in 1965 by Penzias and Wilson [53], the cosmic microwave background (CMB) is today a solid source of our understanding of the history of the universe. The CMB is the oldest light in the universe. It was released when the hot initial plasma expanded and cooled enough to become transparent. In this era, (called of last scattering), the temperature reached roughly 1eV, too cool to ionize a Hydrogen atom; this is when the CMB was released. This happened when separations in the universe were 1000 times smaller than today (redshift of $z \sim 1000$) and the universe was hundreds of thousands of years old.

Multiple results have come from observations of the cosmic microwave

Event	Redshift	Temperature [K]	Time [Myr]
Radiation-matter equality	3440	9390	0.050
Recombination	1380	3760	0.25
Last scattering	1090	2970	0.37

Table 1.1: Events in the early universe. Source: [56].

background:

1. At any point in the sky, the frequency spectrum of the CMB light is well described by a black body. The COBE satellite found that the CMB is described by a black body in up to one part in 10^4.
2. There is a dipole distortion in the temperature distribution. This distortion is the Doppler shift of the CMB light due to the movement of our galaxy in the local group.
3. The temperature fluctuations of the CMB are small in amplitude up to one part in 10^5 (after correcting for the dipole distortion).

The mean temperature of the CMB as observed today is

$$< T >= \frac{1}{4\pi} \int T(\theta, \phi) \sin(\theta) d\theta d\phi = 2.7255K, \tag{1.16}$$

and the root mean square temperature deviation as measured by COBE is

$$\sqrt{\frac{1}{4\pi} \int \left(\frac{T(\theta, \phi) - < T >}{< T >} \right)^2 \sin\theta d\theta d\phi} = 1.1 \times 10^{-5}. \tag{1.17}$$

It is common to describe the statistics of the CMB via its spherical harmonic expansion

$$\frac{\delta T}{T}(\theta, \phi) = \sum_{l=0}^{\infty} \sum_{m=-l}^{l} a_{lm} Y_{lm}(\theta, \phi), \tag{1.18}$$

of which is useful to compute the correlation function

$$C(\theta) = \left\langle \frac{\delta T}{T}(\hat{n}) \frac{\delta T}{T}(\hat{n}') \right\rangle_{\hat{n}\cdot\hat{n}'=\cos(\theta)} \tag{1.19}$$

which has a spherical harmonic expansion

$$C(\theta) = \frac{1}{4\pi} \sum_{l=0}^{\infty} (2l+1) C_l P_l(\cos\theta) \tag{1.20}$$

with P_l the usual Legendre polynomials. CMB experiments usually report the function

$$\Delta_T = \left(\frac{l(l+1)}{2\pi} C_l \right)^{1/2} \langle T \rangle \,. \tag{1.21}$$

Figure 1.4 shows this function as reported by a variety of CMB experiments.

1.3 CMB polarization and inflation

In this section I briefly review the horizon problem, how it is linked to inflation, the tensor to scalar ratio and CMB polarization.

1.3.1 The horizon problem

As discussed in previous sections, the CMB fits quite well a Planck spectrum over three decades in frequency. This suggests that the CMB was in thermal equilibrium at the time of (or before) being released and had a temperature of around 3000 K.

The CMB is measured to be homogeneous over the whole sky by one part in 10^4, this means that the universe was quite homogeneous at the time of the last scattering. One intriguing aspect of this high degree of homogeneity arises

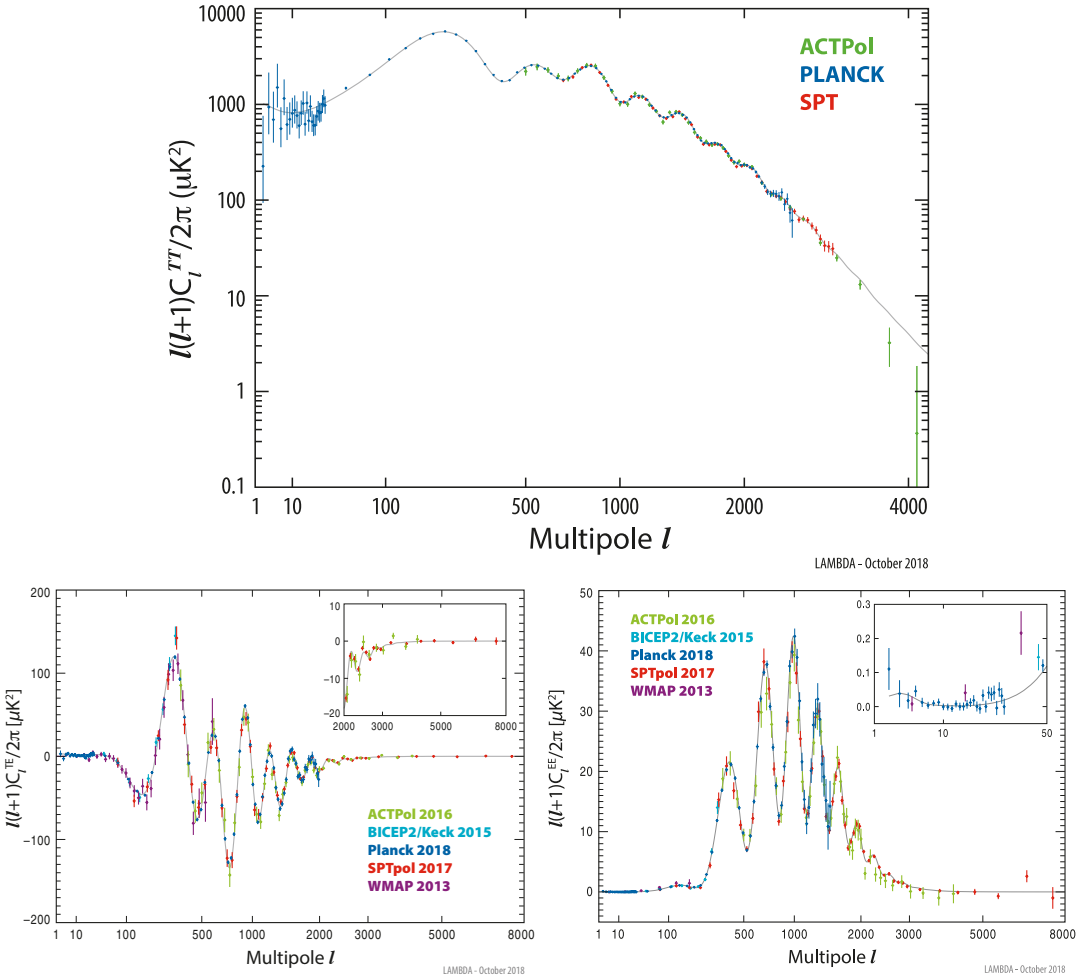

Figure 1.4: CMB power spectra as reported by Planck, ACTPol, SPT, WMAP and BICEP2. Top plot shows temperature (TT) power spectrum, lower left shows TE and lower right EE. Source: LAMBDA. [49]

when considering the size of the causally connected volumes of the universe when the CMB was released. It can be shown that at the time of decoupling, the size of a causally connected sphere subtends an angle of $\sim$ 1 degree in the sky today, which is roughly where the first peak of the CMB power spectrum lies. The homogeneity of the CMB indicates that the CMB sky seems to be correlated even when there was no causal path to communicate between two different parts of the universe back then. The uniformity of the CMB over angular scales

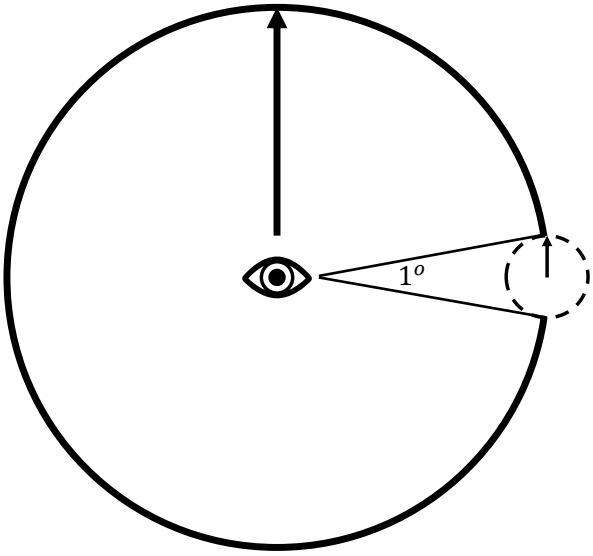

Figure 1.5: The horizon problem. The CMB is seen to correlate to angular scales larger than the coherence scale at the time it was released. In the illustration 1^o is roughly this coherence length. The isotropy however exists to 1 part in 10^4 over the entire sky.

far above 1^o is known as the horizon problem.

It is a quite remarkable fact that the CMB has inhomogeneities at the level of 10^{-5} and that these fluctuations have coherence beyond the horizon at the last scattering. The inflationary model solves this problem by introducing a period of rapid expansion very early in the history of the universe. Inflation would then at $t = 10^{-32}$ s stretch space in the early universe by 20 orders of magnitude. The observable universe today would then have had the size of a Planck length, it would have been in causal contact and in thermal equilibrium. This rapid expansion very early in its history would freeze out this homogeneity.

This paradigm fits the observations. However we are far from understanding the micro-physics that drove inflation. New and more precise measure-

ments promise a closer look into the details of inflationary physics.

1.3.2 The tensor to scalar ratio

All inflationary models predict the existence of tensor fluctuations. The strength of these fluctuations is related to the energy scale of inflation. Inflation however does not predict the level of the tensor modes. The parameter

$$r = \frac{T}{S} \tag{1.22}$$

is known as the tensor to scalar ratio of fluctuations and it depends on the energy scale at inflation

$$V = r(0.003M_{pl})^4. \tag{1.23}$$

A value of $r = 0.001$ corresponds to $V = 6.5 \times 10^{15}$ GeV [57].

1.3.3 Polarization, E and B modes

As we saw in section 1.2, the CMB is decomposed in spherical harmonics for analysis. A similar decomposition exists for the polarization components. In this case, the decomposition is more involved, as polarization is not a scalar field. The bases for polarization are called B and E due to their resemblance to a divergence free (magnetic) and a curl free (electric) fields.

E-modes arise from the density perturbations, which don't produce B-modes. The mechanism that creates polarization from a density perturbation is Thomson scattering via a local quadrupole. Polarization arises from scatter-

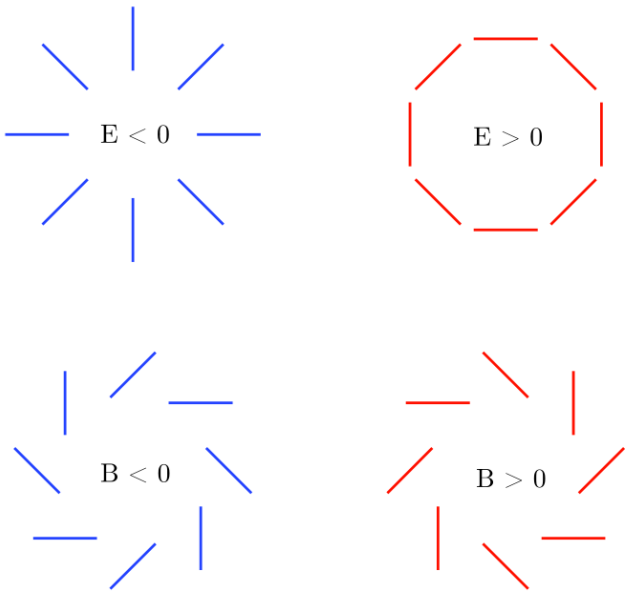

Figure 1.6: E modes have no curl, while B modes have no divergence. Patterns like these over the whole sphere are generated by the tensorial spherical harmonic decomposition of polarization.

ing, so the EE power spectrum peaks when the velocity is maximal, i.e.: there is a peak in EE between peaks of the TT spectrum.

Primordial gravitational waves generate B-modes via Thompson scattering, they peak at $l = 200$ at degree angular scales. Large scale structure will also modify the CMB as it passes through it via gravitational lensing. Gravitational lensing adds to the B-mode spectrum and peaks around 12 arcmin, l=900. This effect has been reported by the Polarbear collaboration, SPT and ACTPol [1, 41, 44], see figure 1.7.

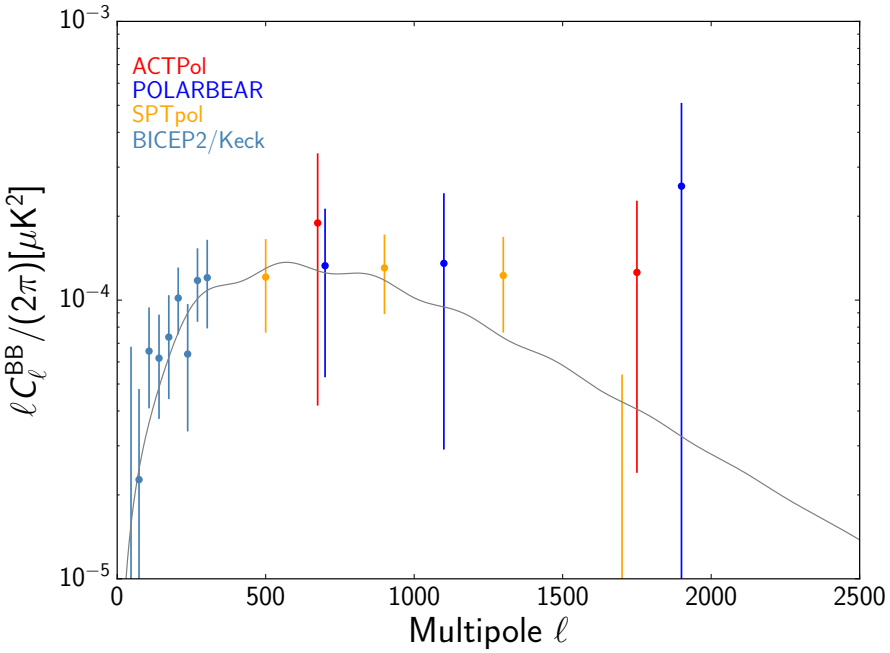

Figure 1.7: BB power spectra reported by ACTPol [44], Polarbear [1], SPT-Pol [41] and BICEP [8]. Figure taken from [44].

CHAPTER 2

OBSERVING THE CMB FROM THE GROUND

In the last decades, ground observatories (in particular in the millimeter) have proven to be a fruitful probe for cosmology. In this chapter I describe how such an experiment works mostly by citing ACT as a case study [60, 13, 34, 59].

CMB experiments share certain characteristics. Broadly the main components of a CMB experiment are an optical system and a receiver. The optics is composed of traditional optical elements (mirrors and lenses) that image the sky onto a focal plane. The receiver transduces the incoming microwave light into voltages and currents that can be detected, digitally sampled and stored.

2.1 Optics

The angular resolution of an optical system composed of a single aperture is given by the diffraction limit

$$\delta\theta = 1.2\frac{\lambda}{D}, \tag{2.1}$$

where D is the diameter of the entrance pupil of the system and λ is the wavelength. In the case of a telescope with a dish, then D is the diameter of the dish. Equation 2.1 shows that for an arcminute experiment operating at $\lambda \sim 2\,\mathrm{mm}$ a diameter of ~ 6 meters is needed. This large diameter makes impractical the use of lenses as the primary imaging element. A degree resolution experiment (like an experiment targeted to map low l in the power spectrum) operating at $\lambda = 2\,\mathrm{mm}$ needs a diameter of tens of centimeters which allows the use of only lenses to image the sky. In practice a small aperture telescope can be made of

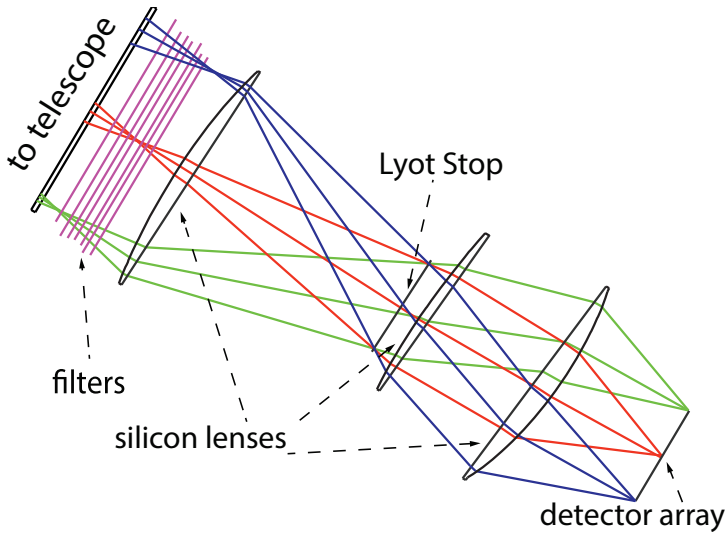

Figure 2.1: The ACTPol camera ray trace. Light from the secondary mirror focuses before the first silicon lens, re-images the primary mirror at the Lyot stop and then is focused on the detector array. Image taken from [13].

lenses *or* mirrors, depending on the design in question.

Large diameter CMB experiments are typically composed of a primary and a secondary mirror (other designs also make use of a third mirror) which usually generate an image at the entrance of a cryogenic camera. In the case of ACT (see figure 2.1), the camera is composed of three cold (4 K) lenses. The lens system is required to image the primary mirror aperture onto a cold stop (Lyot stop) and then focus light onto the focal plane. The use of a Lyot stop helps rejecting warm light from the mirror surroundings. Warm light is detrimental for the experiment performance, since it increases the noise floor at the detectors. Great effort is invested into studying how this light reaches the detector and what can be done to mitigate it. In this work, we studied part of this effect, see chapter 6.

The cryogenic camera has an entrance window through which light enters the instrument. It can also use additional optical elements (which can be present

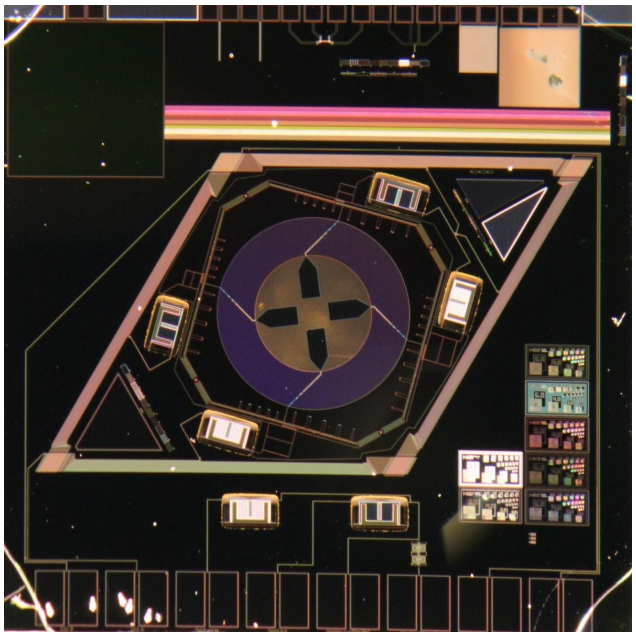

Figure 2.2: Prototype of the Advanced ACTPol high frequency single pixel tested at Cornell. One pixel consists of orthomode transducers (within a circle at the center of the image), TESes and microstrip filters. The TESes can be seen surrounding the central octagon. The lower part of the image shows bond pads, used to connect the sensor to the rest of the test circuit.

or not depending on the specific design) to bring light to the detector focal plane. Some of these elements are: band-pass filters, polarization modulators and feed-horns.

2.2 Sensors

At millimeter wavelengths, transducers can be grouped in two categories: coherent and bolometric. Coherent detectors are used in general astronomy (ALMA, APEX, etc) as they allow high resolution measurements of spectral lines. Heterodyne SIS (superconductor-insulator-superconductor) junctions

dominate the coherent detector market. For wide band detection, bolometric sensors deliver great sensitivity. In particular the use of Transition Edge Sensor (TES) calorimeters has allowed steady progress in the sensitivity of CMB experiments in the last decade.

Transition Edge Sensors

Transition Edge Sensors are made of a thin membrane made of a material that superconducts at low temperatures (hundreds of mK are common today). The devices are biased such that they operate at the onset of superconductivity. In this region the resistance of the device is a fraction of its normal resistance. Voltage bias of the device enables stable operation because of the electro-thermal feedback that arises for small variations in the $\frac{V^2}{R}$ Joule heating. The current in the device is inductively sensed and amplified by cryogenic Superconducting Quantum Interference Devices (Josephson junction flux meters) which are also used as multiplexers. Finally, the current through a TES is multiplexed, digitally sampled, and stored in the time domain, as the telescope scans the sky in azimuth. Figure 2.2 shows one pixel of the Advanced ACTPol array, the reader can find more about the array in [34].

In the case of ACT, a time domain multiplexing scheme is used [36] to read out as many as $\sim 2,000$ detectors per camera. Future CMB experiments will use frequency domain multiplexing schemes that allow reading more detectors ($\sim 10,000 - 100,000$) with less wires per detector [35]. This (plus new optical designs with large fields of view) will enable the fabrication of focal planes with 10 times more detectors.

2.3 Observations

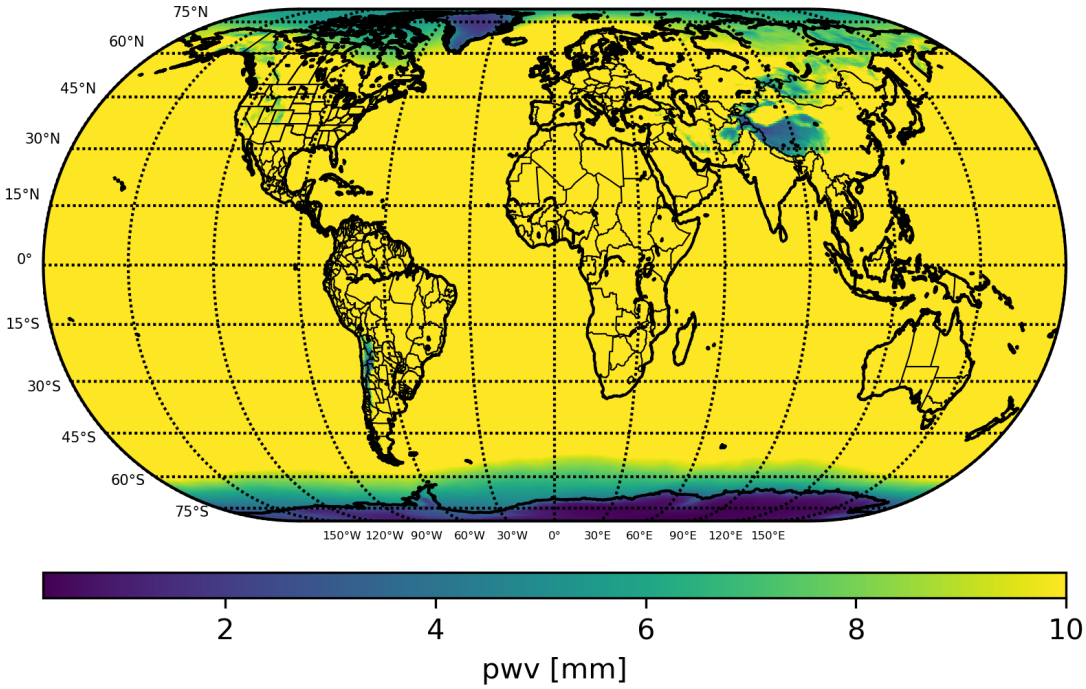

Figure 2.3: World's annual average PWV distribution. Data taken from [29].

A handful of places on earth are well suited for efficient observations on the millimeter and sub-millimeter bands. Good observation sites have good atmospheric transparency, given by a low content of precipitable water vapour in the atmosphere (PWV), as water rotational lines are dominant in the absorption at hundreds of GHz. Figure 2.3 shows the average world-wide distribution of PWV (Figure made with data from the NASA MERRA-2 survey [29]). The Atacama has periods of very low PWV in the Southern hemisphere winter months (July-August) and has periods of bad weather in the summer months (January-February) that tend to skew the average.

The South pole with its low temperatures and elevation (2,800 meters above sea level) is one great site for observations; the South Pole Telescope and Bicep are two experiments currently operating in this polar location. The Atacama desert in northern Chile and part of Argentina is another good location for sub-mm observations. The high Andean peaks of the dry Atacama (with altitudes that easily surpass 5,000 meters in elevation), combined to the logistical benefit of being at driving distance from cities (like Calama) and shipping ports (like Antofagasta) make this place excellent for deployment of astronomical observatories like ALMA and APEX and cosmology experiments like ACT, PolarBear, the future Simons Observatory and CCAT-prime.

2.4 Map Making

After the data is acquired at the high site, it is transmitted via a microwave link down the mountain to the nearest town in San Pedro de Atacama, where it is stored in hard drives. When full, hard drives are extracted and shipped to Santiago, where data is transferred to a supercomputer in North America via the Internet for storage and processing. The map making is the process where the digitally sampled signals from the detectors are taken and an image of the sky is generated. This step is required because the microwave sky has a number of sources of contamination that need to be removed to reach the needed levels of sensitivity. In particular, the most prominent source of contamination is the atmospheric $1/f$ noise. To mitigate the effect of the atmosphere, the scan of the telescope serves as a frequency domain modulation. The scanning takes the signals of interest to a band where the 1/f noise from the atmosphere is sub dominant. Cosmic ray hits also need to be removed from the time-streams and

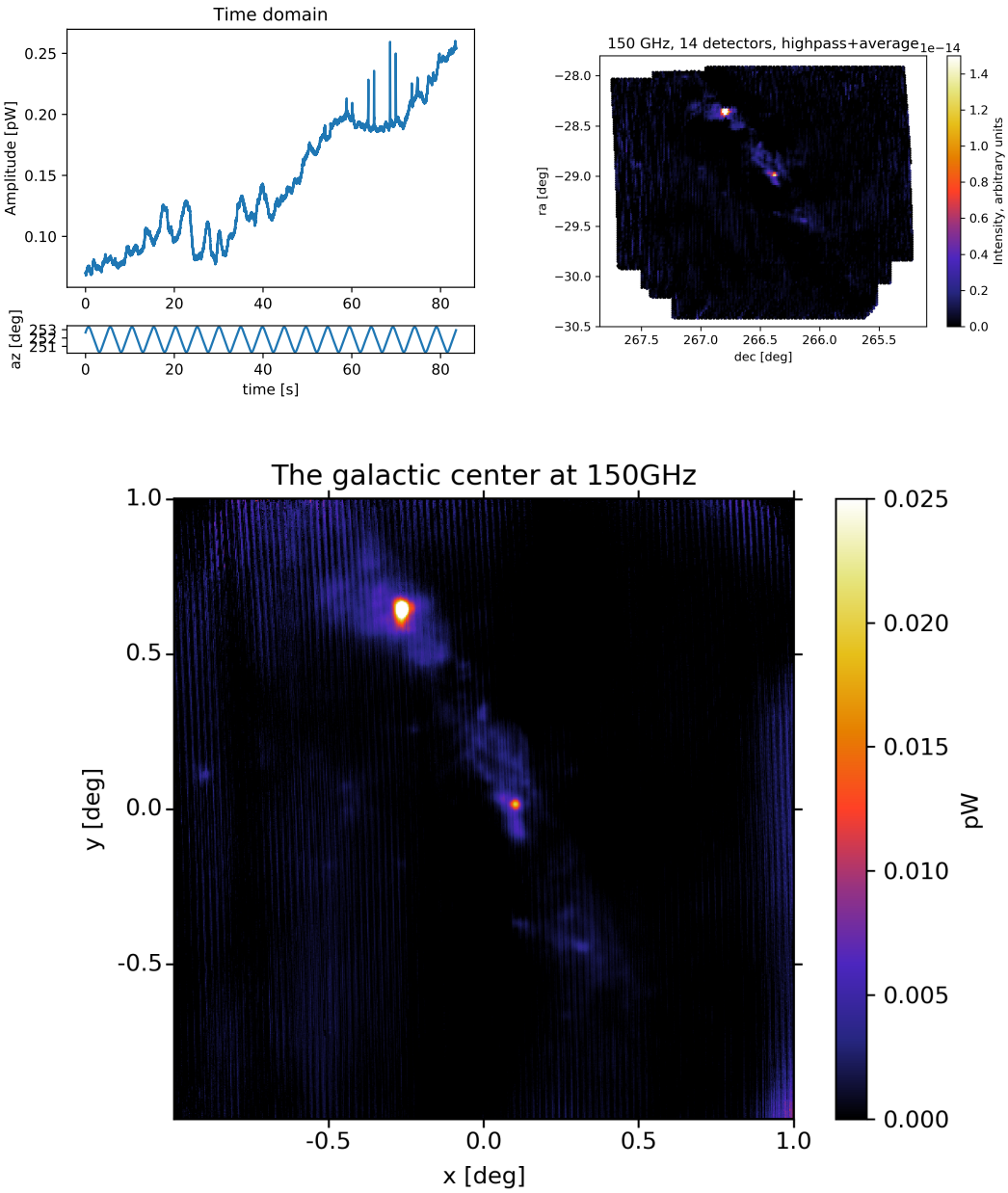

Figure 2.4: Map making example. (Top left) time domain signal as the telescope scans the sky. (Top right) naive map-making done with a high-pass filter and averaging intensities. (Bottom) map of the galactic center done with the ACT PCG planet mapper.

working detectors need to be identified. This is the first pre-processing step done before the map is generated and is referred in the field as 'cuts'.

The map making takes the time domain signal coming from the detectors, uses the position in elevation and azimuth of the telescope at each time on the scan to project each detector on the pixelized sky. In the following lines I describe a toy model for map making; the actual process is more complicated [19, 50].

Let the pixels of the sky we want to map be sorted on a vector m. The entries of m are the pixels of the sky we are interested in mapping. A pointing matrix P converts from pixel to time of observation via the relation

$$d = Pm + n \tag{2.2}$$

where I have added noise to make the problem more realistic. We want to solve for P, but the presence of noise makes things more complicated. The likelihood of a sky m given the data is

$$\mathcal{L} = \frac{\exp -\frac{1}{2}(d - Pm)^T N^{-1}(d - Pm)}{\sqrt{|2\pi N|}} \tag{2.3}$$

where N is the covariance of the noise $cov(d) =< dd^T >=< nn^T >= N$. Which gives a maximum likelihood estimator

$$\frac{d\mathcal{L}(\hat{m})}{d\hat{m}} = 0 \Rightarrow \hat{m} = (P^T N^{-1} P)^{-1} P^T N^{-1} d. \tag{2.4}$$

As the reader can probably realize here, this step is quite involved. A noise model needs to be in place and the size of the matrix $(P^T N^{-1} P)$ is too large to be practicably inverted directly (one map can have more than 10^7 pixels [19]). Usually the map is obtained by iterativelly solving for $\hat{m}$ using a preconditioned conjugate gradient scheme. This part of the process is computationally intensive, and a supercomputer is used in practice. Full detail can be found in [19, 50].

Alternative methods for creating the map exist. For example, one could simply filter and average values that lie inside one pixel. This is simpler and faster but the price to pay is a bias (estimation error) as the model does not take into account the correlations from the noise model. Figure 2.4 shows one example where I used scans of the galactic center done earlier this year. In this example I low-pass filter the time streams and average in the sky pixel space. I compare this to doing the full PCG for one time stream using our planet mapper.

2.5 Sensitivity considerations

The individual components of the instrument (optics, detectors and readout) combine to set the mapping speed of the instrument. The mapping speed is a metric of noise power variance integrated per unit of time. Mapping speed has units of $K^{-2}s^{-1}$, which has the benefit of scaling linearly with the number of detectors. This metric is useful while designing and comparing instruments.

More intuitive from the point of view of first principle calculations is the Noise Equivalent Temperature or NET. The NET has units of $K\sqrt{s}$ and is related to the number of detectors by

$$NET_{arr} = \frac{NET_{det}}{\sqrt{N_{det}}} \tag{2.5}$$

where NET_{arr} is the NET of the array, NET_{det} is the NET of one detector and N_{det} is the number of detectors. The reader should note that this is nothing more than the law of large numbers applied to a radiometer system, i.e. the uncertainty in the average goes down with the square root of the number of averaged samples.

The instrument mapping speed is defined as

$$MS = \frac{1}{NET_{arr}^2}. \tag{2.6}$$

For one individual detector in the array, its NET_{det} is the sum in quadrature of independent components of (uncorrelated) noise. Some of the components of the NET are the photon noise in the detector (NET_{ph}), thermal fluctuations in the detector (NEP_g) and readout noise ($NEP_{readout}$). These sources of noise are better described in the frequency domain (in units of $W/\sqrt{Hz}$) and are translated to the time domain via a factor of 2 that comes from the sampling theorem. The conversion of Watts to Kelvin in CMB units is also needed. With these conversions in mind, we have that the NET for an individual detector is given by

$$NET_{det} = \frac{\sqrt{NEP_{ph}^2 + NEP_g^2 + NEP_{readout}^2}}{dP/dT_{CMB}\sqrt{2}} \tag{2.7}$$

Where dP/dT_{CMB} is the derivative of the Planck law in the bandwidth of interest and has units of W/K_{cmb}. More detail on sensitivity can be found in [37].

For bolometric instruments, when the optical loading of the atmosphere is the dominant part of the noise at the focal plane, the instrument is said to be photon noise limited. This means that in order to increase the sensitivity of the instrument, attention needs to be payed to control the amount of light that enters the receiver if possible.

2.6 ACT

The Atacama Cosmology Telescope, deployed in 2007 is a 6-meter diameter cosmic microwave background experiment that measures the CMB with high an-

gular resolution (1 arcmin) at 150, 220 and 90 GHz. It is located on Cerro Toco in the Chajnantor plateau in Northern Chile. Figure 2.5 shows pictures of the telescope, its location and a ray trace of the optical path before entering the camera.

ACT features three optics tubes with two kilo-pixel arrays of dichroic polarization sensitive transition edge sensor arrays. The first generation camera of ACT, MBAC (a three camera cryostat with 1-kilo-pixel cameras, sensitive to intensity), was replaced by ACTPol (three cameras of 1-kilo-pixel each, sensitive to polarization) in 2013. In 2016 Advanced ACTPol (three 2-kilo-pixel cameras of polarization multichroic arrays) was deployed and has observed to date at 90, 150 and 220 GHz. By the first quarter of 2020 low frequency channels at 30GHz will be deployed.

ACT observes at constant elevation using azimuthal scans to modulate the CMB signals in frequency. The telescope is kept at a fixed elevation and scans are repeated while the earth rotates, hence varying slightly what fraction of the sky each detector sees in each scan.

2.7 The Future: The industrial revolution in cosmology science

The future is exciting. The Simons Observatory is under construction and will be observing the microwave sky in the following years with a set of small aperture telescopes and a large aperture 6-meter class telescope. It will probe the tensor to scalar ratio, the effective number of relativistic species, the sum of the neutrino masses, detect galaxy clusters and enable planetary object searches like planet IX. Also, CCAT-prime will be in operation observing higher frequencies expanding the science impact. The pairwise kinetic Sunyaev-Zeldovich effect

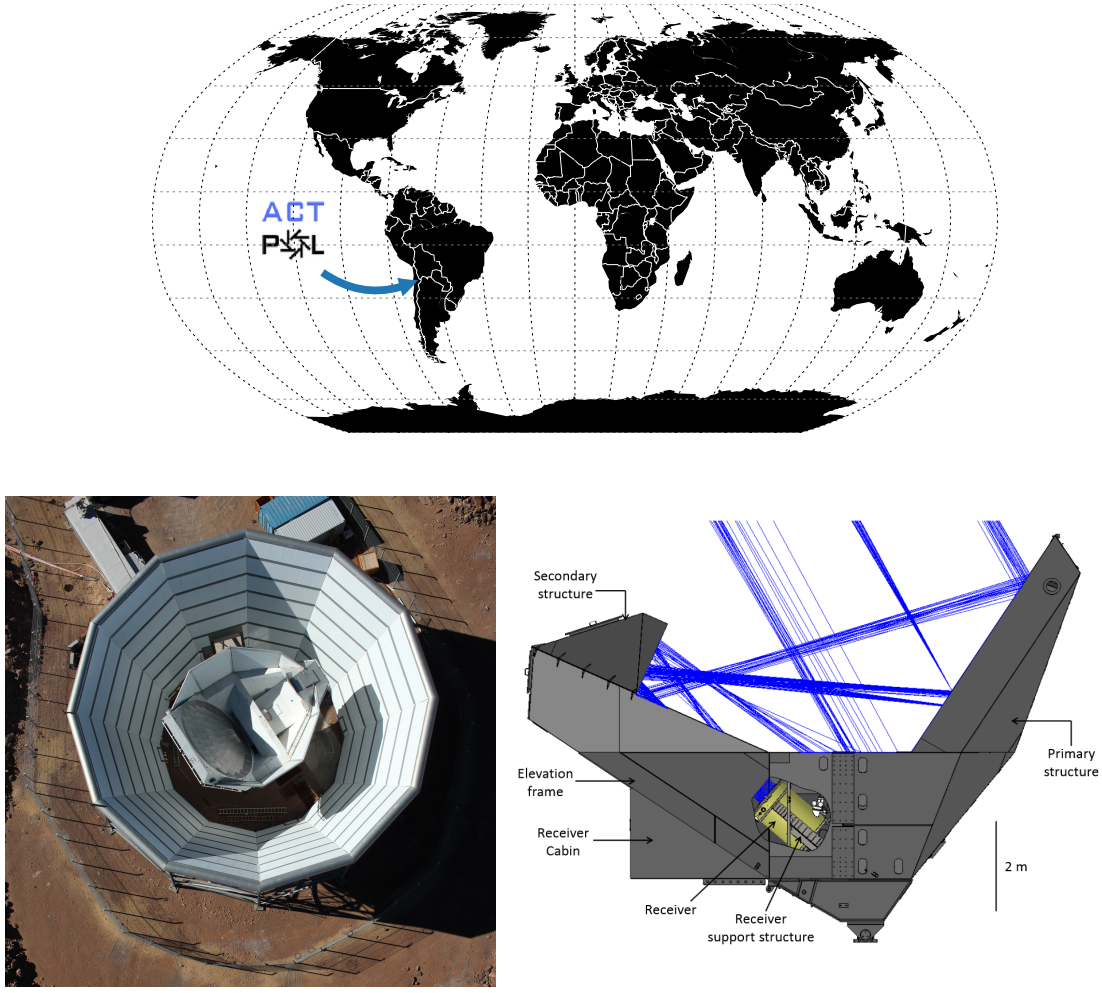

Figure 2.5: (top) ACT location. (lower left) A picture of the telescope; the ground screen surrounds the elevation structure where the primary and a secondary mirrors are attached. (lower right) Ray trace showing the ACT optical path.

analysis that I will present in this thesis will greatly benefit from future surveys. After the Simons Observatory and CCAT-prime an even larger survey can be seen in the horizon: CMB-S4. If fully funded, CMB-S4 will give us much more data to keep cosmologists busy.

We are one step away of seeing a drastic increase in the number of detec-

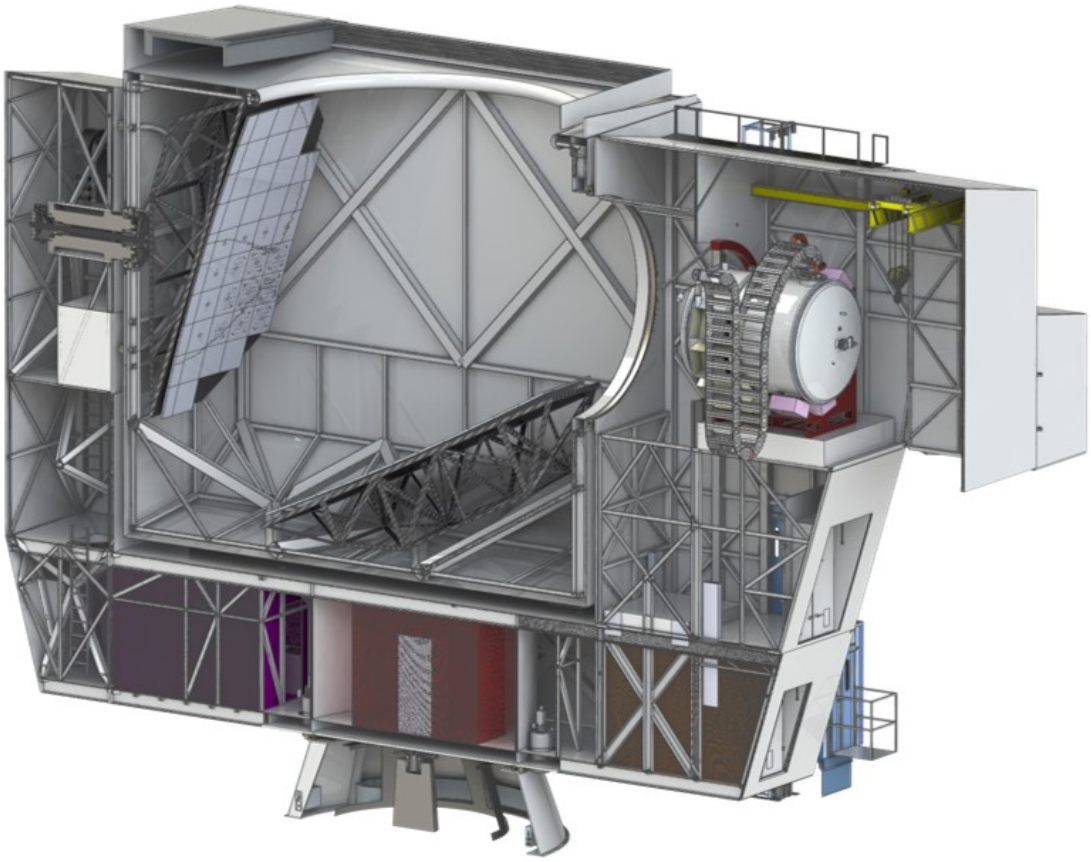

Figure 2.6: The Simons Observatory design concept cross section. Primary and secondary mirrors can be seen on the lower center and left of the image. On the right, the receiver camera. Credit: SO.

tors observing the sky in millimeter waves with arcminute resolution. This increase in sensitivity will expand our ability to test cosmological models, look for extensions of the ΛCDM model of cosmology, probe inflation, measure the movements of clusters of galaxies and much more.

This oncoming set of CMB experiments will also bring new challenges. The amount of data produced will put to the test our ability to handle and efficiently generate our data products. We will be observing the sky so effectively that it will make sense to look for time domain transients in the microwave sky. Big

Figure 2.7: The Simons observatory Site. ACT, Polarbear and CLASS can be seen. In the future, the Simons observatory will deployed on the right of ACT. CCAT prime will be located on top of Cerro Chajnantor, the distant mountain at the center of the image. Picture credit: Debra Kellner.

data tools, like distributed computing and GPU array farms, will be needed and scaled up to deal with all this influx of information. Physicists will become data scientists (which already happened in particle physics). ACT is beginning to look in this direction, incorporating machine learning tools to our pipelines to accelerate the production of maps [30]. Much more is still to be done.

CHAPTER 3

ANTI-REFLECTION COATINGS

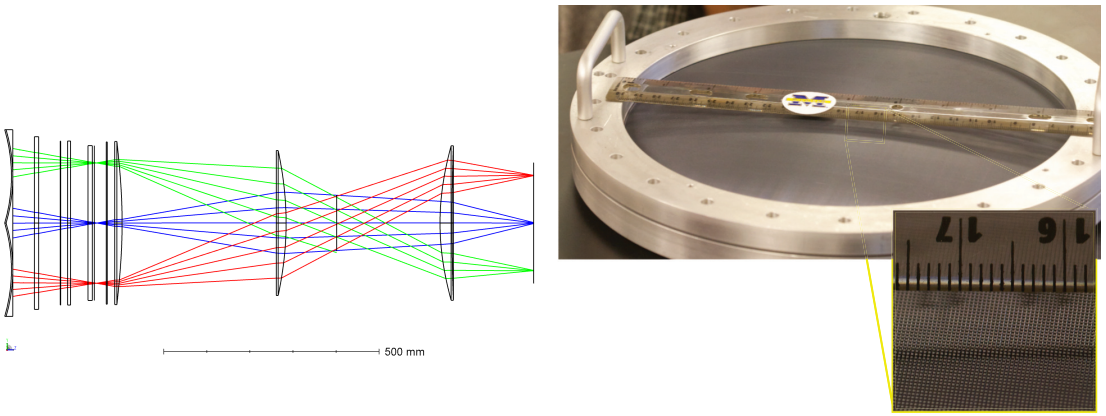

Figure 3.1: (left) Simons observatory large aperture telescope optics tube raytrace featuring refractive silicon lenses. (right) One of the ACTPol silicon lenses. Figure taken from [13].

3.1 Introduction

Large aperture and small aperture cosmology telescopes benefit from the use of refractive optical elements [5, 60, 3]. Refractive optics makes possible re-imaging the entrance aperture allowing a well defined entrance pupil by the use of a Lyot stop. This helps rejecting the warm thermal light from the telescope surroundings. Figure 3.1 (left) shows one receiver design for the Simons Observatory featuring refractive silicon lenses. Silicon is a great material for mm and sub-mm optics due to its large index of refraction (which enables the design of fast optical elements and thus minimizes the size and cost), low thermal expansion coefficient and high transparency. On top of these physical benefits lies the fact that silicon has extensively been studied by the semiconductor industry and processes have been established and optimized over the decades.

This enables commercial availability of high purity silicon which is useful for cosmology experiments.

The high index of refraction of silicon, however, while allowing the design of fast optical elements, presents one difficulty. Refractive reflections, if left unmanaged, limit the amount of light that passes through a silicon sample. This refractive loss can be as high as 30% at each silicon-vacuum interface, thus creating the need for anti-reflection coatings. Anti-reflection coatings use these refractive reflections to control the phase of the reflected wave in one interface to maximize the transmission. The challenge of anti-reflection coatings then consists of finding the right material with the right index of refraction that optimizes the transmission and also can be applied reliably with a high yield and low loss on a large diameter (30cm) silicon lens.

ACTPol demonstrated the use of a meta-material silicon anti-reflection coating, which consists of sub-wavelength cuts made to the silicon lens with a dicing saw. Figure 3.1 (right) shows one of the ACTPol lenses. These cuts lower the density of silicon and make the electromagnetic analog to a material with a lower density. This lower density effectively lowers the dielectric constant. This effective dielectric constant can be tuned by careful design of the meta-material features (texture). The use of this fabrication technique presents limitations on the highest frequency that can be achieved. If the wavelength is too short, a blade that is too thin (to be mechanically stable) is required to make the cuts into silicon.

Our group at Cornell has explored and demonstrated the use of one nanofabrication technique (Deep Reactive Ion Etching, DRIE [63]) to create a meta-material anti-reflection coating that operates at sub-mm wavelenths. We also

used silicon direct bonding [31] to bond two anti-reflection coated samples to demonstrate that such a sample can be fabricated in parts and a flat useful optical element can be created. Our group is currently pursuing (work led by Nick Cothard) the use of such a flat anti-reflection coated sample to make the reflective cavity in the Fabry-Perot spectrometer for the CCAT-prime telescope.

In this chapter I discuss the refractive model we used to compute most of our treatment of the anti-reflection layer. This model, though approximate is useful as it is orders of magnitude faster than electromagnetic simulation techniques and can be used to predict approximately what the transmission of a stack of an arbitrary number of layers will be. It can be used as well to simulate the fringe pattern of a Fabry-Perot interferometer. The mathematical treatment can be found in full detail in [64, 33]. I have written one implementation of such model in the form of a Python 3 library that the reader can find in https://github.com/patogallardo/chal. I will also give a brief summary of the fabrication techniques we used to build the meta-material. Most of the material presented here regarding fabrication and other details can be found in our Applied Optics paper [28].

3.2 Physical models of refractive reflections

Depending on the level of detail needed to model refractive reflections it is convenient to write up a frequency dependent or a frequency independent model. Note that both models describe the same phenomenon on different ranges of applicability. In particular the frequency independent model gives a good description in the limit where the bandwidth is so large (i.e. the ratio $\frac{\Delta\nu}{\nu} >> 1$) that

the oscillations coming from the stratified medium average out. It is common to use the frequency independent model to describe anti-reflection coatings when coherent reflections become important.

3.2.1 Frequency independent model

For a thick slab of substrate (compared to a wavelength) like the one shown in Figure 3.2, we can use the following model to describe the transmission and reflection coefficients. We do this by writing down Maxwell's equations (and boundary conditions) and identifying the two cases ($\vec{E}$ perpendicular to and in the plane of incidence). For the sake of brevity, we will consider the first case ($\vec{E}$ perpendicular to the plane of incidence), an analogous case can be written without much difficulty and can be found in most textbooks, we will present the result in both cases. Here I present the discussion from [33].

For an electric field perpendicular to the plane of incidence, the magnetic field $\vec{B}$ is parallel to it. Continuity in the electric field vector implies that

$$\vec{E}_i + \vec{E}_r = \vec{E}_t \tag{3.1}$$

where the subscripts i, r, t mean 'incident', 'reflected' and 'transmitted'.

We need a second boundary condition to solve for the components of the transmitted and reflected wave. We use the continuity in the tangential component of $\mu^{-1}\vec{B}$ to get

$$-\frac{B_i}{\mu_i}\cos\theta_i + \frac{B_r}{\mu_i}\cos\theta_r = -\frac{B_t}{\mu_t}\cos\theta_t, \tag{3.2}$$

where the left and right hand sides are the magnitudes of $\vec{B}/\mu$ parallel to the interface.

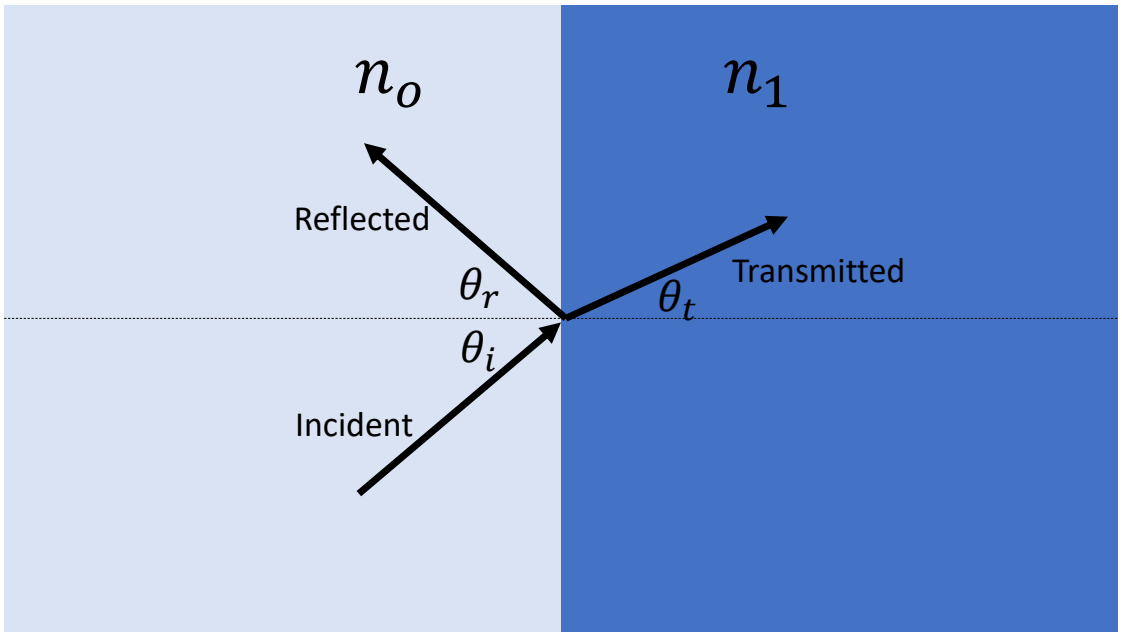

Figure 3.2: Frequency independent model used to describe Fresnel reflections. Light passes from a medium with index of refraction n_o to a medium with index of refraction n_1. The angles that the direction of propagation form with the normal are θ_i, θ_r, θ_t for the incident, reflected and transmitted waves.

Using $B_k = E_k/c_k$ for waves in the k-th medium and $\theta_i = \theta_r$, we get

$$\frac{n_i}{\mu_i}(E_r - E_i)\cos\theta_i = \frac{n_t}{\mu_t}E_t\cos\theta_t \tag{3.3}$$

which combined with equation 3.1 gives

$$r_\perp = \frac{n_i\cos\theta_i - n_t\cos\theta_t}{n_i\cos\theta_i + n_t\cos\theta_t} \tag{3.4}$$

and

$$t_\perp = \frac{2n_i\cos\theta_i}{n_i\cos\theta_i + n_t\cos\theta_t}. \tag{3.5}$$

Similarly it can be shown that

$$r_\parallel = \frac{n_t\cos\theta_i - n_i\cos\theta_t}{n_i\cos\theta_t + n_t\cos\theta_i} \tag{3.6}$$

$$t_\parallel = \frac{2n_i\cos\theta_i}{n_i\cos\theta_t + n_t\cos\theta_i}. \tag{3.7}$$

When $\theta_i = 0$ (the case we are particularly interested in as it is the condition that our designs will meet approximately [13]) the reflection and transmission coefficients (R and T) are

$$R = \left(\frac{n_t - n_i}{n_t + n_i}\right)^2 \tag{3.8}$$

$$T = \frac{4n_t n_i}{(n_t + n_i)^2}. \tag{3.9}$$

From here, note that if we have a semi-infinite space of vacuum ($n_i = 1.0$) followed by a semi-infinite space of silicon ($N_t = 3.41$), the reflection will be

$$R = 0.2975 \approx 30\%. \tag{3.10}$$

Note that this reflection of 30% is per interface, lenses present two interfaces per lens, so for a three lens camera, the transmission will be

$$T = (0.7)^2(0.7)^2(0.7^2) = 6\%. \tag{3.11}$$

This is the reason why we build anti-reflection coatings (see figure 3.3).

3.2.2 Frequency dependent model

In the previous section we studied what happens when light passes from one semi-infinite medium to another. Lets now see what happens when a finite layer is added in the middle as seen in figure 3.4. We will then reach a closed expression for an arbitrary number of layers of homogeneous dielectric constant. Here we will see that the transmittance and reflectance depends on the frequency as interference now appears in the problem and distorts the transmitted powers by canceling and amplifying the output. This model is useful for the experimentalist as it provides the physical foundation of many interference phenomena. We will find that if the pitch (the period of a periodic textured material) of the

Figure 3.3: Its high index of refraction and its bandgap at 1 micron make silicon very reflective in the optical. In the far infrared light does not have energy to excite electrons above the band gap, but still a 30% reflection exists per optical interface.

meta-material is small enough, this model describes well the transmission and reflections coming out of the dielectric boundary. This discussion can be found in reference [64].

Let us consider the case of three indices of refraction (n_1, n_2, n_3). Figure 3.4 shows the three regions in light blue, green and blue. A semi-infinite plane covers the space for $x < 0$ with an index n_1, a finite region of thickness d covers the space between $x = 0$ and $x = d$ and a third region covers the semi-infinite region where $x > d$.

The electric field for a planar wave can be written as a sum of a forward traveling wave and a backward traveling wave as

$$E(x) = Re^{-ik_x x} + Le^{ik_x x} = A(x) + B(x) \tag{3.12}$$

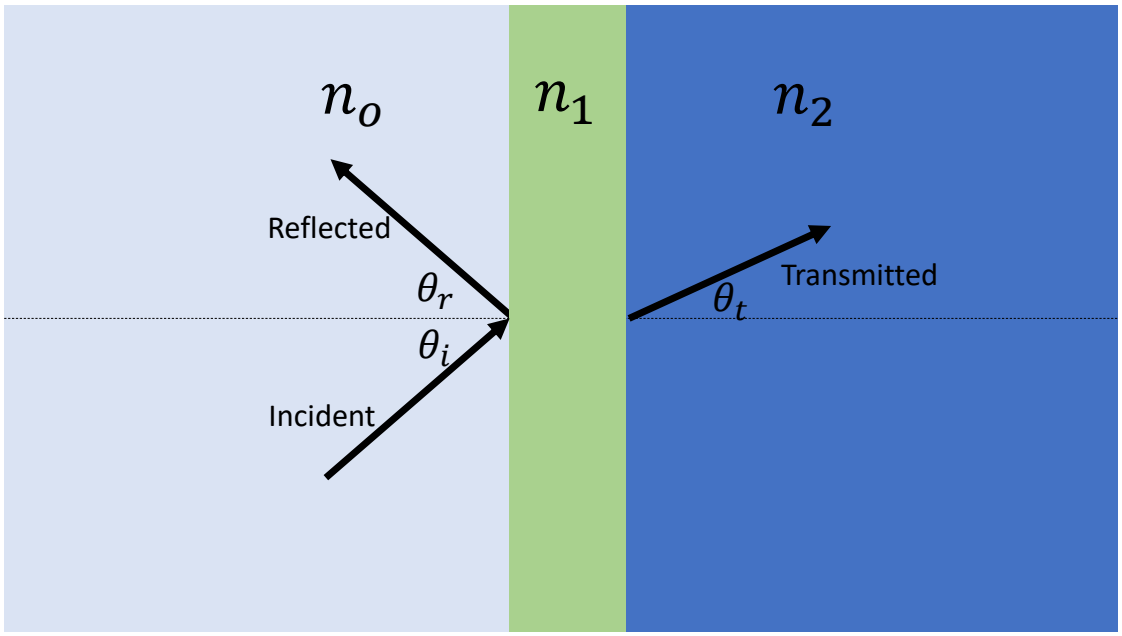

Figure 3.4: Frequency dependent model diagram for a single slab of material.

Introducing the following notation for the values of E at the boundaries:

$$A_j^{\pm} = A(interface_j^{\pm}) \tag{3.13}$$

$$B_j^{\pm} = B(interface_j^{\pm}) \tag{3.14}$$

Where the index j denotes the index of the interface ($j = 1, 2, 3...$) and the sign denotes if we are evaluating the field on the left side or the right side of the interface. Now lets define the matrices

$$D_j = \begin{bmatrix} 1 & 1 \\ n_j cos\theta_j & -n_j cos\theta_j \end{bmatrix} \tag{3.15}$$

for an s wave and

$$D_j = \begin{bmatrix} \cos\theta_j & \cos\theta_j \\ n_j & -n_j \end{bmatrix} \tag{3.16}$$

for a p wave and the matrix

$$P_j = \begin{bmatrix} e^{i\phi_2} & 0 \\ 0 & e^{-i\phi_2} \end{bmatrix}. \tag{3.17}$$

Using these definitions it can be shown [64] that the problem of refractive reflection and transmission on a single layer of material is fully described by the matrix product

$$\begin{bmatrix} A_1^- \\ B_1^- \end{bmatrix} = D_1^{-1} D_2 P_2 D_2^{-1} D_3 \begin{bmatrix} A_3^+ \\ B_3^+ \end{bmatrix}. \tag{3.18}$$

In general, the problem of N layers of dielectric material is given by:

$$\begin{bmatrix} A_0^- \\ B_0^- \end{bmatrix} = M \begin{bmatrix} A_s^+ \\ B_s^+ \end{bmatrix}. \tag{3.19}$$

Where the Matrix M is given by the product

$$M = D_0^{-1} \left[\prod_{l=1}^{n} D_l P_l D_l^{-1} \right] D_s. \tag{3.20}$$

In this formulation, the transmission coefficients of the stack of layers is given by the transfer matrix M according to

$$R = \left| \frac{M_{21}}{M_{11}} \right| \tag{3.21}$$

and

$$T = \frac{n_s \cos\theta_s}{n_o \cos\theta_o} \left| \frac{1}{M_{11}} \right|^2. \tag{3.22}$$

Where R and T are the reflectance and transmittance, which follow conservation of energy and therefore

$$T + R + A = 1 \tag{3.23}$$

where A is the absorption in the material (for the general case where the index of refraction is a complex number).

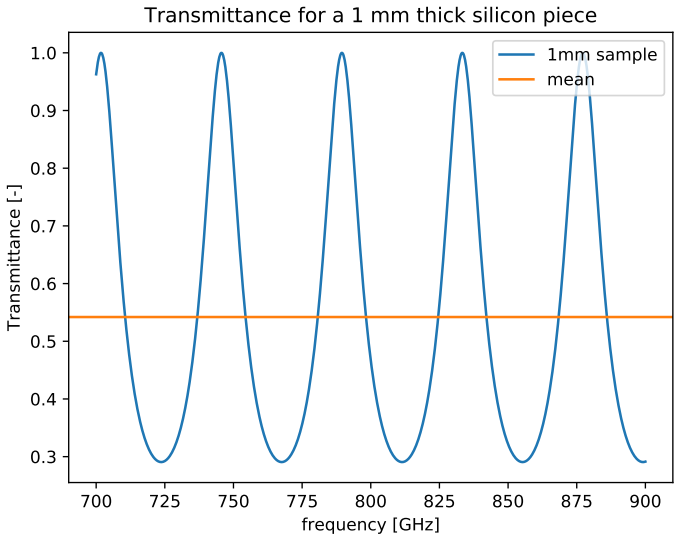

Figure 3.5: Frequency dependent model response for a 1mm thick silicon slab.

Equations 3.21 and 3.22 depend on the cosine and imaginary exponential terms in D_j and P_j, so the R and T is an oscillatory function of the wavelength. Figure 3.5 shows the oscillations in a single slab of 1 mm silicon around 800 GHz. Note that the average is between 0.5 and 0.6. If we had included a large number of oscillations in this average, the mean would converge to our $T = 0.7^2 \approx 0.5$ value. This is the the transmission one would get if using a single silicon lens with no anti-reflection coating.

This formulation is very powerful. In practice, the problem of the transmission and reflection coefficients for one layer of material is analytically simple, but for multiple layers it is quite long to work out in closed form. In practice these equations are computed numerically for the transmittance and reflectance for an arbitrary stack of dielectrics, and can be solved in seconds for a large bandwidth. The plots shown in figure 3.5, 3.6 and the fits in Figure 3.14 were made using the library I have put in GitHub.

3.3 Anti-reflection coatings

It is common in optics to find anti-reflection (AR) coatings made of one or multiple layers. In this section I follow the treatment in Hecht [33] to describe AR layers.

3.3.1 Single layer

Using the matrix formulation presented in the previous section, the reflectance for a single layer of a substrate in contact with a material with index of refraction n_o on one side and n_1 on the other side (and for normal incidence) is given by

$$R_{1layer} = \frac{n_1^2(n_0 - n_s)^2 \cos^2 k_0 h + (n_o n_s - n_1^2)^2 \sin^2 k_o h}{n_1^2(n_0 + n_s)^2 \cos^2 k_o h + (n_o n_s + n_1^2)^2 \sin^2 k_o h}. \tag{3.24}$$

Choosing the thickness of the middle layer to be a quarter of a wavelength or $k_0 h = \frac{1}{2}\pi$ yields the simpler expression

$$R_{1layer} = \left(\frac{n_0 n_s - n_1^2}{n_o n_s + n_1^2}\right)^2. \tag{3.25}$$

Which is zero when

$$n_1 = \sqrt{n_o n_s}. \tag{3.26}$$

This expression sets the index of refraction for a one layer AR coating.

3.3.2 Double Layer

For the double layer AR coating (see Figure 3.7), provided that the two layers are a quarter wavelength, the transfer matrix is diagonal and the reflectance is

$$R_{2layer} = \left[\frac{n_2^2 n_o - n_s n_1^2}{n_2^2 n_o + n_s n_1^2}\right]^2 \tag{3.27}$$

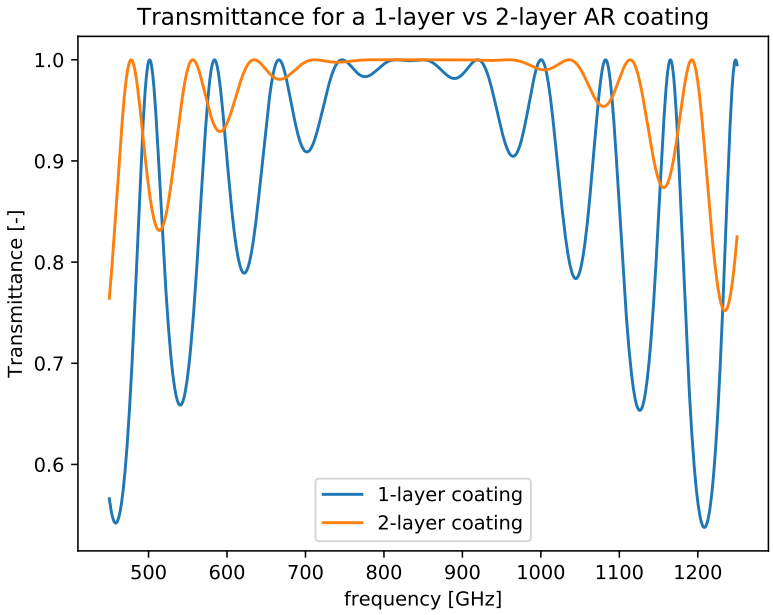

Figure 3.6: 1-layer vs 2-layer coating transmittance around 850 GHz. Note that the double layer anti-reflection coating delivers a much wider bandwidth.

which becomes zero when

$$\left(\frac{n_2}{n_1}\right)^2 = \frac{n_s}{n_o}. \tag{3.28}$$

This kind of multi-layer anti-reflection coatings allow a broader bandwidth than a single layer one. Figure 3.6 shows a comparison of an anti-reflection coating of one layer vs a two layer coating. Notice that the bandwith at which the transmittance is close to unity is larger for the two layer case. This large bandwidth of multi-layer coatings makes them suitable for CMB experiments. In the case of AdvACT a similar coating was implemented by the use of a silicon dicing saw in millimeter wavelengths. Cothard et al. are currently designing and building such two layer coating for submillimeter bands by extending the techniques presented here (DRIE). This kind of coating will be implemented for the CCAT-prime telescope.

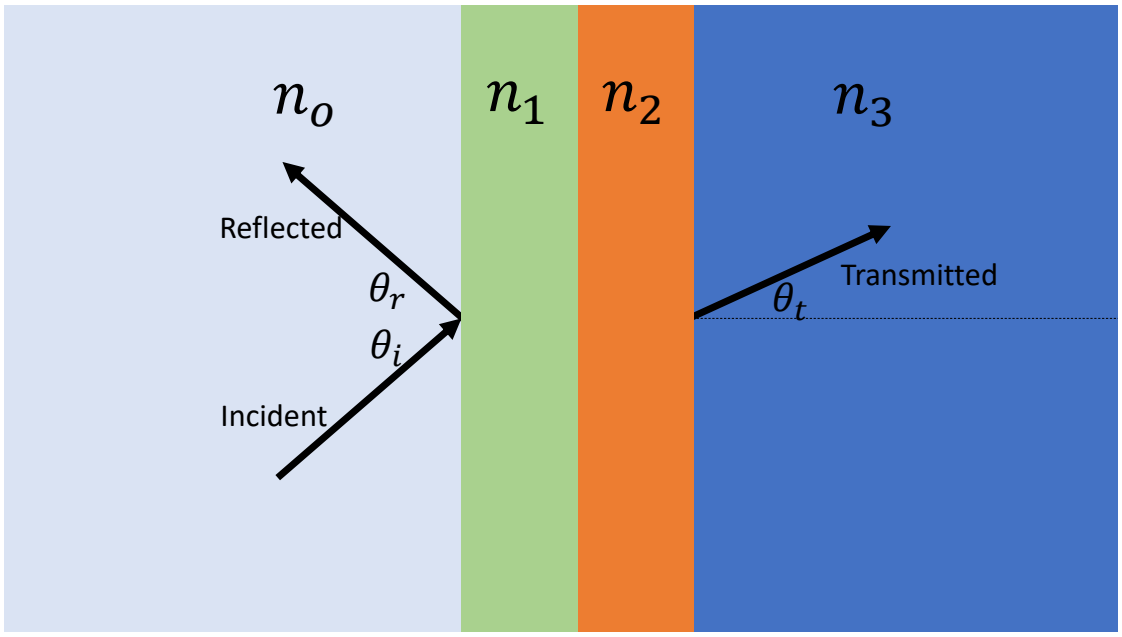

Figure 3.7: Diagram of a double layer anti-reflection coating.

3.4 Meta-material geometry and electromagnetic properties

The geometry of the meta-material governs its effective dielectric constant. In this section the geometry of our meta-material is described and an analytic model used to compute its electromagnetic properties is presented.

3.4.1 Geometry

The contact lithography tools we used allow the application of a regular pattern on a quartz mask. This allows us to define a periodic lattice-like structure on the meta-material. It is known that an x-y symmetric material will present minimum cross-polarization. This is the main reason for choosing a square pattern like the one used on ACTPol.

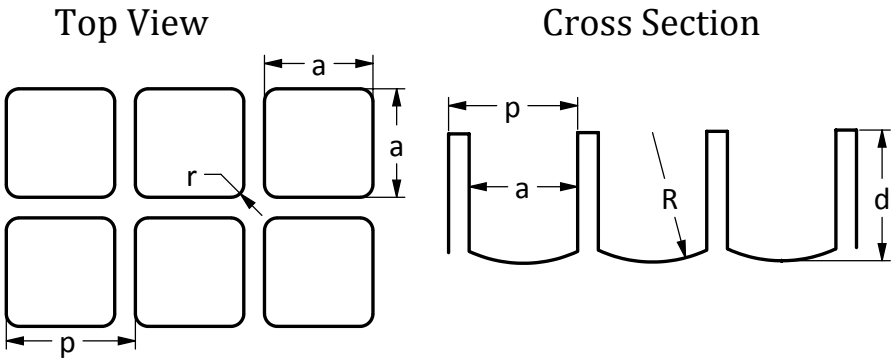

Figure 3.8: Meta-material geometry

A square periodic pattern can have two geometries: pillar-like or hole-like. We chose a hole-like structure (see Figure 3.8) after considering that it would be more mechanically robust than a geometry made out of pillars, as the etching would produce micro-fractures along the axis of the cuts, which could produce a macroscopic failure of the silicon crystal while under stress.

3.4.2 Effective dielectric constant

We used an analytic model to estimate the electromagnetic properties of our square mesh. In our model the square grid is replaced by a network of capacitors. This model is correct on DC (i.e. in the limit where the wavelength is much longer than the feature size). It has the benefit of allowing a fast calculation of the transmittance with the Fresnel equations model that was presented in the previous section.

To extract the effective dielectric constant of the square lattice, we compute the equivalent capacitance of the system and solve for ϵ. It can be shown [7] that

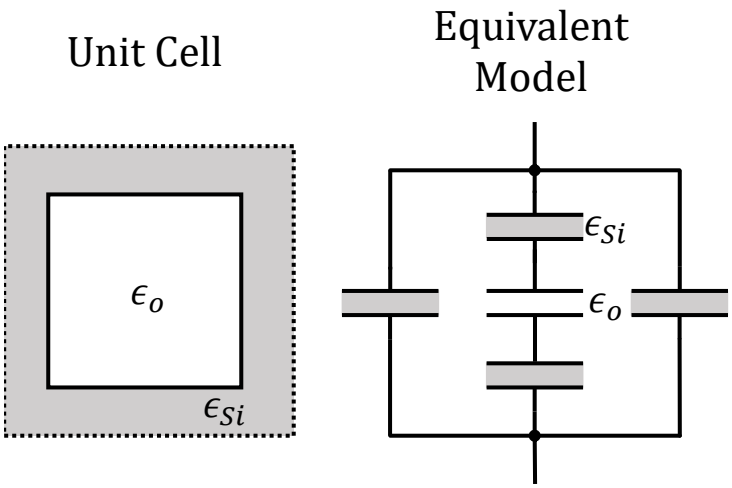

Figure 3.9: Capacitive model.

the equivalent dielectric constant for the system in Figure 3.9 is given by

$$\epsilon_{eff} = \epsilon_{si}(1 - a/p) + \frac{\epsilon_{si}\epsilon_o a/p}{\epsilon_{si}a/p + \epsilon_o(1 - a/p)}. \tag{3.29}$$

This expression reaches the desired optimum $\epsilon_{eff} = \sqrt{e_{si}}$ when $a/p \approx 0.79$. We used this value as a starting point for our simulations and used CST Microwave Studio to compute the S parameters from a given geometry.

3.4.3 Deep Reactive Ion Etching

Progress in silicon technologies has evolved drastically in the past decades, technologies for treating silicon have been developed for the manufacturing of microcircuits in electronics to the use of devices in mechanical actuators and sensors. One technique that is widely used in device manufacturing like MEMS (and is actually also used in the fabrication of large detector count multichroic, polarization sensitive arrays of TESes [18]) is Deep Reactive Ion Etching (DRIE) [63].

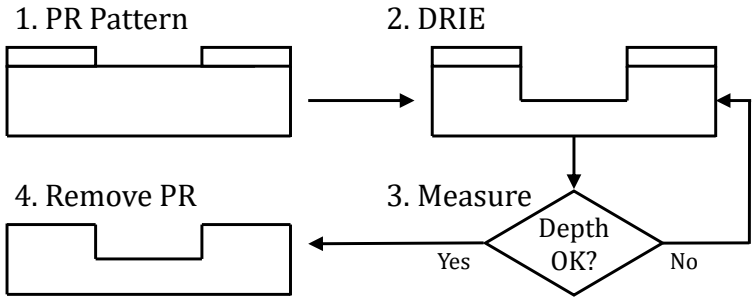

Figure 3.10: Diagram of the etching process. A photo-lithography mask is applied on a silicon wafer. The DRIE process is started. The depth is measured and if the etching is deep enough, the process is stopped. Finally the photo-resist is dissolved by a chemical bath.

DRIE makes use of a set of chemical reactions that remove silicon from the surface plus the ion bombardment from a plasma that enhances the reaction rate anisotropically. A second chemical deposition layer is used after the anisotropic etching to coat the lateral walls of the etched hole, which increases the anisotropy of the overall process.

We used the DRIE process available at the Cornell Nano Fabrication facility (CNF) to manufacture our prototype on a 100 mm wafer. The process of DRIE requires the manufacture of a quartz lithography mask, the application of a photoresist mask which takes the pattern from the quartz mask via a contact aligner and a final step of DRIE.

We applied the DRIE process in three stages where we measured the progress of the etched holes and computed the etch rate to estimate how many DRIE cycles needed to be applied. Each DRIE cycle etches a fraction of a micron. We found that the actual etching rate varies as much as a factor of 2 during one etching cycle. Monitoring of the depth of the holes (see Figure 3.10) compensated for the variance in the etching rate. Figure 3.11 shows one small silicon

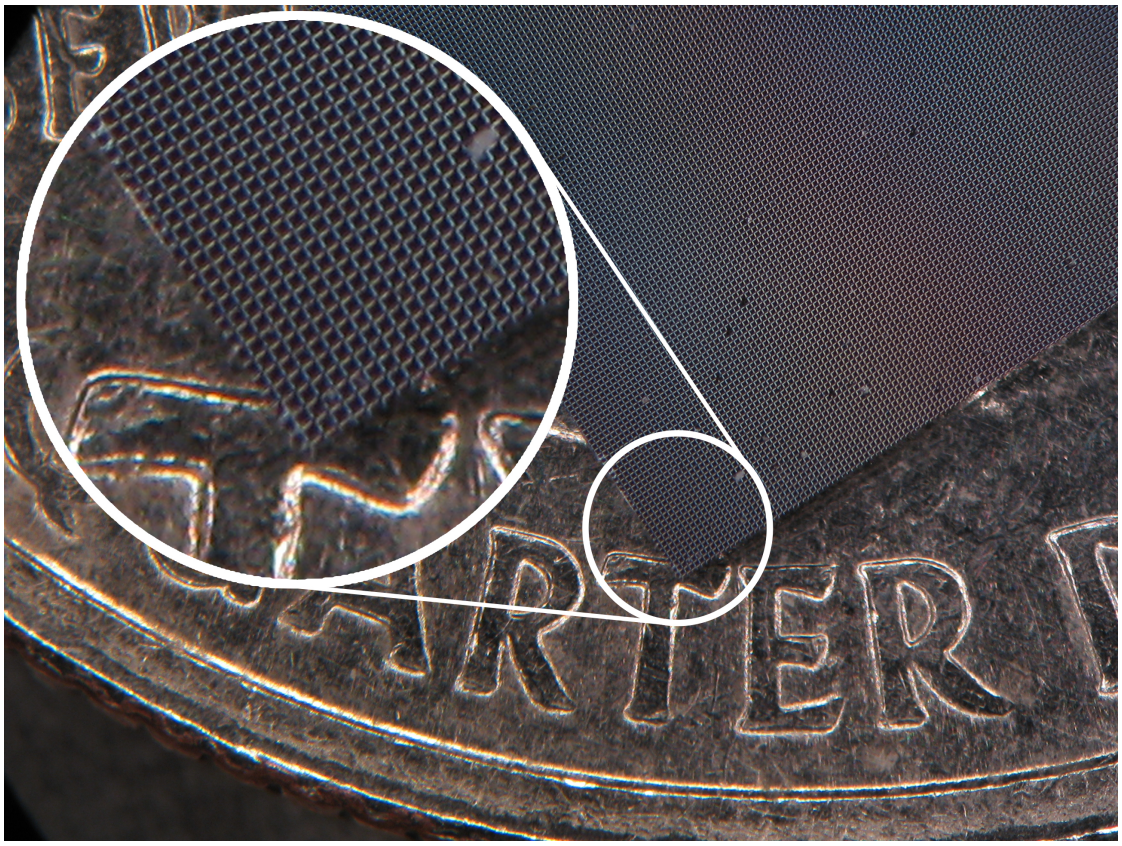

Figure 3.11: Anti-reflection coating on top of a quarter dollar coin.

piece after the process.

3.5 Silicon bonding

In addition to developing the meta-material AR coating, we applied another silicon technique to bond pieces of silicon. The idea here is to enable fabrication in separate stages. In that way an anti-reflection coated sample can be made on one side of the silicon wafer and then bonded to a larger substrate.

We used direct silicon bonding (see [10, 31] for a review) to bond the wafers.

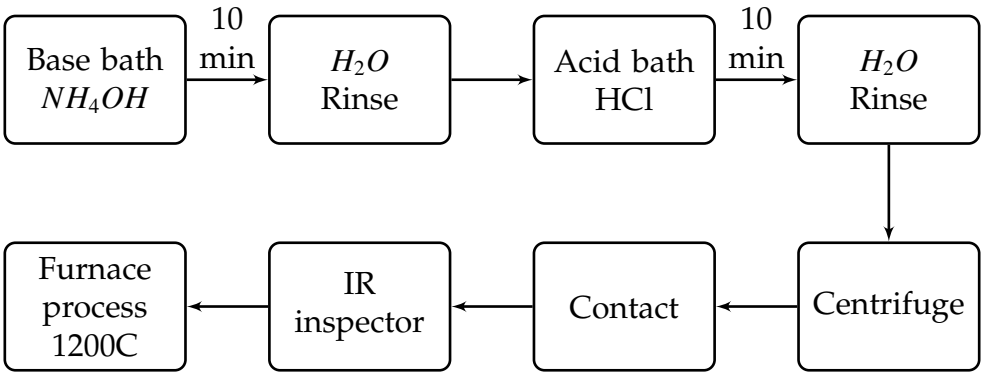

Figure 3.12: Schematic diagram showing steps in the bonding process. The base and acid bath is used to remove the native oxide layer from the silicon. The rinse removes the chemical bath remains and adds some moisture. Under contact a weak bond occurs. Finally a high temperature furnace enables the covalent bond creating the permanent bond.

This technique allows a bond without the use of a chemical glue, as it uses the silicon native chemistry to do the bonding.

Chemically, direct silicon bonding works by creating a covalent bond in the silicon via bonding to a water molecule. This is done by removing the native oxide from the top layer of the silicon by using an acid/base bath and placing the samples in a hot furnace. The process occurs at a temperature of around 1000 C. The high temperature of the process allows the reaction that ultimately creates a covalent bond. Figure 3.12 shows a schematic of the process. This technique has the advantage of not having to use a lossy plastic in the space between samples. However it is susceptible to imperfections as the bond needs both surfaces to be mirror polished and in perfect contact with one another. A single speck of dust of a few microns can create an imperfection of a few centimeters in size. More elaborated schemes have been proposed but we achieved good results by just using the CNF clean room. For production in a massive scale or if the cost of each sample is considerable, we recommend the use of a mini clean room

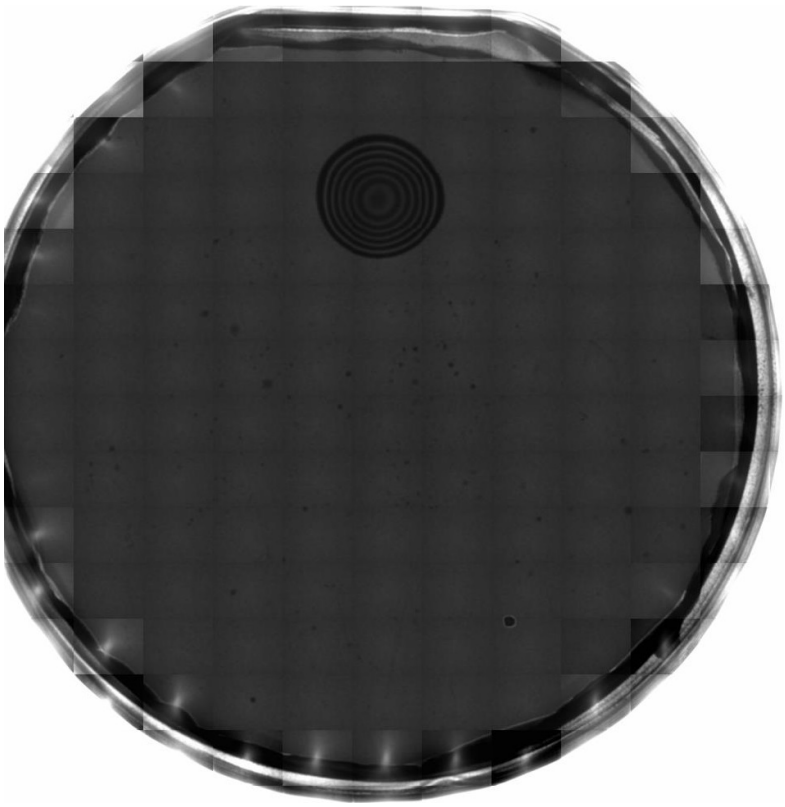

Figure 3.13: Infrared transmission image showing imperfections in the bonding process.

approach as it has been proposed in the literature [58].

3.6 Results

We tested our samples at Nasa Goddard Space Flight Center in Maryland. We used a Bruker Fourier Transform Spectrometer which allows to probe the 0.9 to 21 THz range in the far infrared. We used a liquid helium cooled detector and cooled the silicon samples to 10 K with liquid helium. We tested samples with and without the AR coating in combinations of bonded and unbonded wafers. Figure 3.14 shows the measured transmission curves. We achieved transmis-

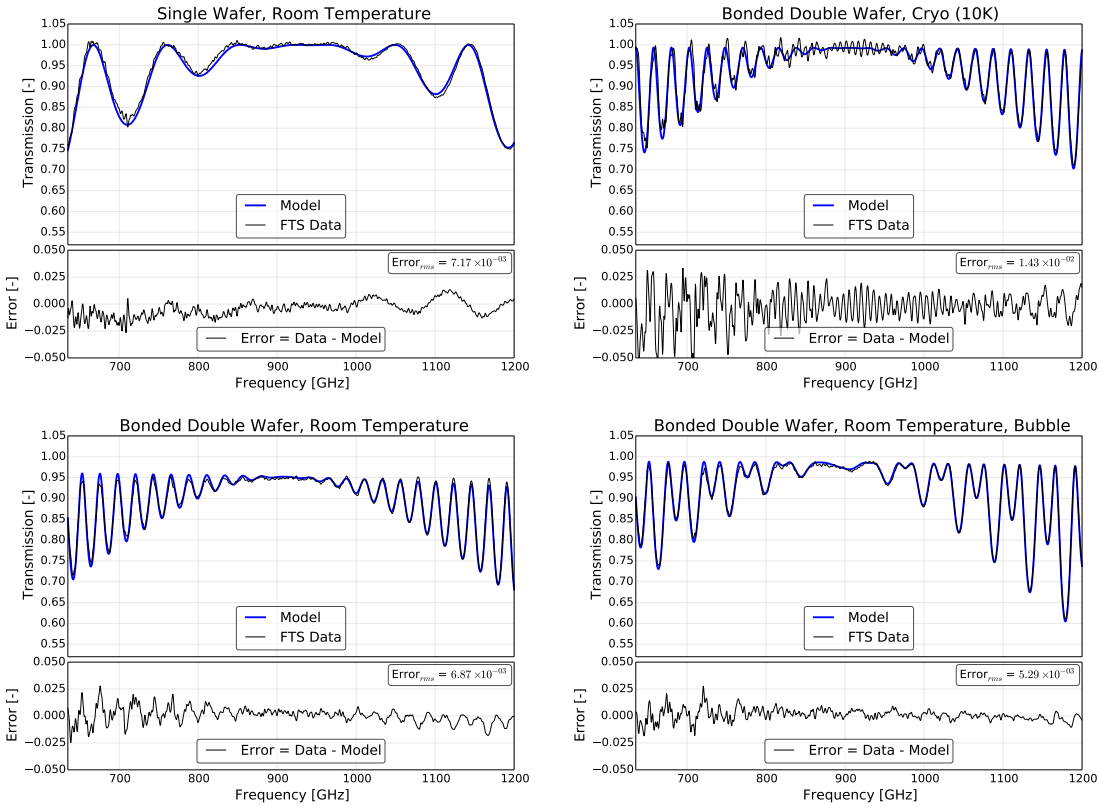

Figure 3.14: Transmission curves measured with the Goddard FTS. Top left: AR coated single wafer at room temperature. Top right: Bonded double wafer at cryogenic temperature (10K). Bottom left: Bonded double wafer at room temperature. Bottom right: Bonded double wafer at room temperature on a region where a bubble is present.

sions better than 99% for a single wafer coated on both sides both at room temperature (Figure 3.14 top left) and at cryogenic temperatures (not shown). The bonded samples showed similar performance (transmission > 99%) at cryogenic temperatures (Figure 3.14 top right) and showed a loss of 5% at room temperature (Figure 3.14 bottom left). The origin of this loss is unclear, though because CMB experiments use cold optics this effect will not appear if a sample like this is fielded in a scientific instrument. We also observed the effect of the gap formed by an imperfection (which can be seen at the upper center of the wafer

in Figure 3.13) in the bonding process which generated the double peaks shown in Figure 3.14 (bottom right).

Work presented in this section is now being extended on the development of metamaterial silicon etalons for Fabry-Perot interferometers that will be used in CCAT-prime [12].

CHAPTER 4

DETECTOR NOISE ALIASING

4.1 Time domain multiplexing and aliasing

Advanced ACTPol uses a time domain multiplexing scheme [35]. In time domain multiplexing the readout signals from each TES are switched in time while being sampled by the ADC in the system. Because of the finite sampling frequency and the physical nature of detector noise in the system, aliasing (out of band noise folding to lower frequencies) needs to be considered. In this chapter the mathematical description of aliasing will be given mostly following the standard treatments on signal analysis textbooks [51]. Measurements in the field with the as-deployed configuration will be described. Finally I will discuss how the aliased noise was estimated from these measurements and how we treated uncertainty.

4.2 The Sampling Theorem

The sampling process can be described as a multiplication of the original continuous time domain signal by a train of Dirac deltas. Our sampled signal will be

$$x_s = x(t)p(t) \tag{4.1}$$

where

$$p(t) = \sum_{-\infty}^{\infty} \delta(t - nT). \tag{4.2}$$

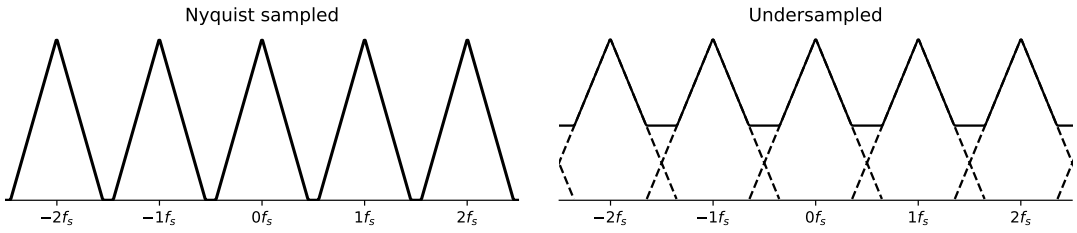

Figure 4.1: (left) Spectrum of a Nyquist-sampled signal. (right) Spectrum of an under-sampled time domain signal. Note that the high frequencies on the positive side of the spectrum mix with the high frequency content on the negative side of the spectrum. Frequency confusion arises.

The time domain sampled signal will be described by the sum

$$x_s(t) = \sum_{n=-\infty}^{\infty} x(nT)\delta(t - nT), \tag{4.3}$$

and the spectral content of the time domain sampled signal will be

$$X(j\omega) = \frac{1}{2\pi}\int_{\infty}^{\infty} X(j\alpha)P(j(\omega - \alpha))d\alpha \tag{4.4}$$

where capital letters evaluated in $j\omega$ denote the usual Fourier transform.

Using the identity for the Fourier transform of a train of delta functions

$$P(j\omega) = \frac{2\pi}{T}\sum_{k=-\infty}^{\infty} \delta(\omega - k\omega_s) \tag{4.5}$$

and the identity of the convolution of delta functions $X(j\omega) * \delta(\omega - \omega_0) = X(j(\omega - \omega_0))$ we finally reach

$$X_s(j\omega) = \frac{1}{T}\sum_{k=-\infty}^{\infty} X(j(\omega - k\omega_s)). \tag{4.6}$$

In other words, the sampling theorem states that a band limited signal with $X(j\omega) = 0$ for $|\omega| > \omega_M$ is uniquely determined by its samples if the sampling frequency

$$\omega_s = 2\pi f_s = \frac{2\pi}{T} > 2\omega_M. \tag{4.7}$$

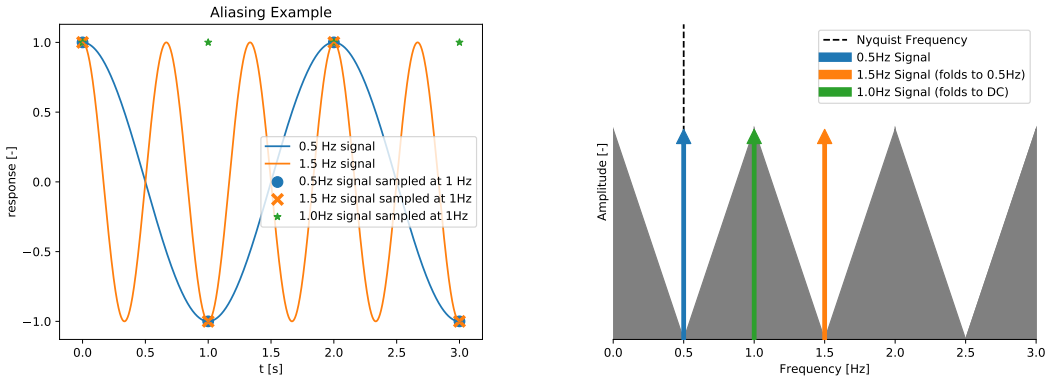

Figure 4.2: (left) Illustration of aliased frequencies. In this example two cosine waves of frequencies (0.5Hz and 1.5Hz) are sampled at $f_s = 1Hz$. Notice that the samples are identical despite the signals having different frequencies. The 0.5Hz signal is the highest frequency that can be Nyquist sampled, while the 1.5Hz signal is the first frequency that is aliased to 0.5Hz. A third continuous time signal at 1 Hz sampled at 1Hz folds back to DC. (right) Frequency domain diagram of the behaviour at the left. The triangles represent the way the sampled signal folds on the frequency domain. Arrows show the spectral position of the signals shown on the left figure. Notice that the signal at 1Hz folds to DC while the signal at 1.5Hz folds to 0.5Hz.

Note that the sampling theorem requires the continuous time domain signal to be band limited in order for a one to one reconstruction to be possible. If the continuous time signal is not band limited, the phenomenon called aliasing arises and the signal cannot be uniquely reconstructed form its time domain samples (see Figures 4.1 and 4.2). It is common practice to add a low pass filter either as an analog filter or a digital one to mitigate this. In this case such a filter is called an anti-alias filter and its objective is to limit the noise power at frequencies larger than the Nyquist frequency.

4.3 What is aliasing

In the previous section we explored the conditions that need to be met for a continuous time signal to be reconstructed from its samples. We concluded via the Sampling Theorem that the condition we need to impose is that the signal is band limited and that the highest frequency in the original signal to be half of the sampling frequency. The spectrum of the sampled signal consists of infinite replications of the spectrum of x(t). If the maximum frequency in the original signal is larger than the Nyquist frequency, then the original signal is no longer recoverable via low pass filtering. This phenomenon, when the replications of the original signal overlap, is known as aliasing.

In practice, when a frequency in the spectrum of the original signal that is being sampled is larger than the Nyquist frequency, its power will be added to the power of another in band frequency (lower than f_{Ny}) and therefore it will be assigned the wrong frequency (aliased). Exactly what frequency will be assigned to one particular frequency depends on which side of the infinite repetitions of the original spectrum the frequency in question fall on.

For example, if the frequency f in question is between f_{Ny} and f_s the power in this line will be assigned to the frequency $f_{Ny} - |f - f_{Ny}|$. If the frequency f is between $2f_{Ny}$ and $3f_{Ny}$, its power will be assigned to the frequency $f - 2f_{Ny}$. This phenomenon is informally known as frequency folding, as its behaviour is what happens when one draws the original spectrum and folds the piece of paper where the graph is drawn on at $n \times f_{Ny}$ with n an integer.

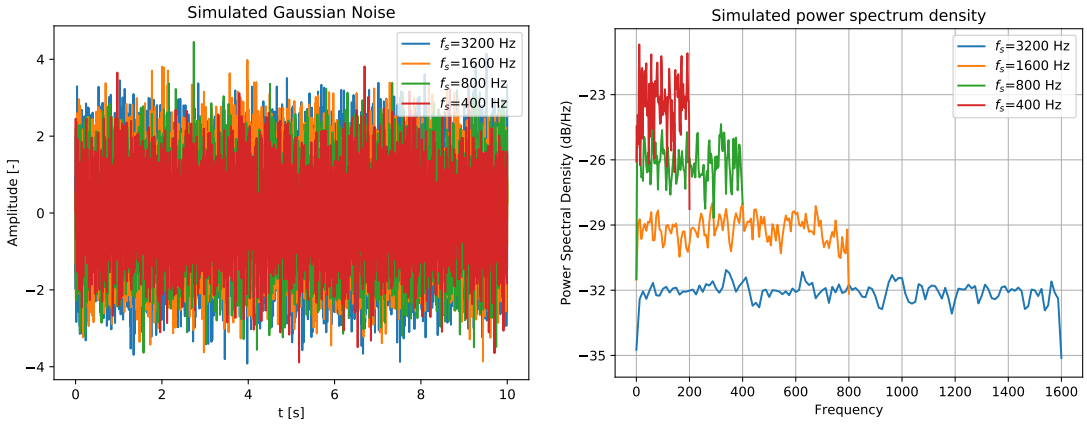

Figure 4.3: (left) Time domain gaussian noise in aliasing simulation. (right) Power spectral density of aliasing simulation.

4.4 An example of aliased white noise

One way of simulating the effect of aliased noise in a detector system is by drawing numbers for a random number generator and exploring how noise varies in the sampled time streams as we vary the sampling frequency.

Lets generate random numbers from a Normal distribution with zero mean and variance $\sigma = 1$. Using this distribution we generate timestreams with the same length in time (that for this example I will keep at 10 seconds) and for various sampling frequencies $f_s \in \{400, 800, 1600, 3200\}$.

In Figure 4.3 (left) the generated gaussian noise is shown. Note here that the lowest sampling frequecy seems to have a lower standard deviation, this is an artifact of the visualizaion as it is the timestream with the lower density of points, the more spread points are less likely to be realized. On the right of Figure 4.3, the power spectral density of the white noise shown on the left is displayed. Note here that the power spectral density varies by 3dB, this is due to the differnece in sampling frequency between each simulated timestream. It

Parameter	Description	Value AR4	Value AR5/6
num_rows	number of rows to be multiplexed	64	55
row_len	number of 50MHz clock cycles that are spent per row during multiplexing.	100	100
data_rate	Time between data packets measured in frame periods. [1]	26	23

Table 4.1: MCE parameters used in regular observation mode. These parameters set the sampling frequency according to equation 4.8 and 4.9.

can be shown that the conserved quantity here is the power (in the signal analysis sense, not the physical sense) in the signal and after compensating for the bandwidth of each timestream, the total power in each timestream is constant.

4.5 Measuring aliased noise in Advanced ACTPol

In order to measure aliased noise in Advanced ACT we measure detector noise at high sampling rates (higher than the ones use in normal observation mode). It is possible to achieve this by re-configuring the data acquisition mode in the Multi Channel Electronics (MCE) to read less rows in the array and thus revisit each row more often increasing the sampling frequency.

The time-domain readout used by the MCE reads detectors in the same column sequentially in rows. The Advanced ACTPol array has 32 columns and the number of rows is 64 for AR4 and 55 for AR5 and AR6. The sampling frequency is then given by the internal clock of the MCE (50MHz) which sets the

[1] A frame period is the amount of time required for the multiplexer to address all the rows on a MUX

cam	num_rows	row_len	data_rate	f_s[kHz]	$f_{s\_readout}$[kHz]
AR4	4,8,16,32,64	100	26	18,36,72,144,288	0.3,0.6,1.2,2.4,4.8
AR5	4,8,16,32,55	100	23	24,41,82,163,326	0.4,0.7,1.4,2.7,5.4

Table 4.2: Number of rows set to be read in the noise measurements.

minimum amount of time the MCE can spend in one single detector and the number of samples that are bunched to make one single sample. The sampling rate internal to the MCE is then

$$f_s = \frac{50MHz}{num\_rows \times row\_len} \tag{4.8}$$

where *num_rows* is the number of rows that are being read out and *row_len* is the number of clock cycles that are spent per row during multiplexing. These samples are taken and then down-sampled via a digital Butterworth filter implemented in the MCE firmware. The sampling rate that is available to the user is then

$$f_{s\_readout} = \frac{50MHz}{num\_rows \times row\_len \times data\_rate}. \tag{4.9}$$

Table 4.1 shows a summary of these parameters and typical values used during observation. Figure 4.4 shows the digital filter at five sampling frequencies realized in the acquisition. Dotted lines indicate the frequency at which the gain of the filter falls 1%.

Data was acquired with reflective covers on the entrance of the optics tubes so the detectors see cold light from the inside of the cryostat reflected on them. Table 4.2 shows the parameters used to aquire the data and the resulting sampling frequencies.

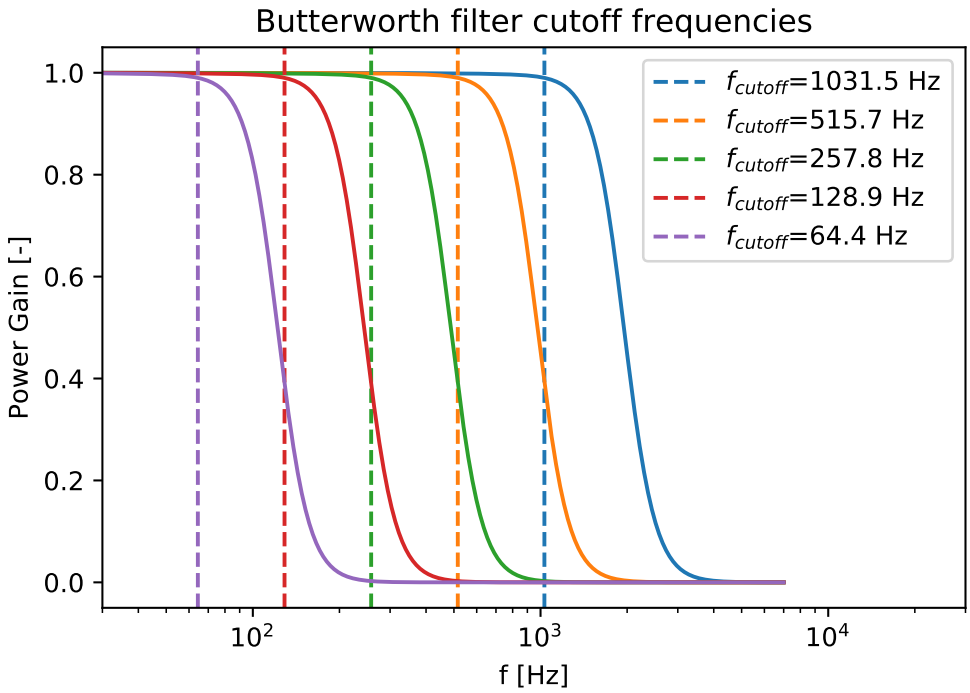

Figure 4.4: Digital filter gain for AR4.

4.6 The Dataset

We have acquired datasets corresponding to the sampling frequencies described in table 4.2 for all three arrays. We also swept the bias point of the arrays from 90% to 40% (in that order) and acquired noise with the bias turned off. The acquisition sequence is described in Algorithm 1. Data was acquired on June 14^{th} 2019, a day where the atmospheric weather conditions were unsuitable for CMB observations due to atmosphere opacity (PWV > 3 mm). Reflective covers (aluminum foil) were put on front of the receiver camera. Figure 4.5 shows a picture taken by Max Fankhanel and Rodrigo Quiroga our site engineers who were at the site assisting with this experiment.

Algorithm 1: Data acquisition sequence pesudocode.

```
for bias_point in [90, 80, 70, 60, 50, 40] do
    Change Bias Point(bias_point)
    Take IV curve
    Wait 5 min
    for num_rows in [4, 8, 16, 32, MaxRows] do
        Acquire data(num_rows)
Turn Off Bias
for num_rows in [4, 8, 16, 32, MaxRows] do
    Acquire data(num_rows)
```

Figure 4.5: Picture showing the Advanced ACTPol camera covered by aluminum foil reflective covers. Picture credit: Rodrigo Quiroga.

Acquisition was done in parallel in all three arrays (named PA4, PA5 and PA6), which took 3 hours and transfer from the high site to our computers at Cornell took about a day (bandwidth was intentionally limited to not disrupt operations at the site). In total we generated 24.6GB of data.

We confirm the detectors were correctly biased in the transition by plotting their noise power spectral density as the bias point was varied. If detectors are properly biased in the transition, the power spectral density is expected to decrease for an increasing bias point (expressed as a percentage of the normal resistance) as shown in Figure 3 (right) in reference [36]. Figure 4.6 shows this dependence.

4.7 Noise aliasing estimate

We measure detector noise using the prescription given in the previous section. The noise acquired as a time series is then decomposed into frequencies via a periodogram (using the Welch method implemented in scipy) which returns the power spectral density (psd) as a function of frequency. The psd is then averaged over a band of interest (between 10 and 60Hz) and an average power spectral density is computed. We have run numerical experiments showing that the returned power spectral density is well normalized and that the psd amplitude does not depend on the sampling frequency nor the length of the data acquisition to discard artifacts coming from the periodogram implementation in use.

We note the presence of some artifacts in the data, mainly of two kinds: jump giltches, which correspond to drifts in the temperature in the array af-

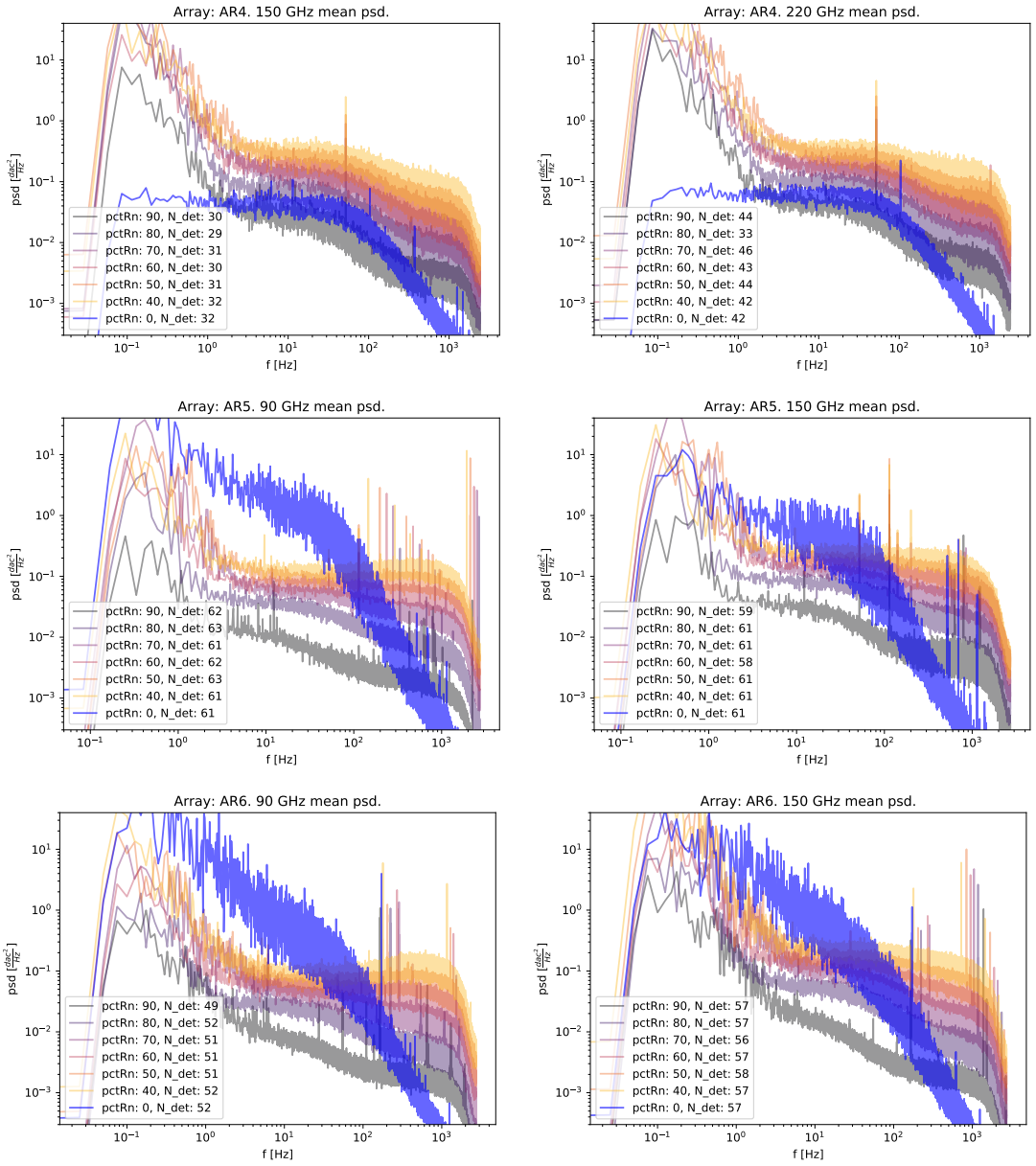

Figure 4.6: From top to bottom: high sampling rate detector noise power spectral density for AR4 (left 150, right 220 GHz), AR5 (left 90, right 150GHz) and AR6 (left 90, right 150 GHz). Data displayed was taken by reading only four rows.

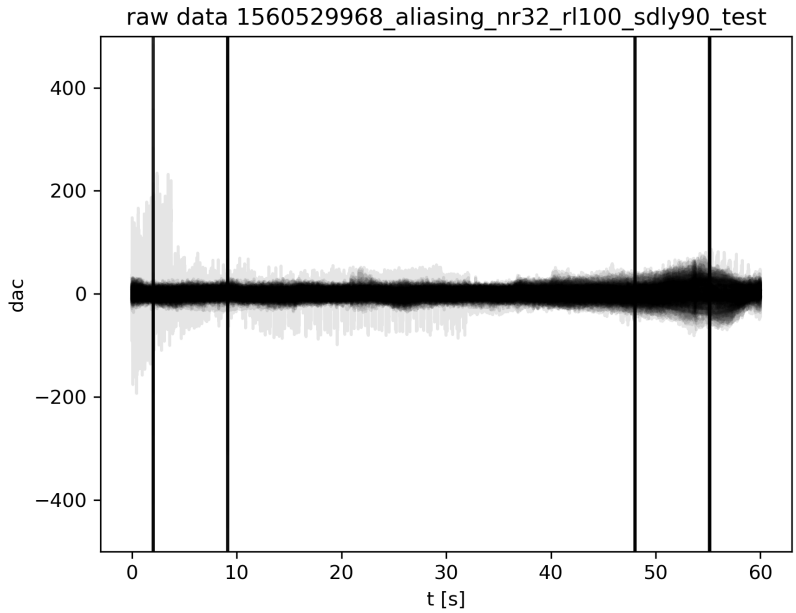

Figure 4.7: Example of the first four rows in the array overplotted for one noise observation. The dark regions show that different detectors are detecting the same signal. In this case there are four glitches that we interpret as cosmic ray hits.

ter a current-voltage (IV) curve (this is needed to get a calibration in power units) has been acquired and short duration, high amplitude glitches, which are most likely due to cosmic ray hits. We find that jump glitches can be limited in number of occurrences if we let the array temperature stabilize after the iv curve acquisition. We wait 5 minutes from IV curve to data acquisition to minimize this artifact. The data presented here shows essentially no jumps. The short duration glitches however can not be minimized by selecting acquisition parameters (we think these short duration glitches are due to cosmic ray hits). We observe that in a data acquisition of length 1 minute, one or two cosmic ray hits are typical. Some are extended to all the detectors in the array, while some are localized.

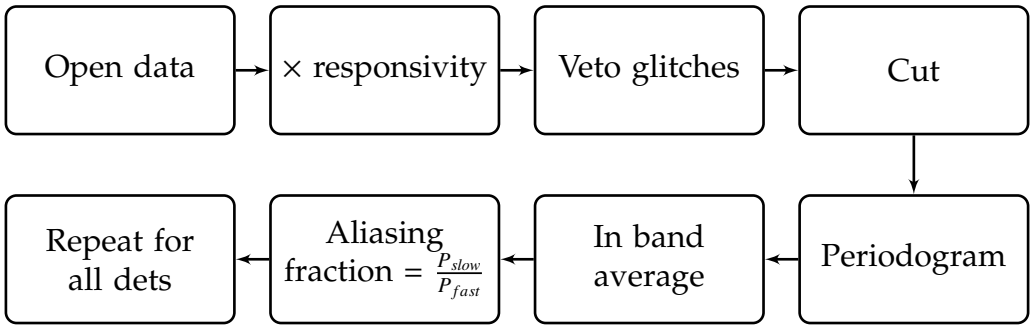

Figure 4.8: Diagram showing how the data was processed.

In post-processing, to minimize the number of cosmic ray hits in the data, before running our pipeline, we over-plot the four rows of interest (128 detectors) and visually look for regions that have no cosmic ray hits and where the noise seems to be time independent. Figure 4.7 shows one example. We then proceed to cut out the longest region where there are no short duration glitches. We find that this part in the analysis is important, as a single cosmic ray hit lifts the noise floor more than what we can tolerate for this measurement (percent level). We fit a sixth order polynomial in the time domain to equalize the baselines and detrend. This step is justified as we are interested in uncorrelated noise. This removes the majority of the $1/f$ noise from thermal fluctuations giving a $1/f$ knee at about 5 Hz or lower when in the transition. Superconducting data shows negligible $1/f$ noise in AR4 but more severe $1/f$ noise in AR5 and AR6. We note that the superconducting data is not used in the estimates of aliased noise presented here.

For each noise observation we compute the PSD and average the in-band power spectral density. The estimate of the mean PSD has an uncertainty (measured as $\sigma/\sqrt{N}$ with N the number of independent frequency samples) of (3-2)% depending on how much data was vetoed in the time domain due to glitches (longer noise observations have a lower uncertainty in the PSD). Using this pro-

cedure we define P_{slow} as the mean power spectral density in the band of interest for the nominal sampling frequency (300Hz for AR4 and 400Hz for PA5 and PA6) and P_{fast} as the mean power spectral density in the band of interest for a fast acquisition frequency (taken by multiplexing only 4 rows). We define the aliasing fraction as

$$AliasingFraction = \frac{P_{slow}}{P_{fast}} \left[\frac{pW^2/Hz}{pW^2/Hz} \right]. \tag{4.10}$$

Where in brackets we have specified the units we used for the mean power spectral density.

After the aliasing fraction extraction we compute statistics by discarding the detectors that show an aliasing fraction lower than 0.5 and higher than 1.5. This cut will be discussed in section 4.8 but essentially its purpose is to discard detectors that are not working. We split the data into two populations per array based on the detector type (there are detectors for two different optical frequencies in each array PA4: 150 GHz and 220 GHz, PA5 and PA6: 90 GHz and 150 GHz) and make separate histograms based on detector type. We compute the mean of the distribution and estimate the error as $\sigma_\mu = \frac{\sigma}{\sqrt{N}}$ with N the number of detectors considered in the average.

4.8 Aliasing Fraction Distribution Monte Carlo Simulation

In order to justify the outlier cut used in the analysis ($Aliasing\_Fraction \in [0.5, 1.5]$) and to predict what the distribution of aliasing fractions would look like, we write a Monte Carlo simulation where we want to estimate the distribution of the aliasing fractions given the spread in the estimate for the mean

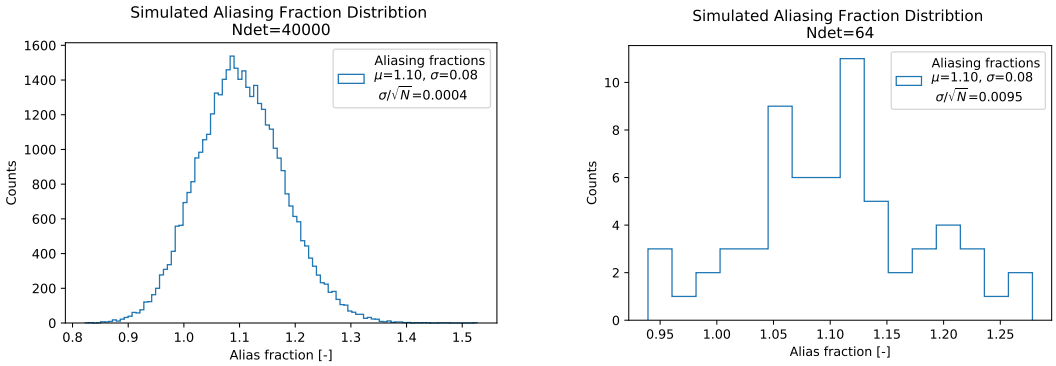

Figure 4.9: Simulated aliasing fraction histogram. On the left, the distribution for a large number (40000) of realizations. Right: histogram for 64 realizations (similar to the number of detectors present in the data).

power spectral density. From this distribution we can assess the likelihood of an aliasing fraction estimate being outside of the outlier cut.

The estimate of the mean power spectral density has a typical error of 3%. We draw simulated mean spectral densities from a normal distribution $\sim \mathcal{N}(\mu, \sigma)$. If we normalize by the high frequency noise PSD level, and we assume a true aliasing fraction of 10% that is equal for all detectors then we can use

$$P_{slow} \sim \mathcal{N}(1.1, 0.03) \tag{4.11}$$

$$P_{fast} \sim \mathcal{N}(1.0, 0.03). \tag{4.12}$$

Computing the aliasing fraction as $Aliasing\_Fraction = \frac{P_{slow}}{P_{fast}}$ we get a distribution shown in Figure 4.9, notice that on the left Figure the number of simulated detectors is 40000 and on the right we simulated a histogram with the number of detectors we expect to get from the data. Note that even for a low number of detectors like the one in figure 4.9 (right), we can recover the mean with a 1% error assuming identical distributions.

Note from Figure 4.9 (left) that the alising fraction histogram shows essencially no realizations under 0.5 or above 1.5. Given this I estimate the probability of such a measurement lower than $1/40000 = 2.5 \times 10^{-5}$ which justifies the cut I have established to clean up the data from outliers coming from non-working detectors.

4.9 Results

At 50% R_n we obtain aliasing fractions of 1.05, 1.03 and 1.05 ±0.01 at 150 GHz in PA4, PA5 and PA6 respectively. The 90 GHz detectors showed aliasing fractions of 1.07 and 1.1 ±0.01 in PA5 and PA6. The 220 GHz detectors on PA4 showed aliasing fraction of 1.10 ± 0.2. Figure 4.11 shows histograms of these metrics. Figure 4.12 shows the evolution of the aliasing fraction as a function of the bias point in percentage of the normal resistance.

An estimate for an effective PWV can be made by comparing the number of detectors within cut for the covers-on tests to what has been observed through routine observations. For PA4 the data shows (see figure 4.10) an effective PWV between 1.7 and 2.3 mm, for $\sim$ 1100 detectors within cut.

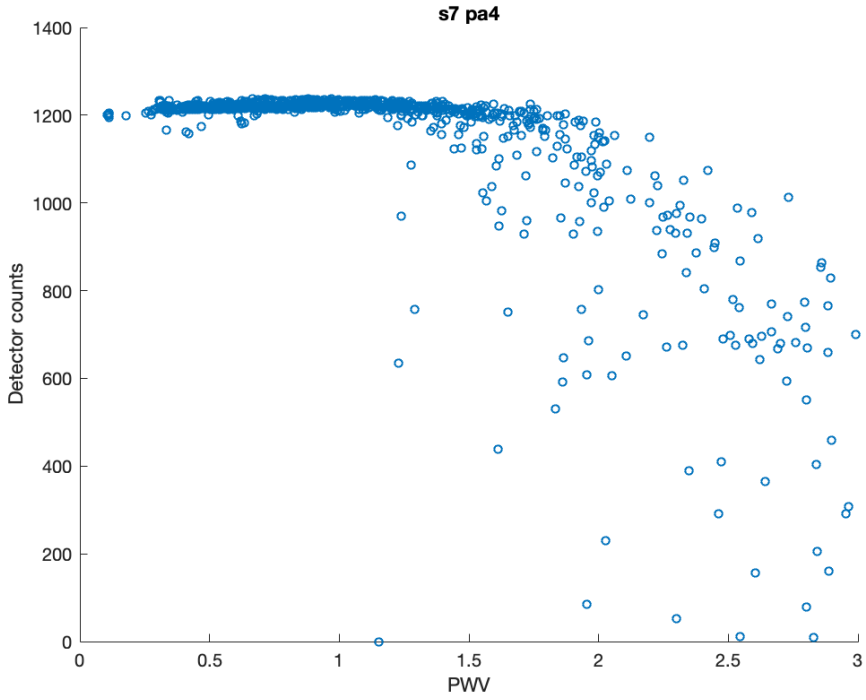

Figure 4.10: Precipitable water vapor (PWV) as a function of detectors within cut for PA4, season S7. In our measurements IV curves with covers on returned $\sim$ 1100 detectors within cut which corresponds to an effective PWV $\sim$ 2. Figure provided by Patty Ho.

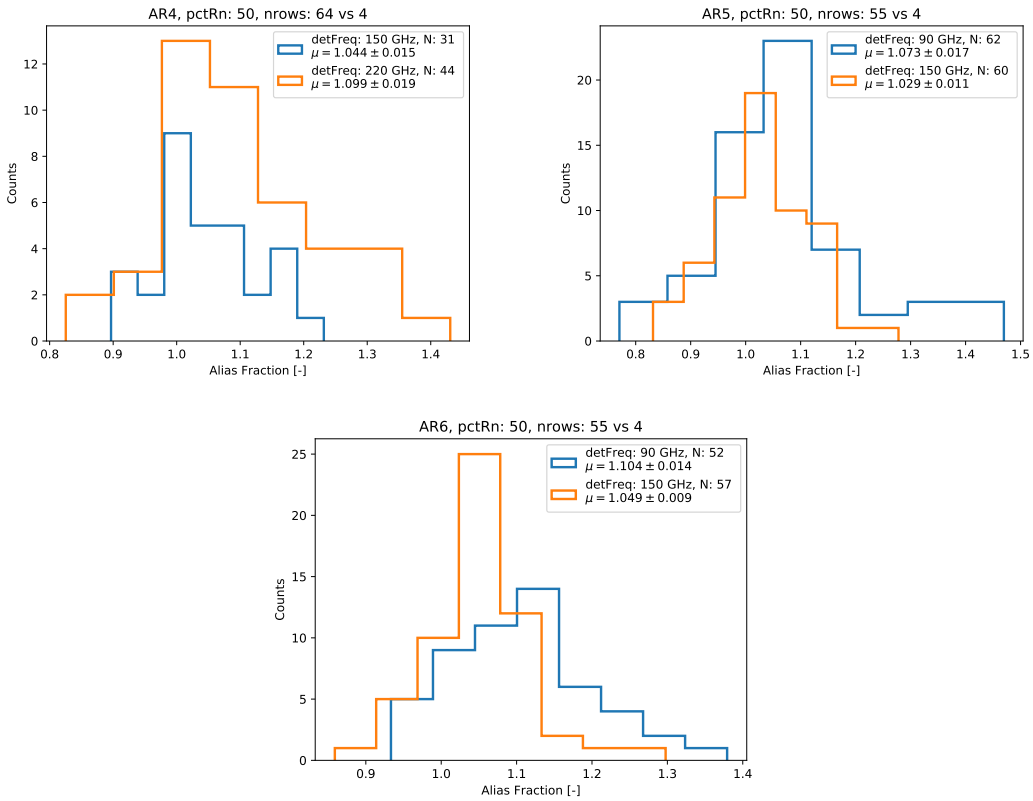

Figure 4.11: Histograms showing the measured aliasing fraction from three arrays split by detector frequency. Bias point is 50%R_n and aliasing fraction compares the nominal sampling frequency to the sampling frequency obtained when multiplexing the first 4 rows.

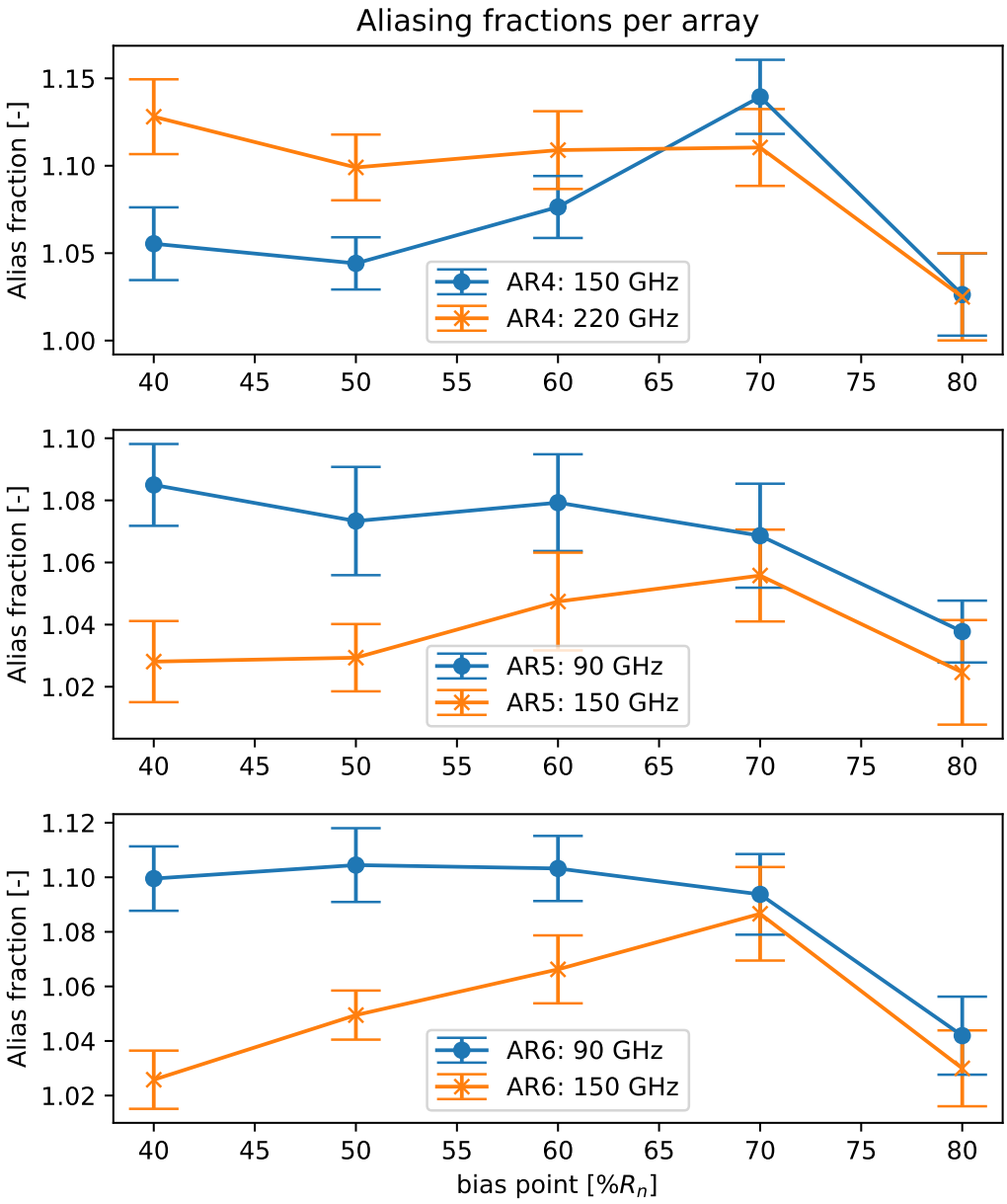

Figure 4.12: Per array aliasing fractions as a function of bias point expressed as a percentage of the normal resistance.

CHAPTER 5

THE SUNYAEV-ZELDOVICH EFFECT

5.1 The Sunyaev-Zeldovich Effect

The Sunyaev-Zeldovich (SZ) effect, first proposed in the late 60s [66], has been proven to be a powerful observational tool for cosmology. The ever increasing sensitivity, sky and frequency coverage of modern CMB experiments allow large numbers of detections of galaxy clusters via the SZ effect which can be used to improve cosmological parameter constraints and to probe the large scale structure of the universe.

The thermal SZ effect is the spectral distortion of the CMB light (schematically shown on Figure 5.1) due to inverse Compton scattering. The thermal SZ effect is insensitive to cosmological dimming as the ratio of the intensity of the CMB to the SZ effect is not affected by redshift, making it a great probe of cluster abundance over time. The redshift evolution of the cluster density is critically affected by the cosmology and thus the SZ effect is a probe of the dark energy equation of state.

Spectral distortions of the thermal Sunyaev-Zeldovich effect due to the movements of clusters of galaxies are referred to as the kinetic Sunyaev-Zeldovich (kSZ) effect. The kSZ offers a way to study the kinematics of the large scale structure of the universe.

In this chapter, I give an overview of the thermal and kinetic Sunyaev-Zeldovich effects and I show my work extracting the kSZ signal from the ACTPol data.

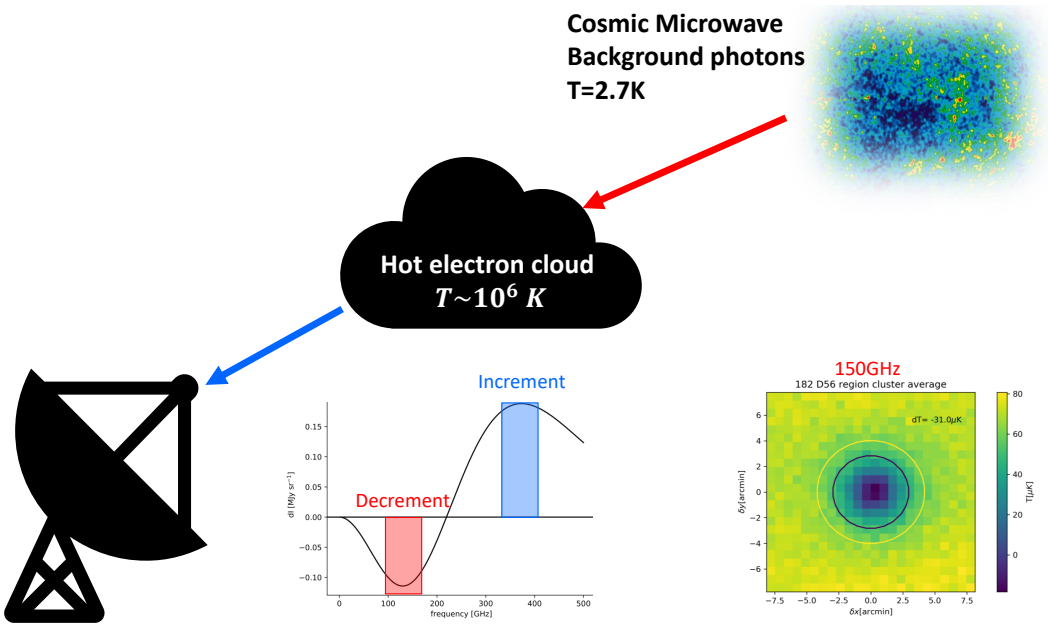

Figure 5.1: Thermal Sunyaev-Zeldovich effect diagram. Cold light from the CMB interacts with a hot electron cloud surrounding a cluster of galaxies. Inverse Compton scattered light has then a distorted spectrum. This distortion is manifested as a decrement in the CMB.

5.2 The thermal Sunyaev Zeldovich effect

The thermal Sunyaev Zeldovich effect (tSZ) is the small distortion of the CMB frequency spectrum caused by the inverse Compton (cold photon-hot electron) scattering of the CMB photons on the electrons of the ionized inter-cluster medium (ICM) gas. Light coming from the CMB has a low probability (less than 1%) of interaction with an ICM electron. Due to the high energy of the ICM electrons, the absorbed photon will be reemited in a different frequency and the resulting photon will show a small (<1 mK) energy boost.

The spectral distortion of the CMB, in normalized frequency units $x = \frac{h\nu}{k_B T_{CMB}}$

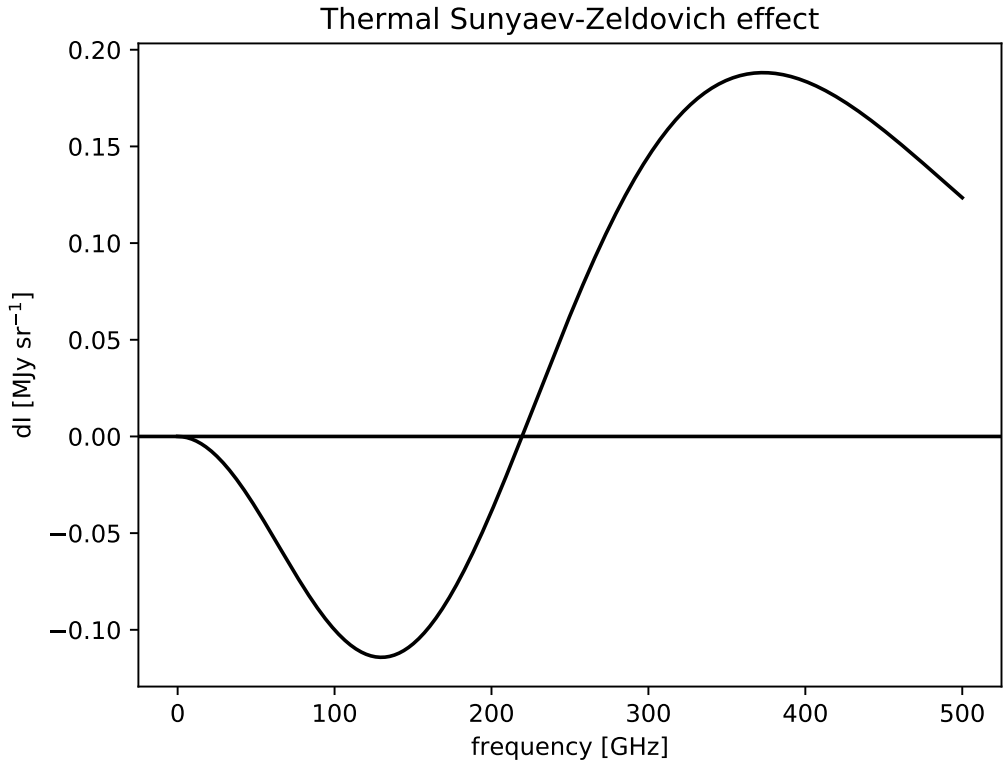

Figure 5.2: Thermal Sunyaev Zeldovich effect frequency dependence. The effect shows a minimum at roughly 150 GHz. The CMB will then show a decrement when observed at 150 GHz by a CMB experiment.

is given by

$$\frac{\delta T_{tSZ}}{T_{CMB}} = f(x)y \tag{5.1}$$

where y, the Compton parameter, is the integral of the pressure

$$y = \int n_e \frac{kT_e}{m_e c^2} \sigma_T dl, \tag{5.2}$$

where n_e is the electron number density, k is the Boltzman constant, T_e is the electron temperature, m_e and c are the usual mass of the electron and the speed of light respectively. The Compton parameter for an isothermal cluster equals the optical depth τ_e times the fractional energy gain per scattering.

The frequency dependence (in the non-relativistic case) is given by

$$f(x) = \left(x \frac{e^x + 1}{e^x - 1} - 4 \right). \tag{5.3}$$

Expressing the tSZ effect in units of specific intensity, the temperature increment is given by

$$\Delta I_{tSZ} = g(x) y, \tag{5.4}$$

where

$$g(x) = 2 \frac{(kT_{CMB})^3}{(hc)^2} \frac{x^4 e^x}{(e^x - 1)^2} f(x). \tag{5.5}$$

Figure 5.2 shows the frequency dependence of the tSZ effect for a cluster with $y = 10^{-4}$. Note that the tSZ effect has a minimum near 150 GHz, a null at 220 GHz and a maximum at 280 GHz, all bands accessible with ground-based CMB experiments. Figure 5.3 (top) shows The Bullet Cluster as seen in the ACT co-added map at 150 GHz. Optical and a filtered map from [45] are also shown (bottom).

Because the SZ effect is proportional to the integrated number density, the integral of the tSZ signal over the solid angle is proportional to the cluster mass, i.e.

$$\int \Delta T_{tSZ} d\Omega \propto \frac{N_e < T_e >}{D_A^2} \propto \frac{M < T_e >}{D_A^2} \tag{5.6}$$

where N_e is the number of electrons in the cluster, $< T_e >$ is the mean electron temperature, D_A is the angular diameter distance and M is the mass of the cluster. Here note that $D_A(z)$ is quite flat at high redshift, and because the energy density scales as $\frac{1}{(1+z)^3}$, high redshift clusters will be denser and hotter. So the tSZ signal is largely independent of redshift and the main parameter that matters for a detection of a survey is the cluster's mass.

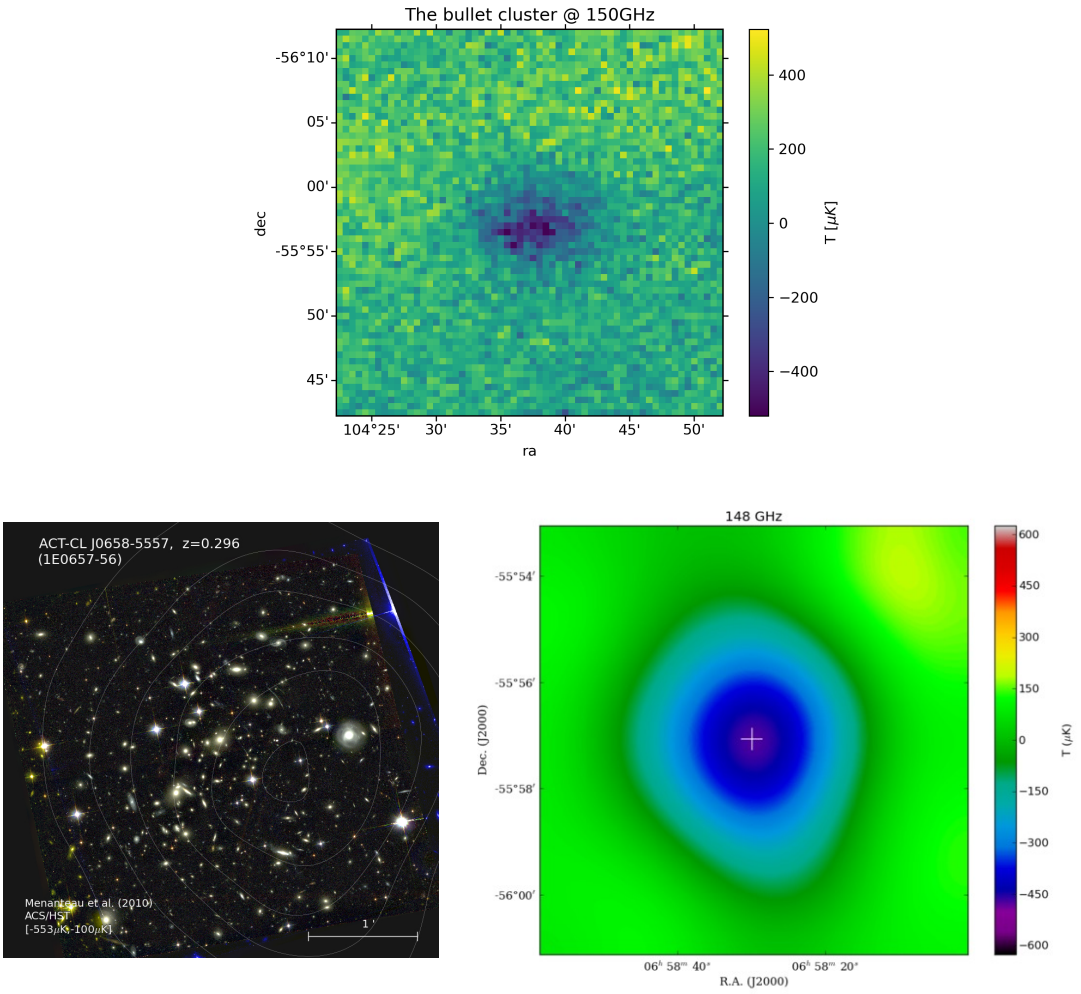

Figure 5.3: (Top) The bullet cluster from the ACT 150GHz co-added map. Note that for a CMB experiment, a cluster shows up like a deficit in surface brightness. (left) Optical image [45]. (right) ACT filtered SZ effect [45].

5.3 The kinetic Sunyaev Zeldovich effect

The SZ effect is also sensitive to Doppler shifts. If the cluster is moving with a velocity v then the SZ distortion will be given by

$$\frac{\Delta T_{SZ}}{T_{CMB}} = -\tau_e \left(\frac{v_{pec}}{c}\right). \tag{5.7}$$

In the non-relativistic limit, the kinetic Sunyaev Zeldovich effect (kSZ) is a purely thermal distortion in magnitude, i.e., the peculiar velocity of the cluster will shift the spectrum in such a way that it will be described by another Planck spectrum but at a different temperature. Note from equation 5.7 that the kSZ effect is small, as it is proportional to v/c. For a galaxy cluster with $v \sim 500\,\mathrm{km/s}$, $\frac{\Delta T}{T_{CMB}} \sim 10^{-3}\tau_e$.

5.3.1 The pairwise kSZ

The small amplitude of the kSZ makes its detection challenging for one given cluster for current sensitivity levels. The kSZ has been measured statistically [32, 6] via the average pairwise kSZ effect, which considers the kSZ line of sight component for an average of galaxy clusters at given separations (see Figure 5.4).

The growth structure parameter D_a and the growth rate

$$f_g(a) = \frac{d\log D_a}{d\log a} \tag{5.8}$$

can be used to parametrize the growth of structure. For a ΛCDM model of cosmology, the growth rate is

$$f_g(a) = \Omega_m^{\gamma}(a) \tag{5.9}$$

where $\gamma = 0.55$ for standard gravity and $\gamma \neq 0.55$ for modified gravity models.

Using linear theory [46], the mean pairwise velocity $v(r)$ between two dark matter particles at positions $\vec{r}_i$ and $\vec{r}_j$ at comoving separation $r = |\vec{r}_i - \vec{r}_j|$ is given by

$$v(r) = \frac{2}{3} f_g(a) H(a) a r \frac{\bar{\xi}(r,a)}{1+\xi(r,a)} \tag{5.10}$$

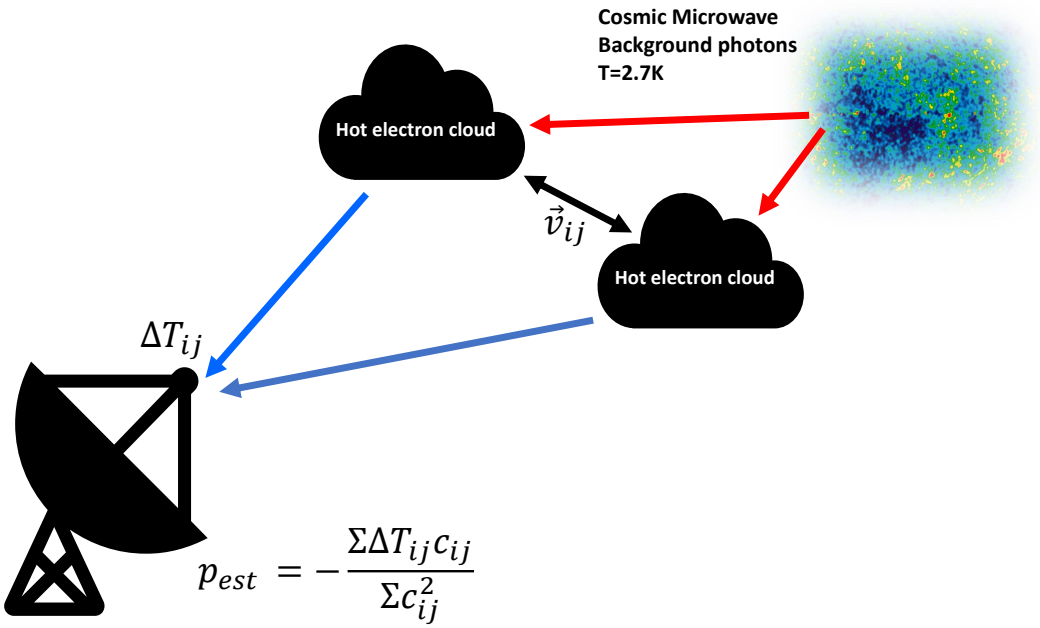

Figure 5.4: Diagram of the pairwise kSZ. Moving pairs of galaxies will present a distortion of the tSZ effect due to their motions. This signal can be extracted by averaging the differences in decrements across a large number of pairs of groups of galaxies and grouping them by separation

where ξ is the dark matter 2-point correlation function and $\bar{\xi}$ is the volume averaged correlation function according to

$$\xi(r,a) = \frac{1}{2\pi^2}\int dk k^2 j_0(kr) P(k,a) \tag{5.11}$$

$$\bar{\xi}(r,a) = \frac{3}{r^3}\int_0^r dr' r'^2 \xi(r,a) \tag{5.12}$$

where $P(k,a)$ is the dark matter power spectrum and

$$j_0(x) = \frac{sin(x)}{x} \tag{5.13}$$

the first order spherical Bessel function.

In practice, CMB surveys are sensitive to masses starting from a low range M_{min}, so the average velocities need to take this into account to be compared to a measured curve. In reference [46] a detailed discussion can be found.

5.3.2 The pairwise estimator

The mean pairwise momentum can be computed from the line of sight component of the momentum by using the estimator

$$p_{est}(r) = \frac{\sum_{i<j}(\boldsymbol{p}_i \cdot \boldsymbol{r}_i - \boldsymbol{p}_j \cdot \boldsymbol{r}_j)c_{ij}}{\sum_{i<j} c_{ij}^2} \tag{5.14}$$

where $\boldsymbol{r}_i$ is the position vector of the i-th object. The length of this vector can be computed from a catalog of redshifts as

$$D_c = \frac{c}{H_0}\int_0^z \frac{dz'}{\sqrt{\Omega_M(1+z)^3 + \Omega_\Lambda}}. \tag{5.15}$$

In equation 5.14, r is the separation distance from the objects $r = |\boldsymbol{r}_i - \boldsymbol{r}_j|$ and c_{ij} is a geometrical weight that downweights the momentum contribution from a pair if their separation does not lie on the line of sight ($r_i = r_j$)

$$c_{ij} = \boldsymbol{r}_{ij}\frac{\boldsymbol{r_i} + \boldsymbol{r_j}}{2} = \frac{(r_i - r_j)(1+\cos\theta)}{2(r_i^2 + r_j^2 - 2r_i r_j \cos\theta)} \tag{5.16}$$

where θ is the angular separation between a given pair of clusters.

The line of sight momentum is then linear with the temperature distortion

$$\Delta T_{kSZ} \propto -\boldsymbol{p_i} \cdot \boldsymbol{r_i} \tag{5.17}$$

and the proportionality constant is given by the properties of the clusters (like the angular distribution in the sky), pixelization and beam of the telescope.

Extraction of the kSZ signal for a given cluster pair is quite challenging as other effects are much larger. The main advantage of the use of the pairwise estimator is that being a differential estimator, it allows effects that are not a function of redshift to be subtracted.

We allow a redshift dependence by modeling it from the data via a Gaussian rolling average

$$\mathcal{T}(z) = \frac{dT_i(z_i)e^{-(z-z_i)^2/\sigma_z}}{\sum e^{-(z-z_i)^2/\sigma_z^2}}, \tag{5.18}$$

where dT_i is the temperature increment defined as $dT_i = T_{disk} - T_{ring}$ and z_i is the redshift of the galaxy in question. As it has been previously proposed in the literature [32, 14] we used $\sigma_z = 0.01$. We subtract the modeled redshift dependent temperature differential for each galaxy in the catalog with which the estimator becomes

$$p_{est} = -\frac{\sum_{i<j}((dT_i - \mathcal{T}(z_i)) - (dT_j - \mathcal{T}(z_j)))c_{ij}}{\sum_{i<j} c_{ij}^2}, \tag{5.19}$$

which is our estimator for the motions of galaxies for a given separation range.

5.3.3 Variance weighting the kSZ pairwise estimator

The map doesn't have the same noise level for each pixel. To improve our estimate of the pairwise momenta, we can use the noise in the map (which is a sub product of the map making process) to down-weight noisy regions of the map, giving more confidence to regions with low variance. Here I will give my derivation of how this weighting needs to be done by digging on the derivation of the pairwise estimator.

The Doppler shift affects the line of sight component of the velocities, but we observe the projection $s_a = \hat{r} \cdot \vec{v}_a$ instead of the full 3-D velocity $\vec{v}_a$. The pairwise velocity estimator probes the mean difference between radial velocities of pairs of galaxies

$$\langle s_a - s_b \rangle = v_{12}\hat{r} \cdot \frac{\hat{r}_1 + \hat{r}_2}{2} = p_{AB}\frac{v_{12}}{2} \tag{5.20}$$

where v_{12} is the pair velocity, $\hat{r} = \frac{\vec{r}_1 - \vec{r}_2}{|\vec{r}_1 - \vec{r}_2|}$ and $p_{AB} = \hat{r} \cdot (\hat{r}_1 + \hat{r}_2)$.

The pairwise estimator minimizes the sum of the squared error (see [22])

$$\chi^2 = \sum_{ab} [s_a - s_b - \frac{p_{ab} v_{12}}{2}]^2. \tag{5.21}$$

This kind of estimator is known in statistics as a Mean Square Error estimator (MSE).

The error is minimum when

$$\frac{\partial \chi^2}{\partial v_{12}} = 0 = \sum -2 p_{ab} [(s_a - s_b) - p_{ab} \frac{v_{12}}{2}]. \tag{5.22}$$

Solving for v_{12} yields

$$v_{12} = \frac{-2 \sum (s_a - s_b) p_{ab}}{\sum p_{ab}^2}, \tag{5.23}$$

which is the usual pairwise estimator we saw in section 5.3.2.

If we variance weight the square error, we get

$$\chi^2 = \sum [(s_a - s_b) - p_{ab} \frac{v_{12}}{2}]^2 \frac{1}{\sigma_{ab}^2} \tag{5.24}$$

which differentiates to

$$\frac{\partial \chi^2}{\partial v_{12}} = \sum -p_{ab} [(s_a - s_b) - p_{ab} \frac{v_{12}}{2}] \frac{p_{ab}}{\sigma_{ab}^2} = 0 \tag{5.25}$$

and again, solving for v_{12} gives

$$v_{12} = \frac{-2 \sum (s_a - s_b) p_{ab} / \sigma_{ab}^2}{\sum p_{ab}^2 / \sigma_{ab}^2}. \tag{5.26}$$

For the variance of a pair we can use the usual formula $\sigma_{ab}^2 = \sigma_a^2 + \sigma_b^2$.

5.4 Resampling methods

We use resampling methods to estimate confidence intervals from the data. Methods like the jackknife and the bootstrap are often used in cases where the estimator is difficult to evaluate analytically or lacks closed form. These methods consist in inferring the probability distribution of the estimator by evaluating its numerical stability, by reproducing a sample of length equal (bootstrap) or smaller (jackknife) than the original sampled population for which we want to compute the estimator.

In the case of the kSZ curve we used a jackknife method to find the error bar of the estimator. I review resampling methods (of which the jackknife is a particular case) to give a context of the statistical tools used to get the error bars of the measurement.

5.4.1 The bootstrap method

Let X be a random variable. We perform an experiment and measure a list of N X_i values. The random variable $f(X)$ is our random variable of interest. We would like to obtain the distribution of $f(X)$ or at least its mean and standard deviation.

The bootstrap method consists of replicating the distribution of the random variable X by resampling *with replacement* the measured data. If the number of samples is large enough and the sampled data are not correlated or biased, the distribution of the random variable X can be replicated by this method and therefore by numeric evaluation we can recreate the histogram of $f(X)$.

Algorithmically the method can be summarized as follows:

1. List the N observations.
2. Randomly select N samples from the pool of N observations with replacement.
3. Run $f(X_i)$ for a large number of replicant samples.
4. Make histograms, compute standard deviations or percentiles.

In practice, the number of replicant samples does not need to be extremely large to get an accurate errorbar, and numbers as low as 200 are reported in the literature.

When does the bootstrap method fail? If the function we are evaluating does not admit repeated values, the bootstrap might get us into trouble. Given that the pairwise estimator does not allow for repeated values (what does it mean to have a pair of galaxies composed of galaxy A and itself?), we use the jackknife method instead.

5.4.2 The jackknife method

Let X be a random variable. The problem consists in estimating the mean (μ) and a standard error (σ) for some estimator ($F(X)$) from a set of observations X_i. This method evaluates the standard error in the mean of the estimator by removing a subset (one or many) of observations and evaluating the estimator repeatedly to assess how noisy the estimator is to the input data.

The most common type of jackknife is the so called "delete 1" jackknife, where the ensemble of observations X_{-i} is defined as the pool of N observations with the observation i removed. Partial estimators are computed from the X_{-i}. For example if the estimator is the mean then

$$\chi_{-i} = \frac{1}{N-1}\sum_{k\neq i} X_k. \tag{5.27}$$

With this quantity, the estimator for the standard error in the mean value of X is

$$SE_{jackknife} = \sqrt{\frac{N-1}{N}\sum_{i=1}^{N}(\chi_{-i} - \chi_{(.)})^2} \tag{5.28}$$

where $\chi_{(.)} = \sum \chi_{-i}/N$. Note that the factor (N-1) differentiates this estimator from the sample variance of χ. In statistics this is called an inflation factor to make the estimator χ unbiased. Conceptually this factor takes care of the fact that the range of χ is very similar to the value of the full observation (since we only remove one sample at a time). The sample space that the jackknife estimator generates is smaller than the one of the bootstrap.

Other jackknife variants are the delete-d jackknife and the group-g jackknife. These estimators are helpful when the numerical evaluation of $F(X)$ is problematic. For example, given $F(X_{-i})$ is so close to F_N, the estimator F (represented as a floating point number of finite precision) might not change at all when evaluating the jackknife and then the estimator will be dominated by rounding errors. In the delete-d jackknife random groups of length d are removed yielding a great number of possible combinations, making this method computationally expensive for large samples of data. In the group-g jackknife we generate g groups with $h = N/g$ samples each, and evaluate the estimator with each group of observations. This gives a balance between robustness to numerical noise and computational cost.

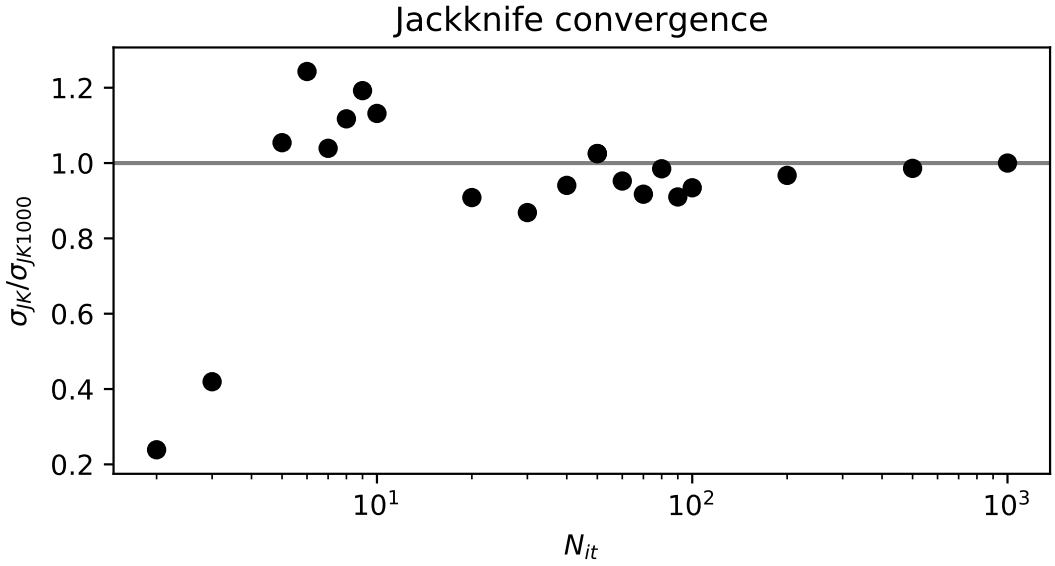

Figure 5.5: Jackknife convergence. Here we show one jackknife errorbar run for a varying number of jackknife iterations. Amplitude of the jackknife errorbar has been normalized to the 1000 iteration jackknife. Note that for a low number of jackknife iterations, the error in the variance is around 20%, while for 50 iterations the error is around 10%. Over 100 jackknife iterations the error in σ_{JK} is lower than 5%. In this work we report confidence intervals for 50 iterations.

In Figure 5.5 we show one convergence curve of one run of the pairwise estimator presented in this work, computed via a group-g jackknife of increasing g.

5.4.3 Covariance

For a set of estimators p_n^k, where n indexes estimators and k indexes the jackknife observation, the jackknife covariance matrix is

$$C_{m,n} = \frac{N-1}{N} \sum_{k=1}^{N} (p_m^k - \bar{p}_m)(p_n^k - \bar{p}_n) \tag{5.29}$$

Note here that in the sample variance jackknife estimator, the prefactor $N-1$ inflates the covariance in the same way it does it for the variance.

It is also common practice to use the Pearson correlation matrix to display this graphically. In this case, the correlation matrix is defined as

$$r_{xy} = \frac{\sum(x_i - \bar{x})(y_i - \bar{y})}{\sqrt{\sum(x_i - \bar{x})^2 \sum(y_i - \bar{y})^2}} \tag{5.30}$$

Note here that the jackknife normalization factor cancels out and can be left out. For more detail on resampling methods the reader can consult [20].

5.5 The dataset

The kSZ calculation uses an optical catalog with optical magnitudes and measured redshifts. We use the position on the sky of the galaxies in the catalog to extract the aperture photometry (discussed in section 5.6) around the position of individual galaxies from the ACT map. Figure 5.6 shows the density of galaxies per square degree on the sky. The magnitude in different bands (ugriz) and redshift are used to compute the luminosity of galaxies. Figure 5.7 shows histograms of the redshift and luminosities from the k-corrected catalog. The luminosity of a galaxy is expected to follow the galaxy's mass and therefore to correlate with the strongest SZ signal.

We use the redshift to generate the radial distance following equation 5.15,

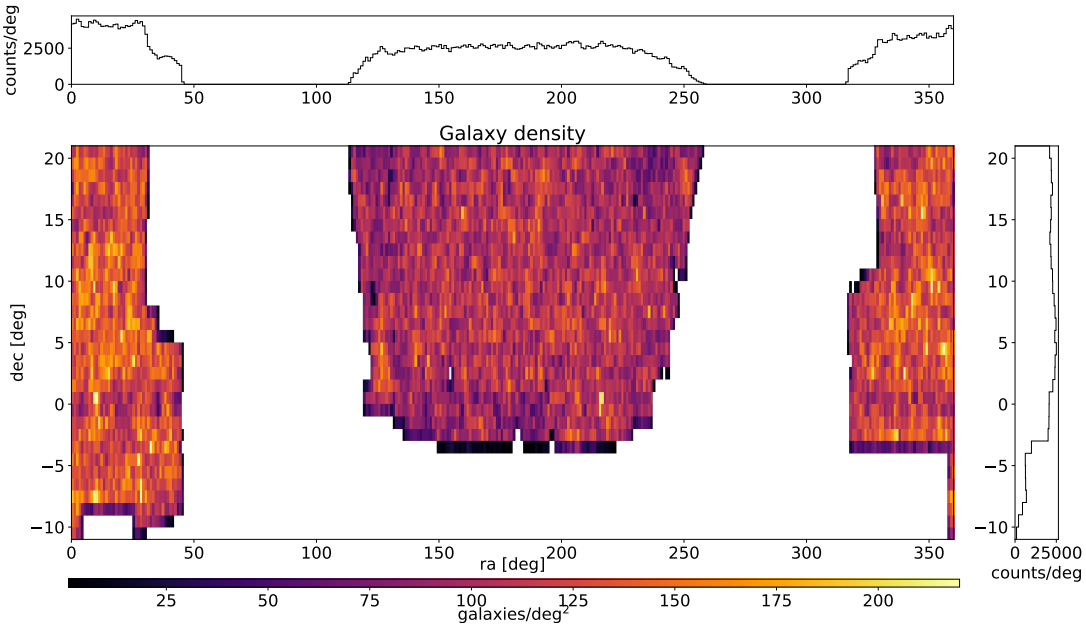

Figure 5.6: Catalog Galaxy density.

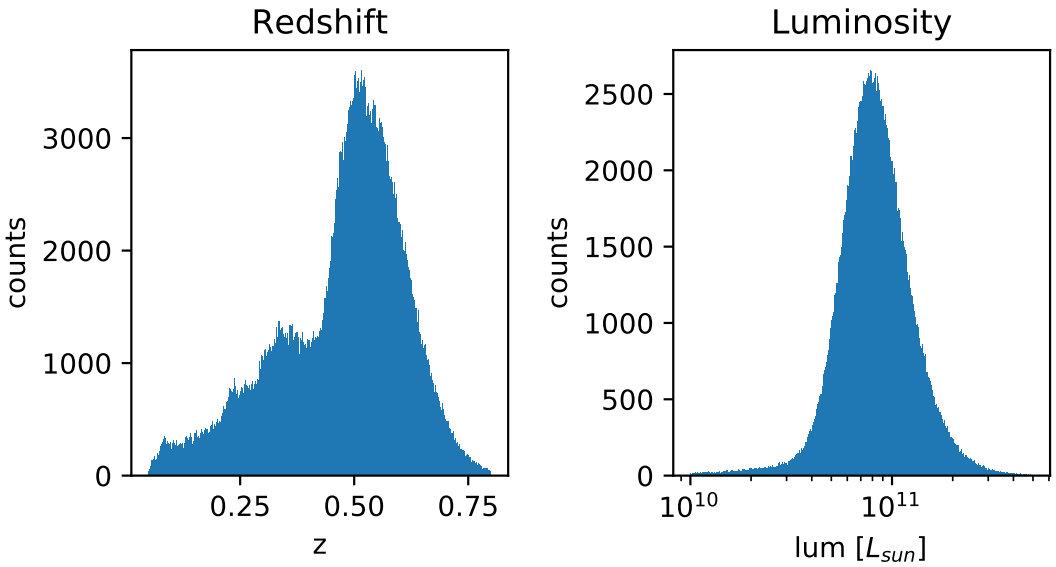

Figure 5.7: Luminosity and redshift catalog distributions.

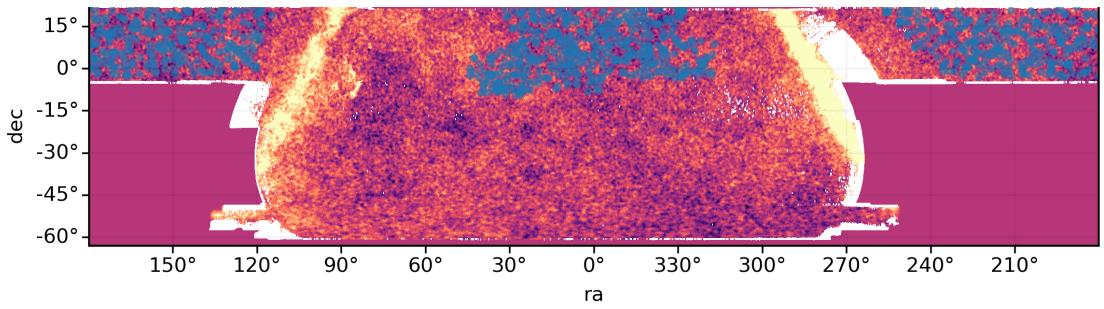

Figure 5.8: ACT co-added map and catalog coverage. Hundreds of randomly selected galaxies are shown as blue dots. Note that the ACT map covers areas of the sky not covered by the galaxy catalog.

which in turn is used to compute the pairwise distance. The conversion from optical magnitude and redshift to luminosity is a process known in astronomy as a k-correction, which uses templates of observed galaxies and their distance to estimate a total integrated luminosity. Table 5.1 shows the first rows of the k-corrected catalog. This work was done by VC following the conventions described in [9]. The catalog itself is generated using scripts written by EV, and come from the Sloan SDSS catalog [65]. Figure 5.8 shows (in blue dots) the area covered by the catalog superposed to the map used in this study.

We used the ACT co-added map [47] to extract the aperture photometry. Figure 5.8 shows the map which covers 360 deg in right ascension and 20 deg in declination (though a larger area is covered non-uniformly in ra-dec).

In addition to the ACT map, we also use the inverse variance map. This map is a sub-product of the map making process and indicates how good the estimate of the value of each pixel is. Because we use the pixel values from the map to estimate the kSZ curve, the uncertainty from each pixel propagates directly to the uncertainty in the estimated velocity curve. The way this error propagates

ra	dec	lum	z	PScut	divcut	galcut
1.89e+02	1.01e+00	1.28e+11	6.90e-01	1	2	2
1.89e+02	9.33e-01	5.09e+10	4.74e-01	1	2	2
1.89e+02	9.92e-01	5.77e+10	5.75e-01	1	2	2
1.89e+02	1.03e+00	1.03e+11	6.95e-01	1	2	2
1.89e+02	1.00e+00	1.06e+11	6.95e-01	1	2	2

Table 5.1: First 5 rows of our k-corrected catalog. Each row corresponds to a galaxy. The catalog contains 602461 galaxies. PScut flags galaxies near a region of known point sources, divcut selects galaxies based on the variance they have in the map, galcut selects galaxies depending on their distance to the galactic plane.

depends exactly on the distribution of galaxies in the sky and the distribution of the inverse variance map. To build intuition about the uncertainties on the map, I ran my aperture photometry code on the inverse variance map to get an average variance for each galaxy position. Figure 5.9 shows histograms of the number counts of galaxies for different values on the variance map. Figure 5.10 shows the distribution of the map variance on the sky after averaging neighbouring galaxies. Note that the variance of the map changes drastically across the sky; this is expected from the way the observations are scheduled.

5.6 Aperture Photometry

One problem that affects how the aperture photometry is done arises from the inter-pixel positions of galaxies from the catalog. When the map has to be evaluated at a point between the center of two pixels, a statement about the interpolation scheme that is being used needs to be made. In FDB 2017 [14], a nearest neighbor interpolation was used and the galaxy position was replaced by the center of the closest pixel. This approach has the advantage of being simple and

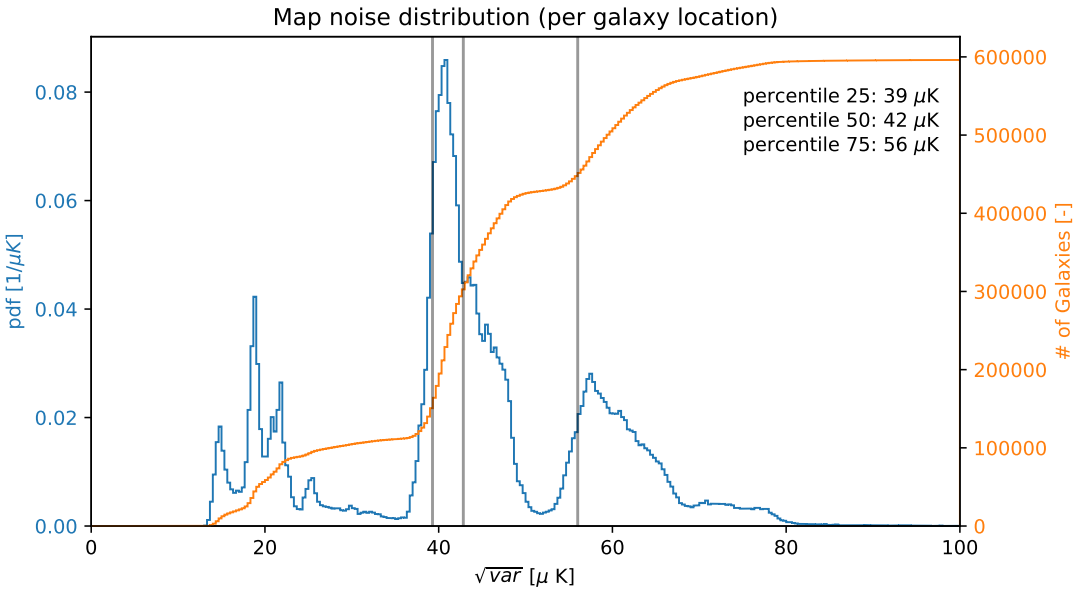

Figure 5.9: Distribution of map variance for the catalog galaxy positions.

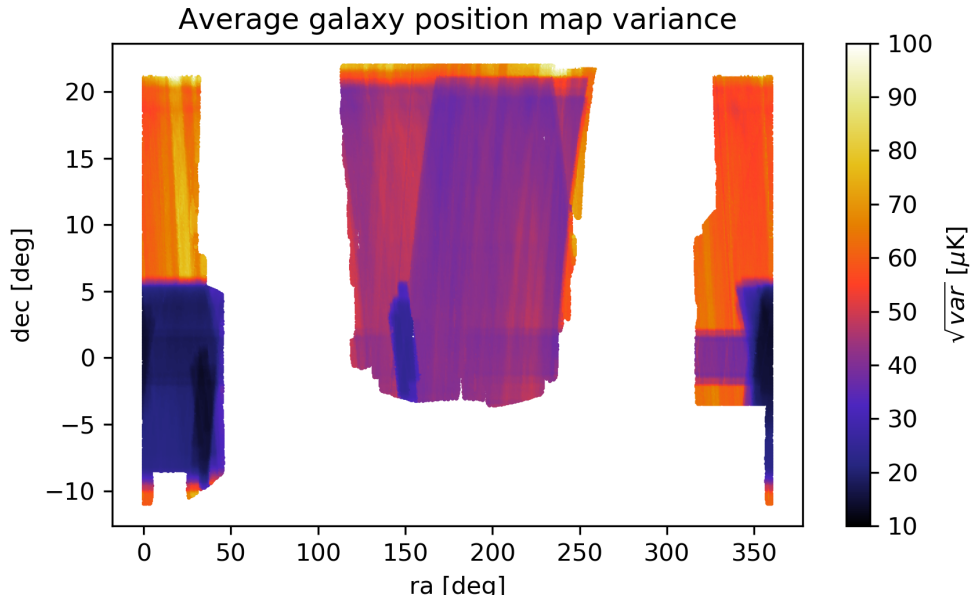

Figure 5.10: Average map variance for all the galaxy positions in the catalog. The variance in the map follows the number of times the telescope has observed a given region.

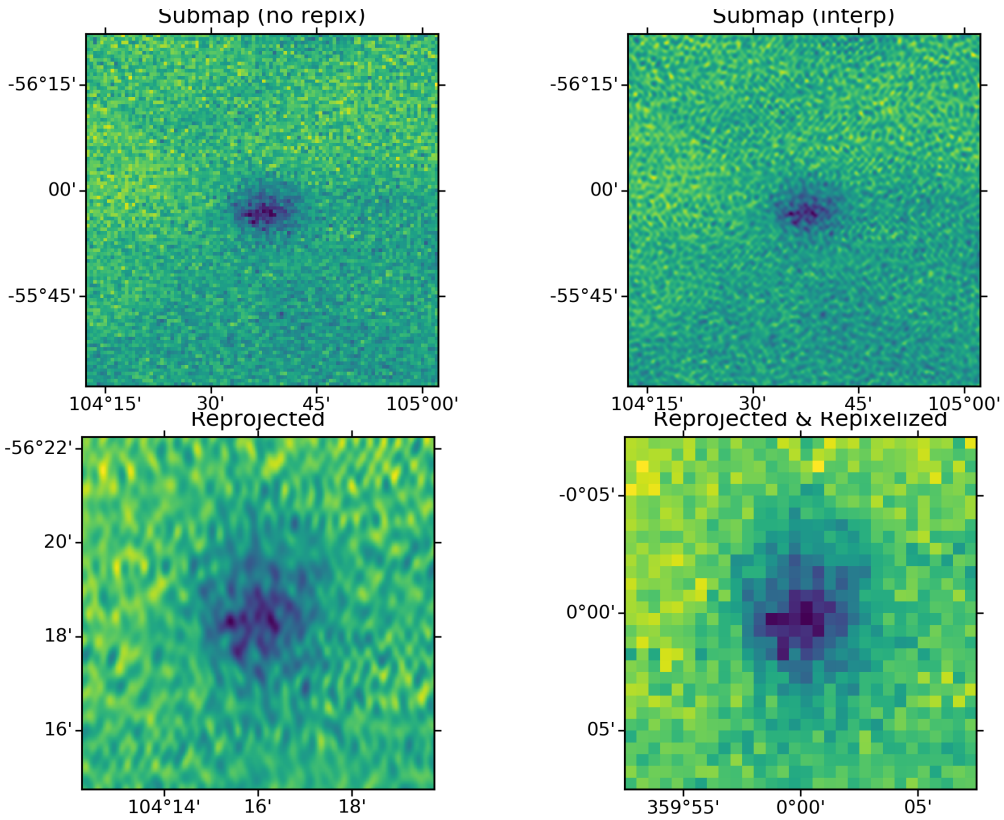

Figure 5.11: Repixelization steps. Top left: Submap extracted around the Bullet cluster position. Top right: interpolated submap to increase the resolution without distorting the frequency content of the image. Lower left: reprojected submap, grid is now square around the center of the submap. Lower right: reprojected and repixelized submap. Note that the cluster now seems more elongated in the vertical axis.

it uses exactly the same pixel-space mask, no matter where the galaxy in question is located. Also, to keep the analysis simple, no grid reprojection was used and a cylindrical equal area pixel grid was used (which was the projection that ACTPol was using at the time).

The newer ACT maps have changed the sky projection grid to a Plate Carrée grid (with circles in azimuth that change in size as $1/\cos\theta$). We have explored interpolation and reprojection schemes that make the analysis independent of the grid choice by first decreasing the size of the pixel element via a zero-padding

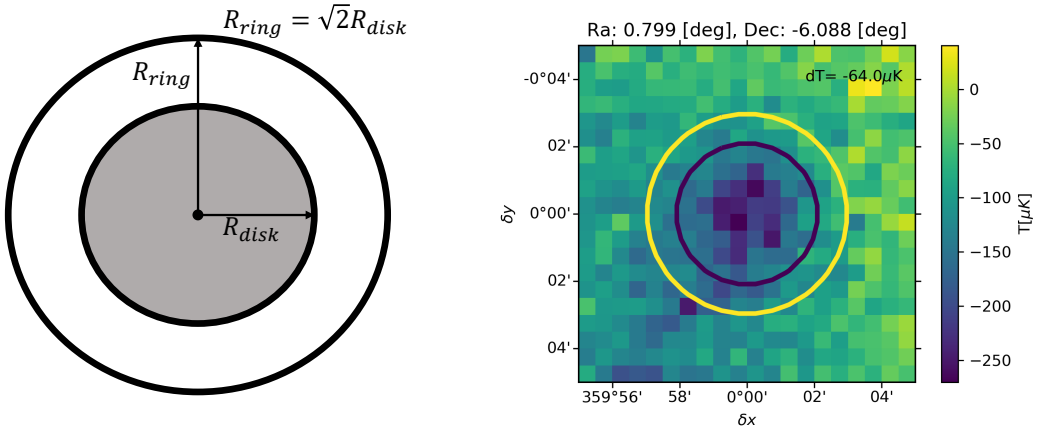

Figure 5.12: Aperture photometry. Two concentric circles are drawn in angular space around one galaxy position. The mean brightness of the disk and ring are then computed.

interpolation in the Fourier domain (also called a sinc interpolation [40]) around the galaxy in question and then reprojecting to a square coordinate system centered in the galaxy position. Figure 5.11 shows one example of this process. The trade-off (compared to [14]) is that doing this slows down the analysis. We deal with this increased complexity by adding a preprocessing step that can be split across multiple machines in the cluster. This step takes $\sim$ 1 hour for the whole catalog (600,000 galaxies) and needs to be done only once for a choice of interpolation, reprojection and aperture photometry size. We can also export the submaps, though this is even slower (as this process is I/O bound [61]) and is done as an optional step. The kSZ analysis does not need actual submaps, only the integrated brightness of the disk and ring in question.

To compute the aperture photometry we draw a circle (of radius R_{disk}) around the source position in sky coordinates after the interpolation and reprojection steps are done. We compute the mean brightness (T_{disk}) of the interpolated (now with a much smaller pixel size) grid. Then we draw a ring around the selected disk, the ring corresponds to the area where $R_{disk} < r < R_{ring}$ and

compute the mean map brightness (T_{ring}) inside the annulus. The radius of the ring R_{ring} is chosen so it contains the same area as the disk, this happens when $R_{ring} = \sqrt{2}R_{disk}$. Figure 5.12 shows an illustration and an example from the map.

5.6.1 The algorithm

The following steps detail how to extract the kSZ signal from the map[1]:

1. Extract submaps on the original pixelization.
2. Zero padding interpolation.
3. Repixelize to compensate for grid distortions far from the equator.
4. Draw an aperture and extract the mean temperature of the inner disk and outer disk (aperture photometry).
5. Compute the redshift smoothed function $\mathcal{T}(z)$.
6. Compute the pairwise estimator.

I have split the computation in two steps that can be run on a cluster. Steps 1 to 4 use pixell [48], the Simons Observatory library for map analysis, which has part of the methods parallelized (like FFTs). I split the 500,000 galaxy catalog in $\sim$ 10 smaller 2-core jobs and run these in the CLASSE cluster which has no trouble assigning 20 cores for this job. Splitting the data into smaller jobs reaches diminishing returns as the tasks become network bound (too many jobs trying to access the same data at once). This preprocessing step takes about 1 hour and roughly the time it takes grows linearly with the number of galaxies in the catalog (for a fixed number of workers).

[1]The reader can find the source code in https://github.com/patogallardo/iskay

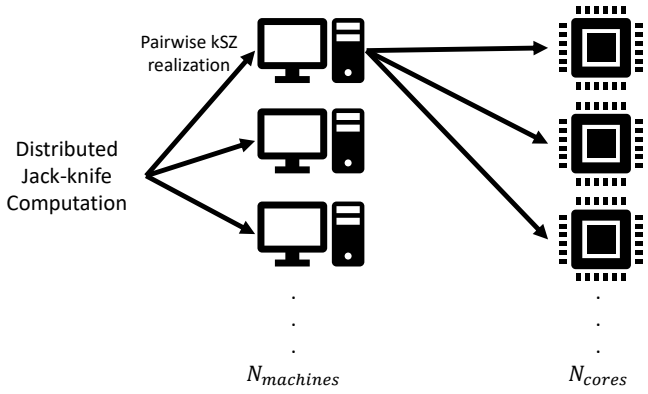

Figure 5.13: Diagram showing the distributed jack knife errorbar computation. One computer is capable of computing one kSZ curve on all its cores. Each of the jackknife replicants are computed in different machines at the same time.

The second part of this algorithm is the pairwise kSZ estimator. Here the complexity of the algorithm is much higher as the number of calculations grows as N^2 so more care was taken to ensure fast computation. There is a variety of approaches we have considered, but we converged in the following: we use a rather new Just In Time (JIT) compiler for Python called Numba [42], which generates low level machine code from pure Python code. The use of Numba gives speedups of as much as 100x (which is already competitive to pure C code) compared to native Python, this gives the right balance of quick development turnarounds and quick run times. We compute the smoothed out $\mathcal{T}(z)$ as a multi-threaded vectorized computation in Numba. The pairwise estimator is then computed as multiple processes (note the difference between a thread and and a process) on a single machine.

This solution has the benefit of being able to compute one entire kSZ curve in a single machine (which is desirable as no data has to be sent through the network once the computation started). We leverage this property for the cal-

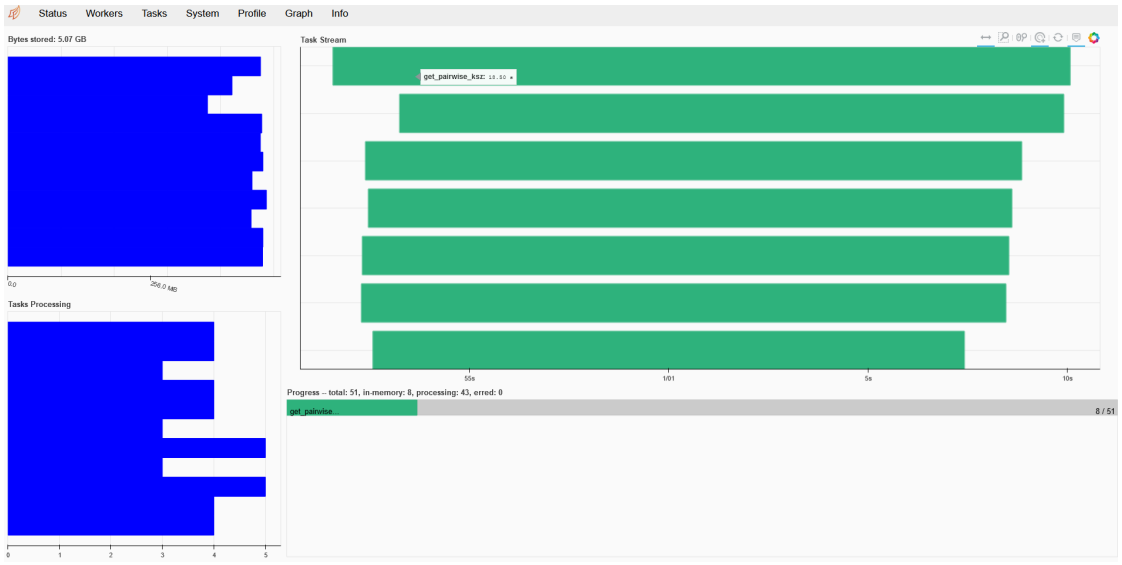

Figure 5.14: One instance of the Dask [55] dashboard coordinating the execution of the kSZ estimator throughout the network. Each green bar represents the time one kSZ curve took to compute in one computer. On the left the memory usage and the job queue is shown.

culation of the error bar (standard error) in which we use Dask [55] to deploy this program in multiple machines (around 10) throughout the CLASSE Cluster using 20 cores in each machine. Figure 5.14 shows one instance of Dask coordinating the execution of the jackknife errorbar.

The computation time is a combination of how many computers we are using to get the errorbars (which require around 50 kSZ curves), how many cores we are using in each machine to compute each kSZ curve and how many galaxies there are in the catalog. Ignoring all the overhead, one simple expression for the computation time scales as

$$t_{\rm computation} \propto \frac{2N^2_{\rm galaxies}}{n_{\rm cores} n_{\rm machines}}. \tag{5.31}$$

Here I have added a factor of two since we are doing two calculations with

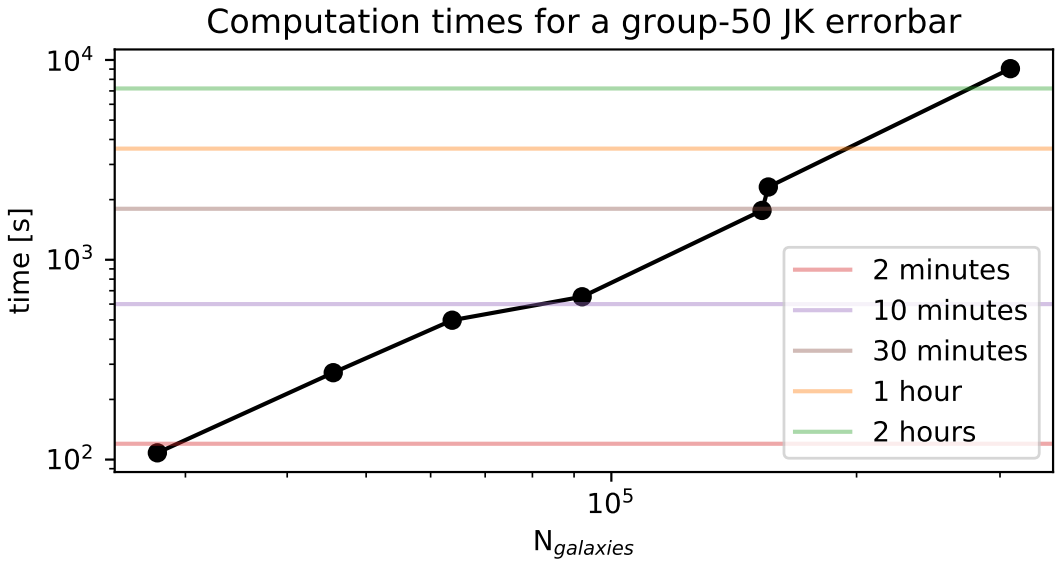

Figure 5.15: Group-50 Jackknife run times for a set of computations (kSZ curve with errorbars) with varying sample length. Notice that the computation time grows as N^2. Doubling the number of galaxies quadruples the computation time. In this run, I have requested 10 workers with 15 cores each (which is common for the CLASSE cluster). The code in FDB 2016 [14] needed $\sim$ 50 hours of computation time for 60,000 galaxies, we have cut this to less than 10 minutes (300×).

complexity $O(N^2)$, the first is the computation of $\mathcal{T}(z)$ and the second is the computation of the pairwise estimator. We can thus cut this time by a factor of two if we sparsely evaluate the function $\mathcal{T}(z)$ and interpolate it. I leave this as a future study, but preliminary tests show that this can be done without impacting the accuracy of the estimator.

5.7 Verifying D56 clusters

As a test, and to make sure we are reading the maps correctly, I downloaded the D56 cluster positions presented in [38]. In that work, a detection of 182 clusters was done through matched filtering, here I average submaps centered in their reported cluster coordinates as a check that the pipeline is working as expected.

Figure 5.16 shows the 182 clusters from [38]. Here I show the result of using the same pipeline that was used in my kSZ extraction. In this example submaps are cut around the cluster positions, the submaps are interpolated with a zero-padding scheme (as described in section 5.6.1) decreasing the size of the pixel by a factor of 20, re-projected to compensate for changes in the grid projection, subsampled to a pixel size of 0.5 arcmin and then averaged the sub maps. Figure 5.17 shows the result of such average.

With the cluster positions and redshifts of these confirmed clusters we can also show how galaxies at the redshift of the cluster track the center position. If we extract the sky coordinates in right ascension and declination from the SDSS catalog within 5 arcminutes of each cluster, we can generate the 2D histogram shown in Figure 5.18.

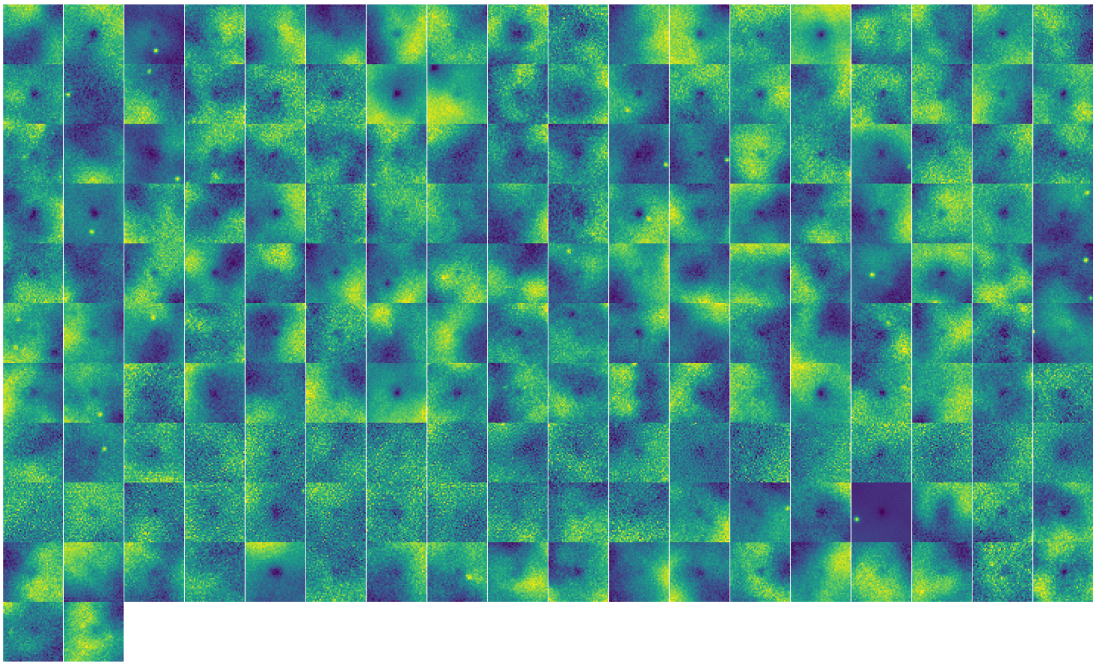

Figure 5.16: D56 region clusters extracted from the ACT co-added map.

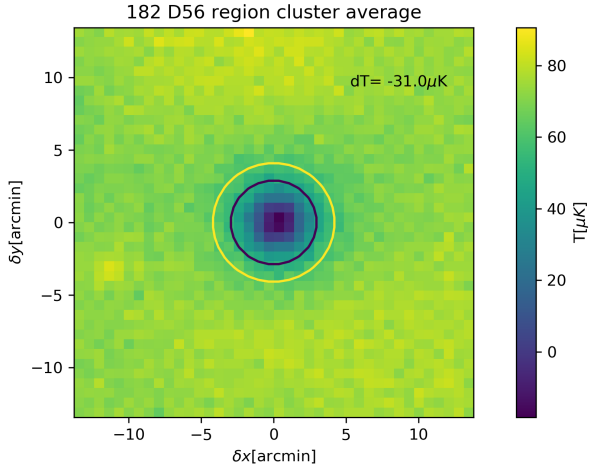

Figure 5.17: D56 region SZ cluster average. Concentric circles show the 2.1 and 2.97 arcminute radii used in the aperture photometry.

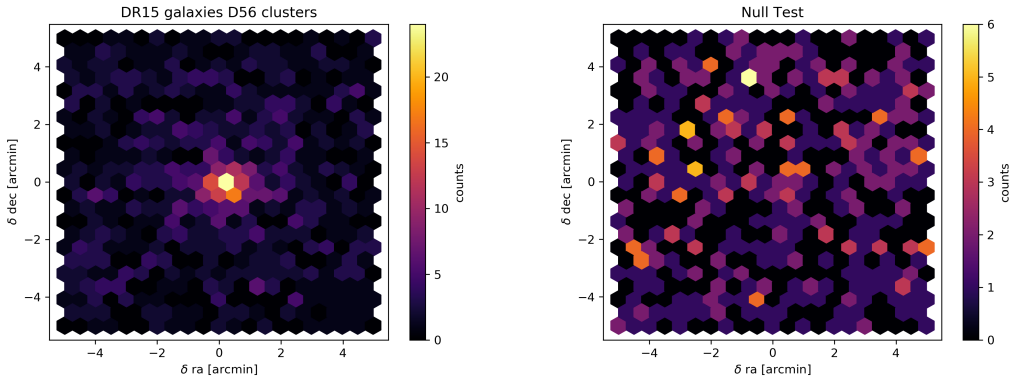

Figure 5.18: (left) 2D Histogram showing the frequency of galaxy positions near the center of their respective cluster. Galaxies within 5 arcminutes from the central cluster are shown. (right) Null test, where we add 5 degrees to the position of each cluster in the list and no clustering is observed.

5.8 Preliminary Results

I will summarize here some of the results we can get with the tools we have built. The work presented here has received input from many people in the collaboration, in particular EV and VC have been crucial. For these results an aperture of 2.1 arcminutes was used for the aperture photometry. We might change this in the future as we are converging on what value is appropriate.

On this section I show some tSZ results I include as a sanity check. EV has been working on this part of the project with greater detail and we will be comparing these results for consistency.

5.8.1 tSZ

The thermal SZ is a natural sub-product of this pipeline. We compute the decrement tSZ for the whole catalog as it is needed for the kSZ estimator, see equation 5.19. On figure 5.19 (top) the distribution of the *ring* vs *disk* temperatures is shown. The linear trend indicates that the disk temperature tracks the background and the actual decrement is small in value. Here notice that the histogram for T_{ring} is slightly offset from zero. In future work we should understand why this happens. Figure 5.19 (bottom) shows the distribution of dT as a function of luminosity.

We can also explore the distribution of the temperatures of the disk and ring on sky coordinates to see if there are any systematic trends in the data. Figure 5.20 (top) shows the distribution of T_{ring}, notice the resemblance of this plot to the CMB anisotropies. Figure 5.20 (bottom) shows the distribution of dT in sky coordinates. No major trend is seen here other than the noisier regions of the map taking extreme values. This behaviour is suppressed when applying a cut based on the noise of the map to the original catalog.

It is possible to compute the statistics of all the galaxies in the catalog that survive the $45\,\mu$K noise cut and get an estimate of the overall SZ decrement without doing a luminosity cut. Figure 5.21 shows this histogram. Here it can be noted that the mean temperature difference is $dT = -0.12 \pm 0.03\,\mu$K. This rules out a zero mean to 4 σ.

This analysis can be brought a step further and split the estimate of the mean per luminosity cut. Figure 5.22 shows violin plots (one semi-width of each violin represents bootstrapped probability density of the mean) and errorbars of the 5

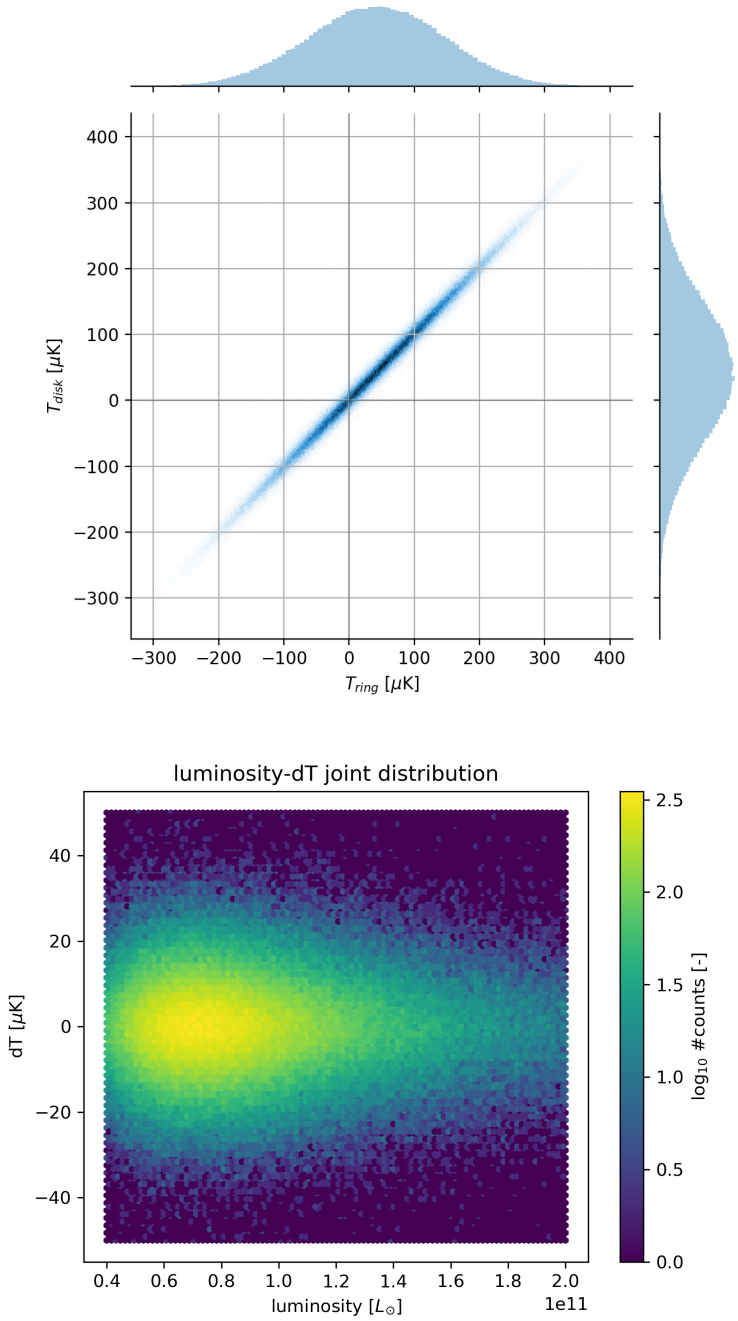

Figure 5.19: (top) Joint distribution of the aperture photometry ring and disk contributions. The tSZ difference is obtained from doing $dT = T_{disk} - T_{ring}$. On the top and right separate histograms are shown. Central plot is a two dimensional histogram of the joint distribution of these two variables. (bottom) Joint distribution of the aperture photometry (dT) as a function of luminosity.

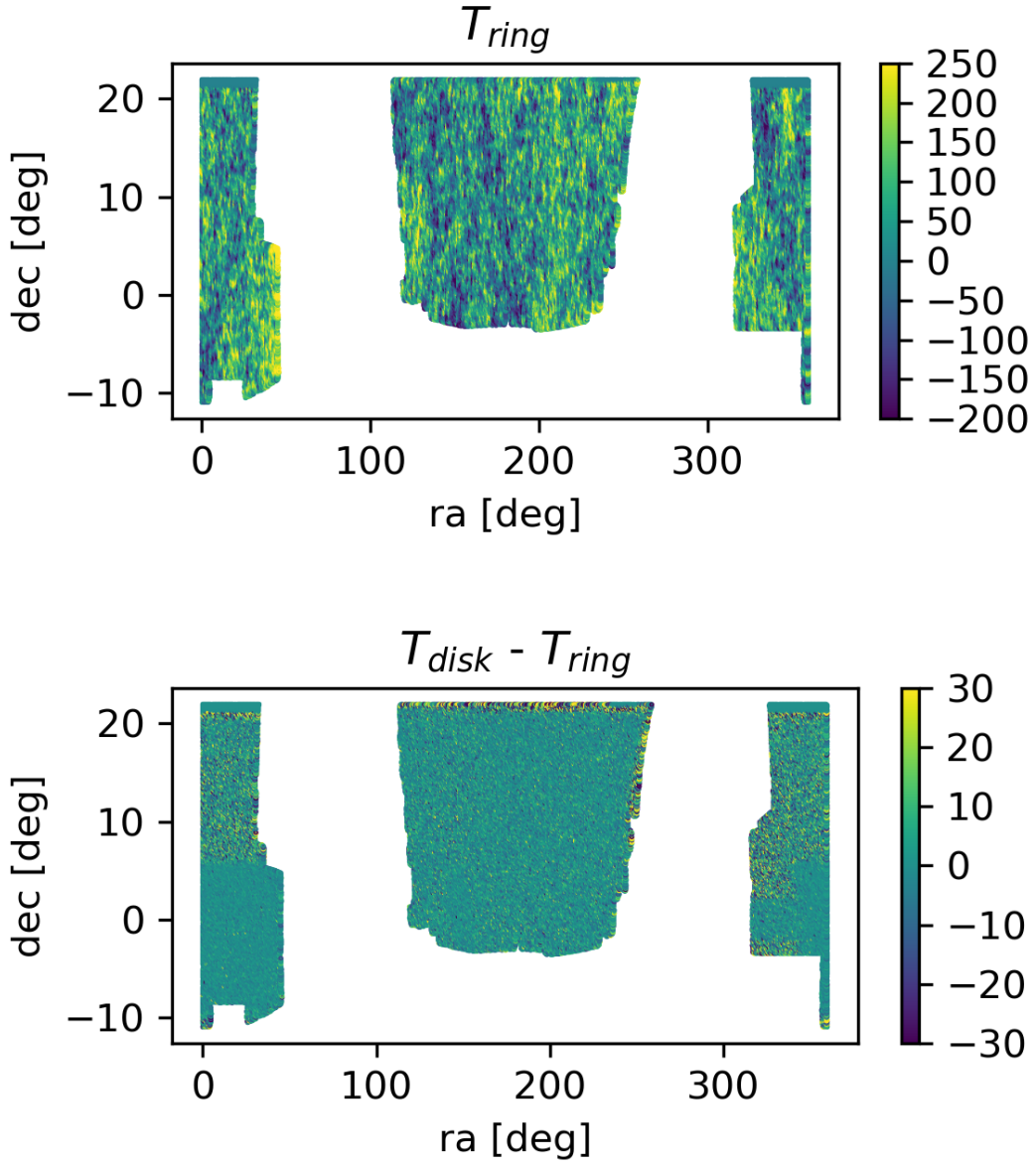

Figure 5.20: Sky distribution of the ring temperature (top) and the SZ decrement (bottom). Note the resemblance of the T_{ring} distribution to the CMB anisotropies. The decrement distribution shows no major trend other than the noisier regions of the map.

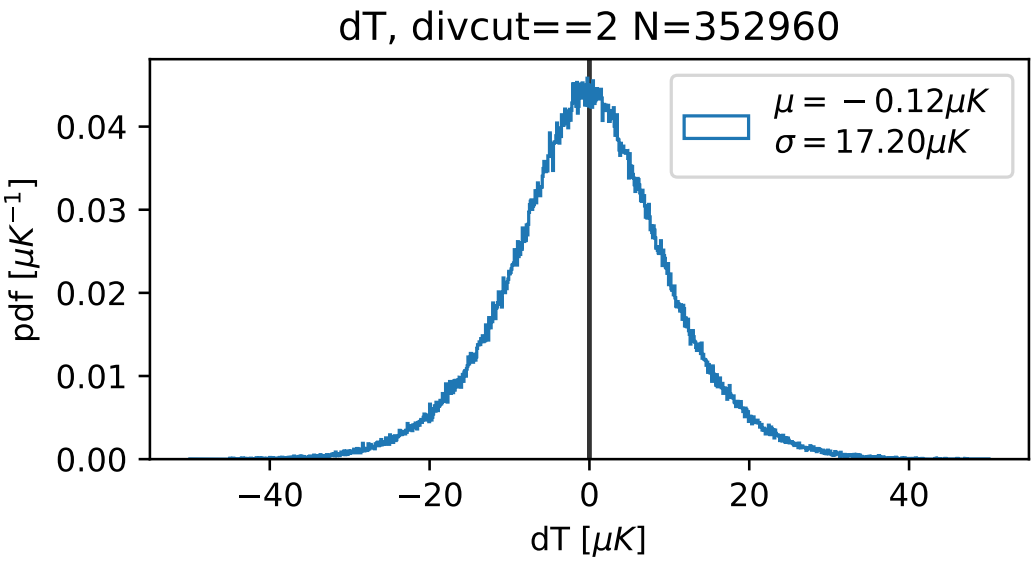

Figure 5.21: Aperture photometry histogram. $dT = T_{disk} - T_{ring}$. A cut based on the noise of the map was applied, using $45\,\mu$K as a tolerable noise limit. The mean of the distribution is -0.12 ± 0.03 which rules out a zero mean to 4 sigma.

luminosity bins we have considered in this study. Here the only cut that was applied to the catalog was the noise above $\sigma_{noisemap} = 45\,\mu$K. Note that this discards almost a half of the catalog. A variance weighted average would be more suitable and is left as a future study.

As seen in Figure 5.22 the tSZ dependence on luminosity is nearly flat for the first three luminosity bins ($6 \times 10^{10} L_\odot < lum < 12.8 \times 10^{10} L_\odot$). For lum> $12.8 \times 10^{10} L_\odot$ the tSZ decrement starts to increase with a slope $\sim 0.1\mu$ K$/10^{10} L_\odot$.

One aspect that can be studied here are the asymmetric tails of the distributions that can be seen in the violins in Figure 5.22, do these get suppressed if we do an inverse variance weighted bootstrap? Figure 5.23 shows that this is in fact the case.

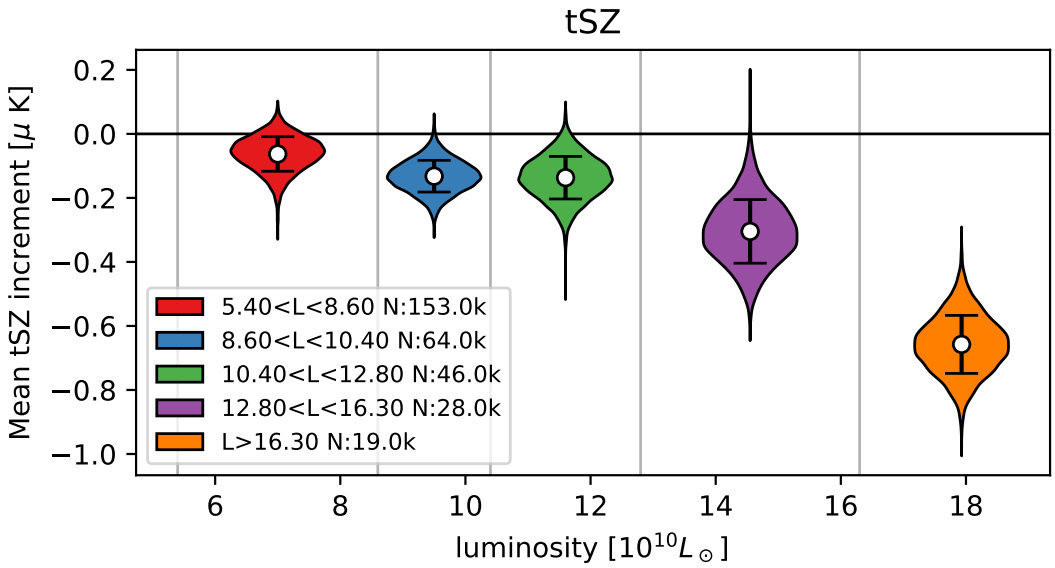

Figure 5.22: Thermal SZ decrement for the 5 luminosity bins used in this study.

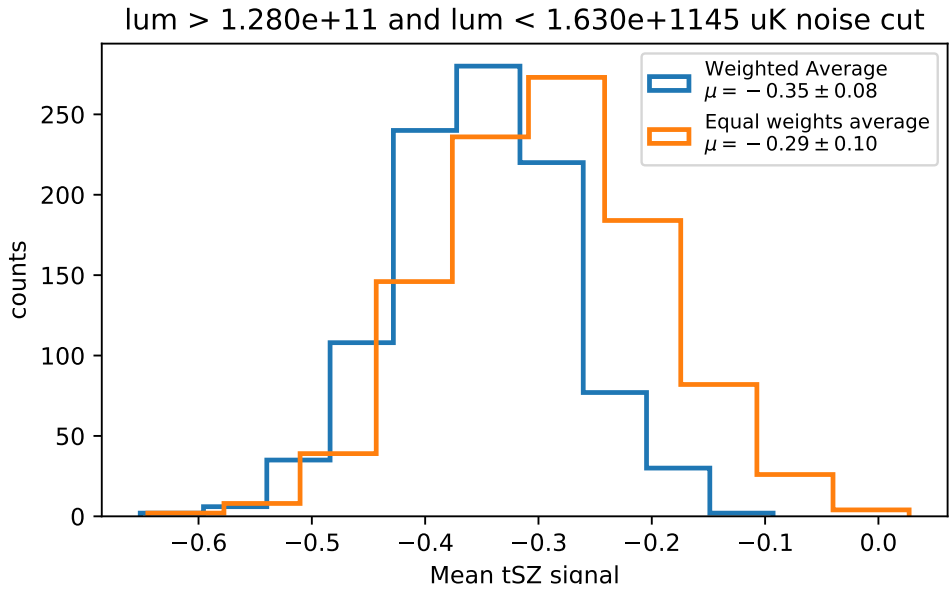

Figure 5.23: Thermal SZ effect for the bin between 12 and 16 $\times 10^{10} L_\odot$ for a simple average with equal weights and an inverse variance average.

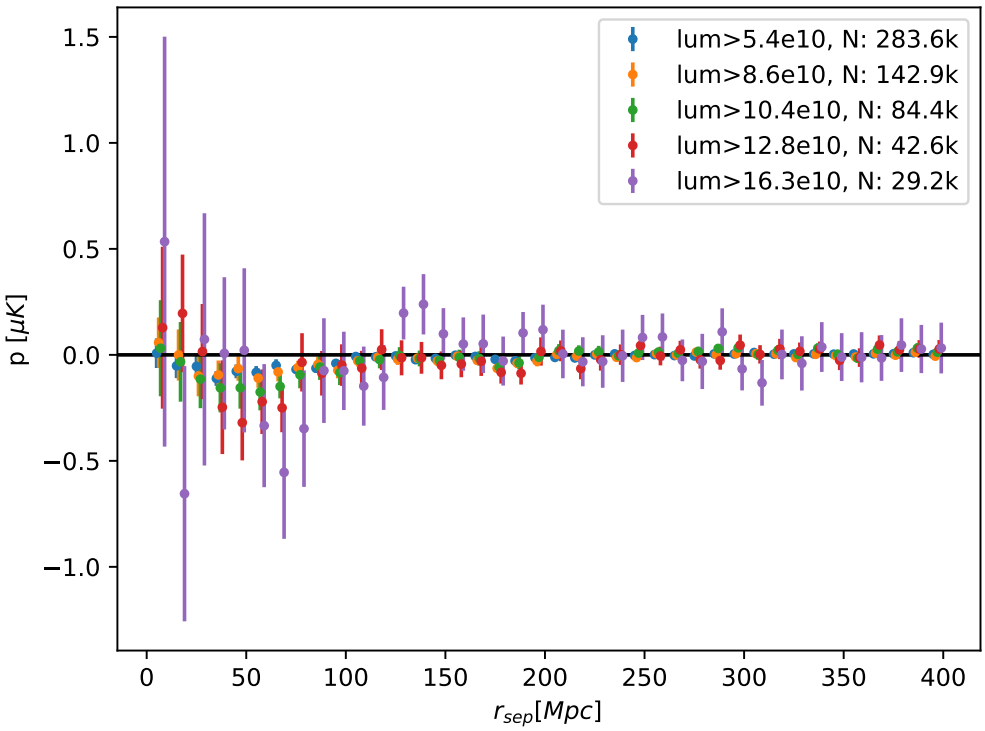

Figure 5.24: Mean pairwise momentum curves. Note that the amplitude around the 50 Mpc peak decreases with decreasing luminosity cut. However decreasing the luminosity cut also decreases the uncertainty in the estimator.

5.8.2 Pairwise kSZ

We obtain momentum curves as a function of galaxy separation for our catalog. Figure 5.24 shows 5 curves in increasing luminosity cut. The peak decrement occurs at around 50 Mpc of separation and the amplitude is about 0.5 μK. The amplitude of the decrement decreases with decreasing luminosity cut as it was noted in [14]. However decreasing the luminosity cut also increases the number of objects that are included in the estimator making the estimation less noisy. Figure 5.25 shows the correlation matrix for $L > 12.8 \times 10^{10} L_{\odot}$.

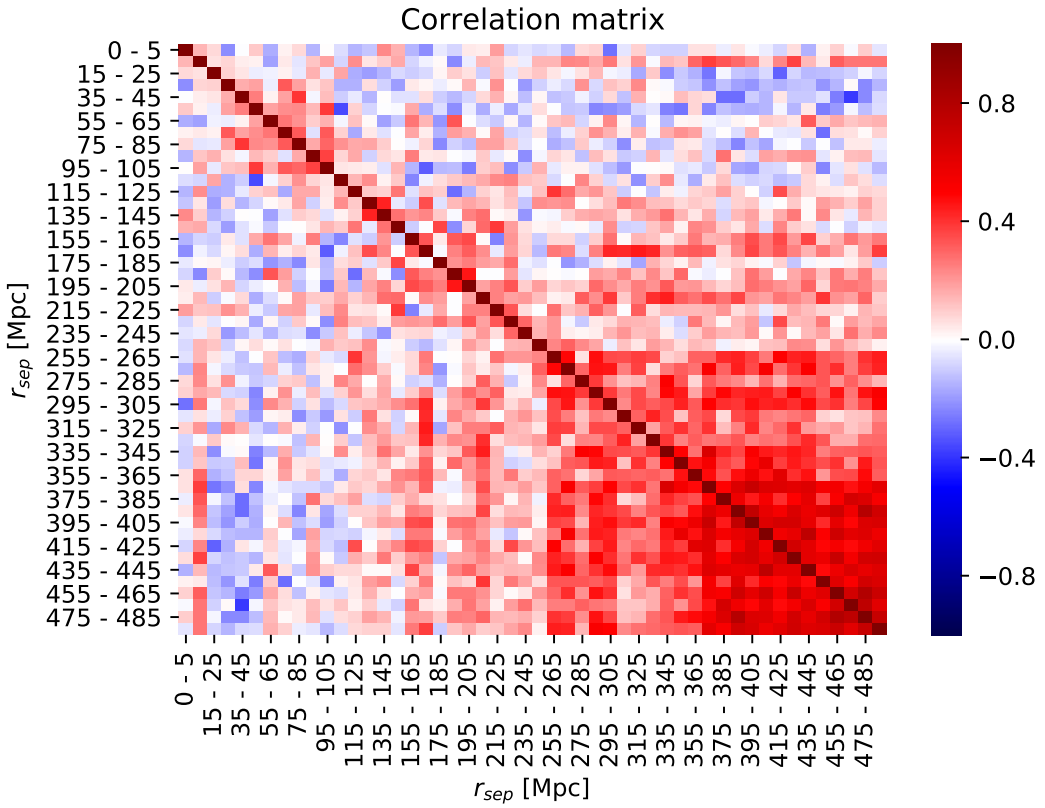

Figure 5.25: Correlation matrix for the pairwise momentum estimator shown in Figure 5.24. Correlations for $L > 12.8 \times 10^{10} L_{\odot}$ is shown.

Variance weights

Using the same $45\,\mu$K noise cut and same luminosity cuts as in the previous section, we can compute the variance weighted curves. Figure 5.9 shows the resulting curves. The curves change slightly but the general trend remains. Note as well that the point around 70 Mpc for the second highest bin now tracks the point for the highest bin.

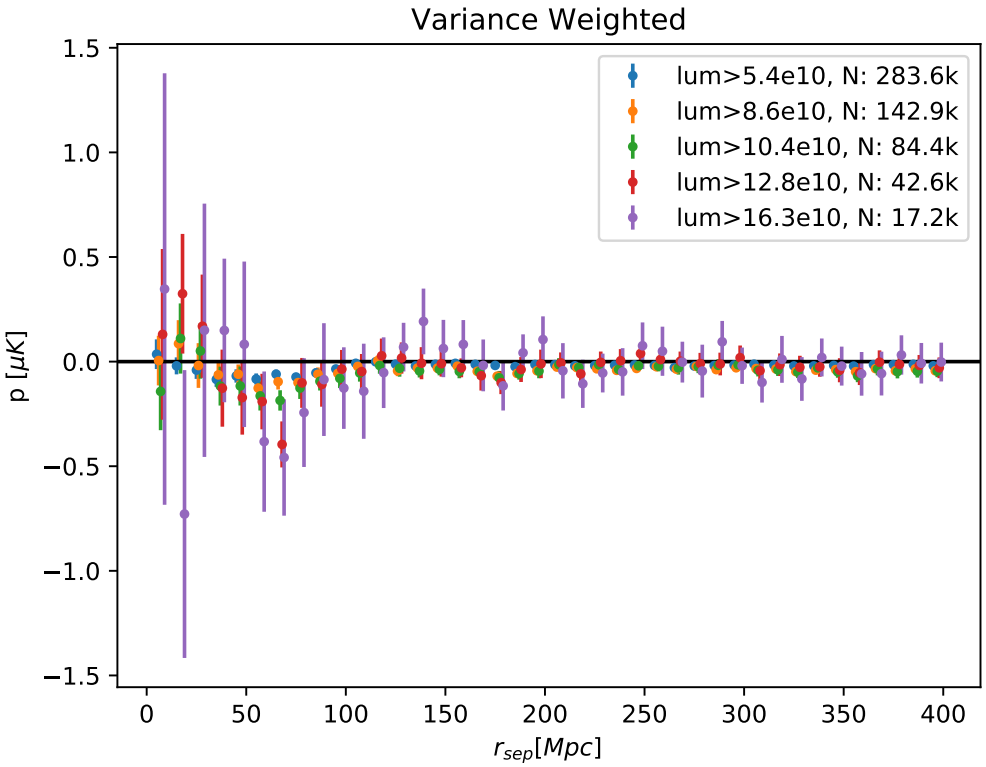

Figure 5.26: Variance weighted mean pairwise momentum curves. Points near 70 Mpc for the two highest bins in luminosity are now slightly larger in magnitude compared to the equal weights case.

CHAPTER 6

SIDELOBES

6.1 Introduction

On a CMB instrument sidelobes and stray light have an impact on the overall sensitivity performance. They can generate spurious signals if not controlled. In this chapter we define stray light and sidelobes, we explore the relation between stray light and sidelobes in the the Atacama Cosmology Telescope by building a model that describes the sidelobe pattern starting from an experimentally measured curve of the camera stray light angular distribution and show how this model is being used to inform the design of the Simons Observatory. We discuss the limitations of this approach and sketch what future work addresses these issues.

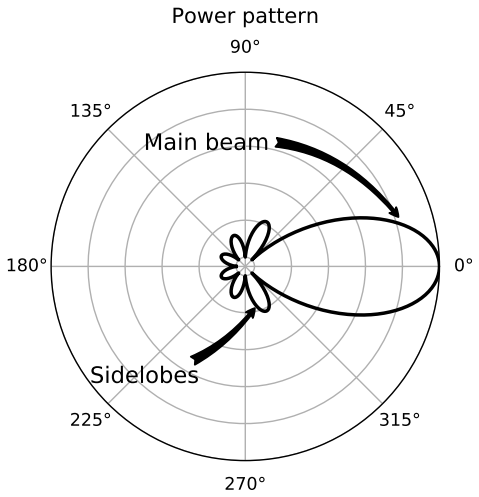

Figure 6.1: A cartoon representation of $P(\theta)$. The angular response consists of a main beam and sidelobes that extend far from it.

6.2 Definitions

Stray light: In optics, light paths that do not follow the primary path (mirror1, mirror2, lens1, lens2, lens3, focal plane) are said to be stray light. In practice, mechanisms that generate stray light can be: scattering, reflections or diffraction. To mitigate stray light, it is common practice to use baffles (reflective or absorbing concentric rings) and stops. Anti-reflection coatings also help mitigating stray light because they minimize the generation of reflections inside the optical path.

Sidelobes: The angular response of an optical system (given by its point spread function $P(\theta, \phi)$) consists of a *main beam* and *sidelobes*. The main beam is the region to which the system is the most sensitive to light. Sidelobes are directions from where, though not in the main beam, still some light can be detected at the focal plane usually attenuated (by several 10s of dB) below the main beam intensity, see Figure 6.1.

Sidelobes can be classified in near and far, depending on their angular position relative to the main beam.

Near sidelobes are sidelobes that are close (from a few times $\frac{\lambda}{D}$ to $\sim$ a field of view) to the main beam. They can be generated by diffraction (ringing in the Airy function), ghosting (reflections between optical components), stray reflections (reflections on the baffling structures) and scattering in optical components to name a few. Their intensity is $O(10\times)$ lower than the main beam or weaker.

Far sidelobes occur from 1 FoV to 180 degrees from the main beam. They are

typically attenuated more than 20 dB, because of this they are hard to measure and require detailed modeling or experiments to be identified and understood. Sources of far sidelobes are: reflections/diffraction over the physical structure of the telescope and scattering over optical components.

Antenna Gain The antenna gain is the power pattern normalized such that the integral over the sphere equals to 4π

$$\int_{4\pi} G(\theta, \phi) = 4\pi. \tag{6.1}$$

Here θ and ϕ are the usual spherical coordinates around the optical system.

Pickup temperature Given an extended source in the sky, with brightness temperature $T(\theta, \phi)$, the pickup at the focal plane can be computed according to

$$T_{pickup} = \frac{1}{4\pi} \int_{4\pi} G(\theta, \phi) T(\theta, \phi) d\Omega. \tag{6.2}$$

If the source is extended and the sidelobe pattern is slowly varying and it subtends a solid angle $\Delta\Omega_{source}$, the pickup will be given by

$$T_{pickup} \approx \frac{1}{4\pi} G(\theta_s, \phi_s) T_{source} \Delta\Omega_{source}. \tag{6.3}$$

Where θ_s and ϕ_s are the angles at which the gain is being evaluated at to approximate the sidelobe level.

6.2.1 Physical origin

The physical mechanism that generates a sidelobe can correspond in general to a combination of simpler mechanisms, some of which are listed below:

Diffraction Sharp edge diffraction can cause sidelobes. In a perfect circular aperture case, diffraction around an aperture with uniform illumination will cause a sidelobe at the second maximum of the function $2J_1(x)/x$ which is 17.83dB below the peak.

Ghosting Reflections inside a refractive camera can cause the phenomenon known as ghosting. Light coming through the camera gets reflected off an optical component and this reflection is re-imaged, creating a false image at the focal plane. Optical elements that can contribute to ghosting are: a reflective focal plane composed of metalized feedhorns/reflective lenslets, partially reflective lenses or filters, and a partially blackened optics tube interior.

Stray Reflections Off-axis light can be reflected by surfaces that are not perfectly black. in the baffling structure of a refractive system, creating a sidelobe. This sidelobe, in the case of a large aperture telescope can interact with the telescope support structure generating a complex pattern.

Scattering in optical components Scattering refers to any re-emission of light passing through a material. The angular dependence of this re-emission depends on the details of the properties of the material but in general is not necessarily specular.

Panel Gap Diffraction Primary and secondary mirrors are commonly built from individual panels. If the wavelength of operation is of the order of the physical size of the panel gaps, light will diffract forming a complicated diffraction pattern that creates sidelobes. These sidelobes can extend over several degrees and can be polarized [24].

Ruze Scattering Gaussian surface errors on reflector elements can cause distortions to the main beam. The Ruze equation relates the loss in antenna gain

related to the RMS surface error ϵ according to

$$G(\epsilon) = G_0 e^{-(4\pi\epsilon/\lambda)^2} \tag{6.4}$$

where G_0 is the antenna gain in the absence of surface errors and λ is the wavelength of operation.

6.3 Modeling techniques

There are two groups of modeling techniques for large reflective systems coming from different regimes in the electromagnetic spectrum and differing in computational complexity. Ray tracing is primarily used in the optical wavelength regime, while the electromagnetic methods have been developed for applications in the radio regime.

Ray tracing For a high frequency system at which the wavelength is small compared to the feature sizes of the system, a ray trace can be used. In this case, light follows a straight line and its path depends on the angles at which optical elements are configured in the system. Refractive optical elements can be modeled by computing the refraction angles of the rays. These computations can include many physical parameters like polarization and interference which makes them useful to model even wave-like characteristics of light, though the electric field and magnetic field are being modeled as plane waves throughout the system. A variety of commercial tools exist to carry out analysis in this regime[1], scattering can be modeled and even diffraction under certain assumptions. These tools allow the user to launch a large number of rays (10^6) and thus

[1]See for example https://www.zemax.com/

probe out regions of the system that have a very weak response compared to the main beam. This method is fast (can be run in a desktop computer) and enables wide range of models for the individual responses of the elements in the system.

Electromagnetic These methods correspond to a broad range of computational approximations to Maxwell equations that allow computing the radiation pattern of a set of reflectors in different scenarios. These tools were developed for communication systems in radio engineering and (depending on the method used) can be used to compute the electromagnetic response of large scatterers (thousands of wavelengths in size). With the development of fast multicore CPUs they can be used to compute the response of a 6m diameter mirror at hundreds of GHz (that is, thousands of wavelengths in size) on one server sized computer (with more than 30 cores). The most common technique of this group is called Physical Optics (PO) which is used to compute sequential diffraction on reflectors. PO tools can also be used to compute interactions among pairs of refractive scatterers. The biggest limitation of PO tools is that they are hard to set up in multiple reflection configurations and scattering is challenging to describe. Another method commonly used for small structures is the Method of Moments that can compute infinite reflections in a closed system inside a volume. This method is more computationally intensive than PO and can be used for small regions of the optical chain (for example, the Simons Observatory collaboration is exploring using a MoM calculation to compute the response of the instrument camera) but it is unfeasible for the whole optical system. These methods are implemented in the software package GRASP[2].

[2]https://www.ticra.com/software/grasp/

Hybrid methods For large structures with more than thousands of wavelengths across, even the use of PO can be prohibitive in terms of computational cost. Hybrid approaches exist to compute the response in these cases. One approach called Geometric Theory of Diffraction (GTD) can be used, which computes the response as if it were computing a ray trace. Diffraction is computed by adding a per-ray diffraction scattering model. This approach is less precise than PO and MoM but it is a great tool to consider for a new model of which the designer wants to get an idea of the overall characteristics of the system as it allows rapid prototype-evaluation cycles.

6.4 Spillover in the Atacama Cosmology Telescope

Since the first camera in ACT (MBAC), we have been interested in measuring the camera angular response as it is directly related to the sensitivity and sidelobes of the telescope. In reference [25] the angular response of MBAC was measured (see Figure 6.2). We noted that the far angle response of the camera was larger than expected for a purely diffractive model.

Variations of this work were done again for ACTPol and yet again for Advanced ACTPol. This measurement is hard to do in practice as it is easy to contaminate the experiment with the apparatus built to do the measurement. Finally our best measurement to date was done at the site by Nick Cothard and published in SPIE 2018 [26], see Figure 6.3. In this publication we also used GRASP to show that the expected fall-off from a purely diffractive model is not enough to explain the camera beam pattern at large angles see Figure 6.4.

The measured beam can be translated into a spillover fraction (or percent-

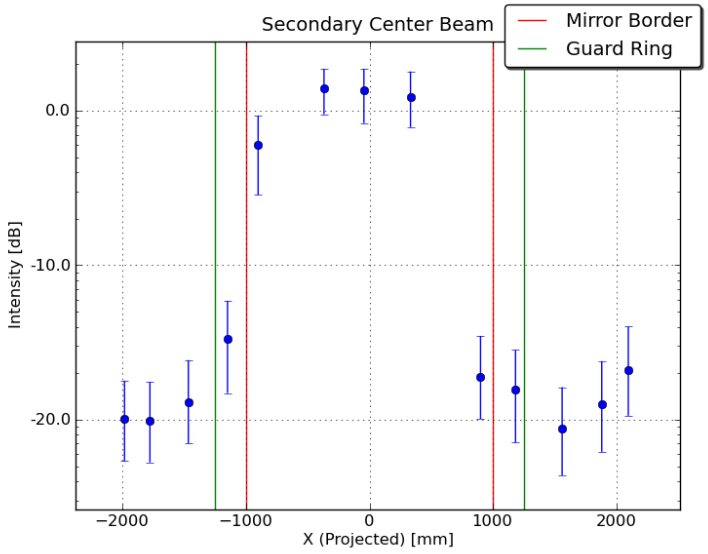

Figure 6.2: MBAC camera spillover measured in 2012.

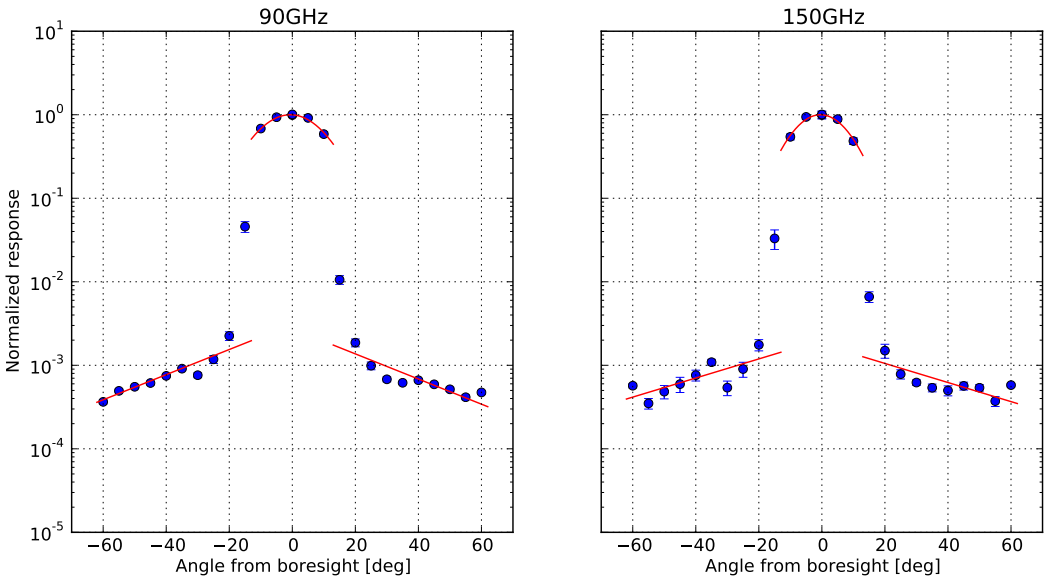

Figure 6.3: Camera beam from Advanced ACTPol, the third camera PA6 is shown. The left figure shows the 90 GHz beam and the right shows the 150 GHz beam. The Gaussian beam given by the feedhorns in the focal plane can be seen at the center. There is an abrupt jump around 15 degrees, and there is a slow exponential fall-off at larger angles.

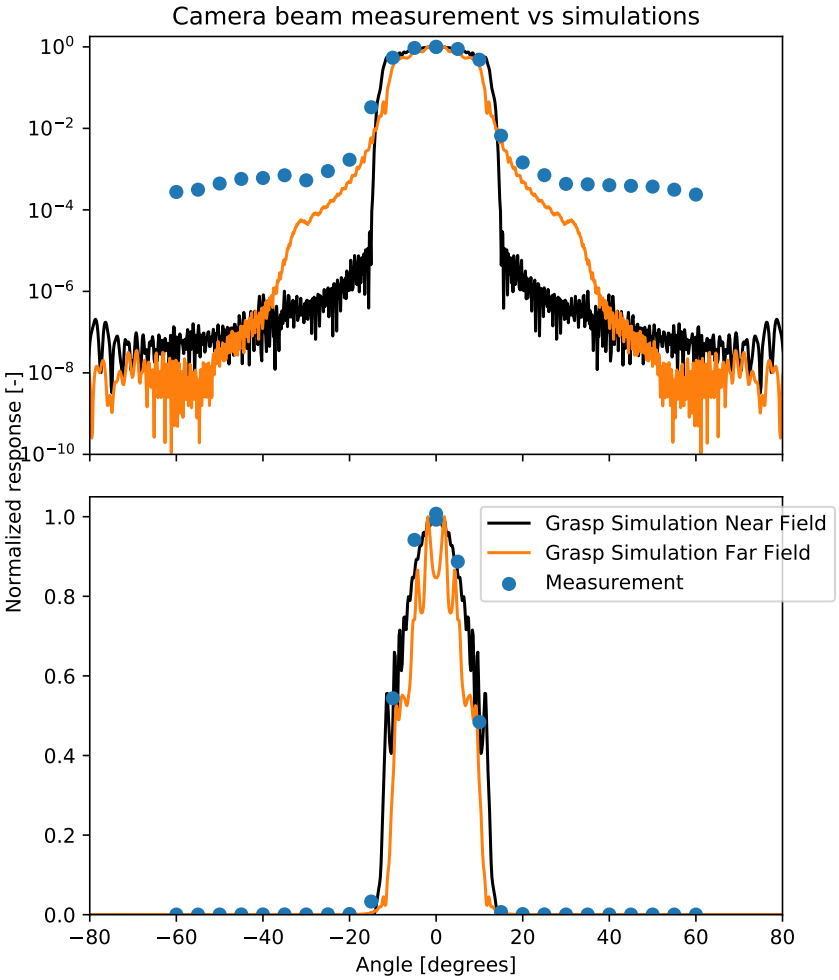

Figure 6.4: Camera beam measured in [26]. Black and orange lines show a physical optics calculation beam evaluated on the near and far field respectively. Dots correspond to the measurement. Note that a diffractive model does not explain the measured far angle response.

age), which is a metric commonly used to describe the spillover performance. The spillover fraction is given by

$$\eta_{sp} = \frac{\int_{\Omega_{sp}} P(\Omega) d\Omega}{\int_{4\pi} P(\Omega) d\Omega}. \tag{6.5}$$

In the case of ACT, using the data measured in [26], we showed that the spillover fraction for the case of Advanced ACT is 3% and it does not depend strongly on frequency, while comparing the 90 GHz with the 150 GHz bands.

6.5 Sidelobes from spillover

The spillover characteristics of the instrument can be used to explain another optical property of the instrument, its sidelobes. The far sidelobes of the telescope depend on how the camera beam is projected onto the telescope structure and reflected to the sky.

We built a hybrid ray trace model. In this model we simulate a camera beam using its measured intensity and traced rays from the telescope focal plane in the time reverse direction. This model has the benefit of being purely phenomenological, it does not require a deep understanding of the physical origin of the spillover mechanism and it can also be used to inform what the physical origin might be if a detailed model of the camera exists. The ray trace used a solid model (see 6.5) that was built by Roberto Puddu (more detail in [26]). This 3D model was built using pictures taken at the site and then using a photogrammetry software to reconstruct the three dimensional positions of the constituent panels of the telescope.

Our optical model keeps track of the intensity per unit of solid angle by

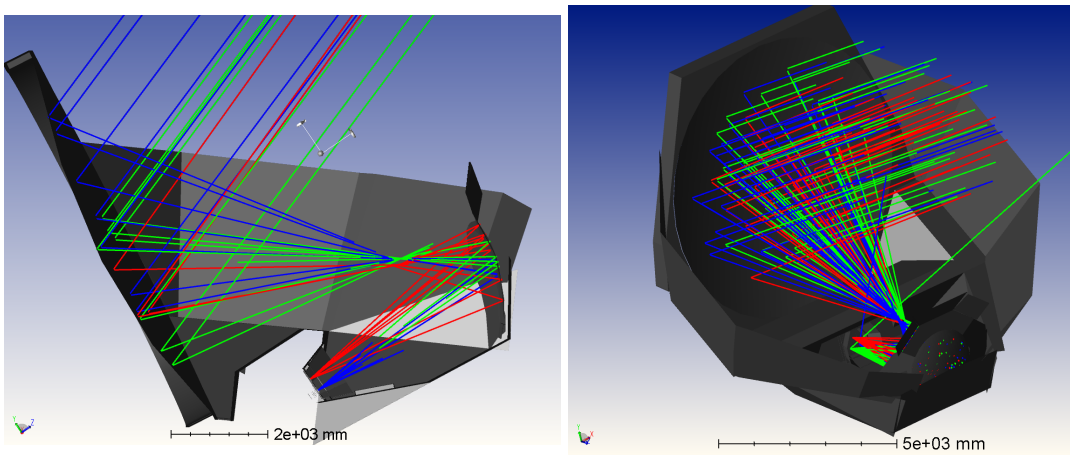

Figure 6.5: 3D model used in this study. Model was built by RP using images of the telescope and inferring the three-dimensional location of each panel with a photogrammetry software.

launching a large number of rays from the telescope focal plane, propagating these rays on the telescope structure and then counting the number of rays that hit a hypothetical spherical detector that surrounds the telescope at a large distance from it. We implemented this model in the optical design software Zemax in the Non-Sequential mode, that allows multiple reflections between optical elements in arbitrary paths (as opposed to the sequential mode, where light has one defined path to follow).

6.5.1 ACT Sidelobes

The output of our model for the ACT geometry and the Advanced ACTPol beam is shown in Figure 6.6. We have explored what panels in the telescope structure are responsible of what sidelobes in the simulation. Figure 6.7 show a few visualizations. Note from top to bottom that the model predicts a sidelobe at 30 degrees that results from reflections on the primary guard ring, diffuse

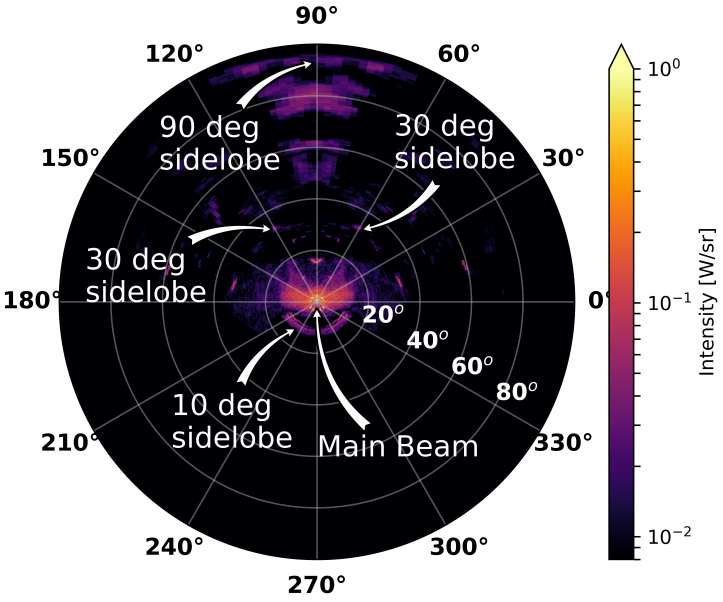

Figure 6.6: Output of the ray trace simulation presented in [26]. Sidelobe at 10 degrees from the main beam shows an amplitude $\approx$ 0.09 W/sr which it is estimated (total injected power is 1W) corresponds to +0.5 dBi. The extended features at 90 degrees have an amplitude $\approx$ 0.04 W/sr which under the same normalization corresponds to -3 dBi

sidelobes near the bore-sight, from the panels next to the secondary and an arc shaped sidelobe at 10 degrees below the bore-sight product of the panel on top of the secondary.

6.5.2 Model validation

Our hybrid model can be used to predict the sidelobe pattern of the telescope. We can use it to compare the predicted angular response of the system to what has been measured while gathering data along the observation seasons.

Qualitatively this model explains the 30 degree sidelobes, and other struc-

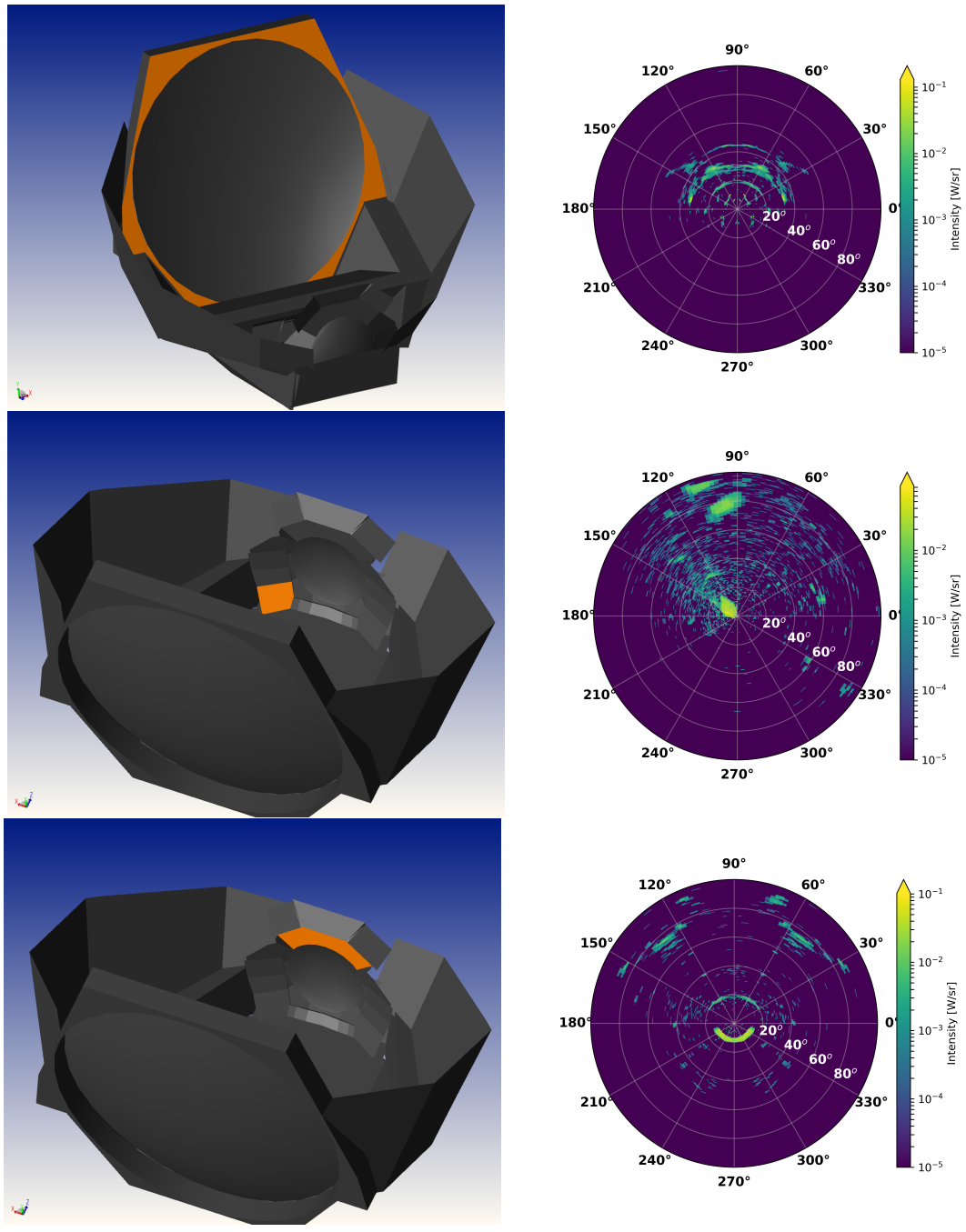

Figure 6.7: Selected panels and their corresponding sky projection

tures at far angles, including a sidelobe at 10 degrees, a group of them a 90 degrees from the boresight. It also explains its symmetries as one considers data from the first, second or third arrays. Figure 6.6 shows the output of our model for PA6. In the following subsections we make this comparison quantitative by looking at values from moon maps and estimating the gain of the main beam.

Sidelobe Gain

We can compare the output of our model to what is observed by making far sidelobe maps. In ACT this is being carried out by the map makers who can produce boresight-centric maps of the moon gathering data from an extended period of time during the season. Here I list the main metrics that are important for this calculation.

Main beam estimate

The main beam peak amplitude can be approximated by the relation

$$G_{max} = \eta_{geo} 4\pi \frac{A_{geo}}{\lambda^2}. \tag{6.6}$$

Where η_{geo} is the geometric efficiency and A_{geo} is the aperture efficiency. For ACT this formula evaluates to

$$G_{max}(150\,\mathrm{GHz}) \approx 77.3\,\mathrm{dBi} \tag{6.7}$$

and

$$G_{max}(90\,\mathrm{GHz}) \approx 72.9\,\mathrm{dBi}. \tag{6.8}$$

This compares well to what was measured in [60] at 150 GHz.

$$G_{peak} = \frac{4\pi}{\Omega_{mb}} = 6.79 \times 10^7 = 78.3\,\mathrm{dBi}. \tag{6.9}$$

Gain from moon maps

The focal plane amplitude of the moon from the moon maps is still in preliminary stage, but an amplitude of $T_{pickup} \approx 250\,\mu$K has been estimated. Using this number the antenna gain for the moon is

$$G = \frac{T_{pickup}}{T_{moon}} \frac{4\pi}{\Delta\Omega_{moon}} \approx \frac{250 \times 10^{-6}}{250} \frac{4\pi}{6.387 \times 10^{-5}} = -7\text{dBi} \tag{6.10}$$

which gives a sidelobe amplitude of -85.3 dB from the main beam at 150 GHz.

Gain from ray trace simulation

The ray trace simulation is given by Zemax in units of W/sr. If we use a total power for the source to be 1 Watt, then the gain is obtained by multiplying by 4π/sr. Using a sidelobe amplitude of 0.09 W/sr from our sidelobe model (taken from the strongest sidelobe at 10 degrees) then our estimate for the sidelobe amplitude from the model is 0.5dBi while some of the faint sidelobes at 90 degrees show an amplitude of -3 dBi these two numbers put the sidelobe amplitude between -78.8 and -81dB from the main beam putting the prediction from the model in the same order of magnitude to the measurement. Table 6.1 summarizes this result. Here note that the moon map is filtered, as the map making needs to subtract the atmosphere modes, this will discard the large angular structures, removing some of the power from the map, therefore we expect some disagreement between the model presented here and the moon maps. Also it is important to note that the moon map is done considering all the detectors in the array, while our simulation takes into account only one of them.

Sidelobe amplitude (ray trace)	Sidelobe amplitude (moon maps)
-81, -78	-85

Table 6.1: 150 GHz sidelobe amplitude estimates referred to the main beam amplitude in dB. The ray trace simulation was computed using a 3% spillover as measurements suggest. [26].

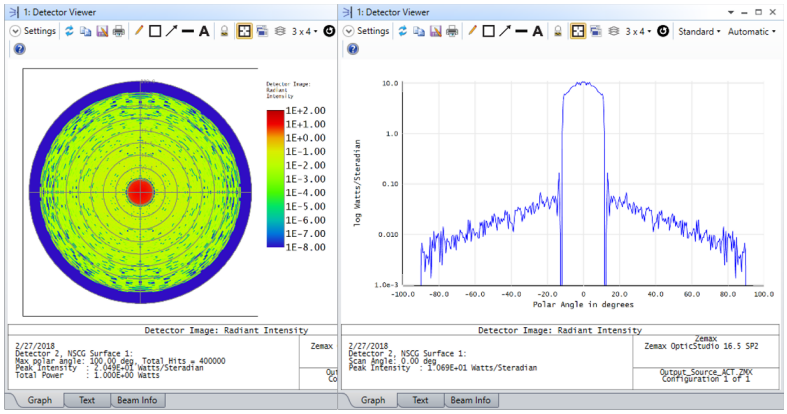

Figure 6.8: Source beam model used to simulate the camera beam.

6.6 Sidelobes predictions for the Simons Observatory

Using the approach presented here, we explored what the sidelobe pattern for the Simons Observatory would look like and informed design decisions like the use of baffles in different parts of the structure. The history of this analysis is being prepared as a SO technical note.

6.6.1 Camera Beam

The camera beam was modeled using the model presented in [26]. This beam was shown to have a nearly Gaussian fall-off near the center (as expected from the focal plane feedhorns) with an exponential fall off outside of the Gaussian part (Figure 6.8 shows a Zemax implementation of this beam). The transition

between the Gaussian model and exponential decay is modeled as a discontinuity as no data has been measured that indicates a better model. This model can be parametrized as follows:

$$\text{CameraBeam}(\theta) = \begin{cases} \exp\left(\frac{-\theta^2}{s_g^2}\right) \text{ for } \theta < 11.3^\circ \\ A_e \exp\left(\frac{-|\theta|}{s_e}\right) \text{ for } \theta > 11.3^\circ, \end{cases} \tag{6.11}$$

where the Gaussian has a width parameter given by s_g truncated at an angle ($\theta = 11.3^\circ$) given by the diameter of the Lyot stop. The exponential fall-off is found phenomenologically and its overall amplitude is given by A_e, while the speed of the fall-off is given by s_e. At 150 GHz our best fit parameters are $s_g = 12.7^\circ$, $s_e = 38^\circ$, $A_e = 1.9 \times 10^{-3}$.

6.6.2 Beam Aiming

The camera beam is launched perpendicular to the camera entrance plane for the fields at the center camera. The side camera beams are launched with a tilt angle that is extracted from the chief ray in the sequential (forward-time) Zemax optical model. For the sake of simplicity we use the fields that are along the x or y axes at the camera entrance, which yield a trivial tilt angle in only one axis.

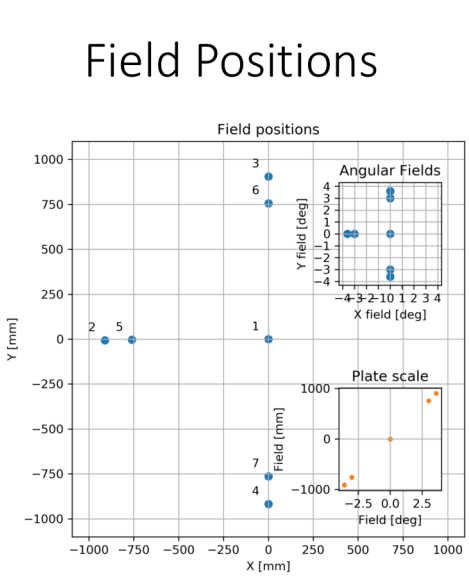

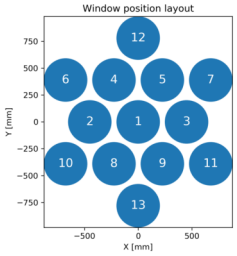

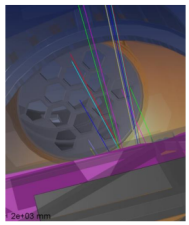

Field	Hx [deg]	Hy [deg]	X[mm]	Y[mm]	anglex [deg]	angley [deg]
1	0.0	0.0	0.00	0.00	0.00	-0.00
2	-3.6	0.0	-911.02	-5.69	2.55	0.02
3	0.0	3.6	0.00	904.92	0.00	-2.51
4	0.0	-3.6	0.00	-916.82	0.00	2.58
5	-3.0	0.0	-759.12	-3.95	2.12	0.02
6	0.0	3.0	0.00	754.91	0.00	-2.10
7	0.0	-3.0	0.00	-763.16	0.00	2.15

Table 2: Output of the code used to determine positions and angles at the secondary focus surface. Hx and Hy are the field positions measured from the boresight, X and Y are the chief ray position at the secondary focus (surface 24 in ID11). Anglex and Angley are the director cosine angles defined as $angle_j = arccos(cos_j)$, where cos_j is the director cosine in the j direction.

Figure 6.9: Field positions and tilt angles used in the sidelobes simulation.

6.6.3 Baffling strategies that have been studied and a brief history of our recommendations.

Various baffling strategies have been proposed, all of them reflective to try to mitigate the pessimistic case of a 3% spillover. These can broadly be split into: elevation structure baffles (all the baffling structure that can be added in the elevation structure to mitigate spillover) and receiver baffles (reflective structures that can be added next to the receiver camera to mitigate spillover).

Elevation structure baffles

Baffling that can be added inside the elevation structure to mitigate spillover include guard rings around the primary-secondary and baffles in the space between the primary-secondary that help redirect rays ending there to the sky.

The baffling structures that have been studied include:

Primary/secondary guards First preliminary study was presented in June 2018. This calculation suggested that having the possibility of extending the size of the mirrors would be beneficial to the spillover characteristics of the system. Though there are practical concerns against the case for primary/secondary baffles such as air flow, weight, and cost, this study was used to recommend Vertex to add mounting points around the primary/secondary that could be added if needed. Note that this recommendation was done with an older camera beam (before our 3% estimate) which predicted more pessimistic sidelobe characteristics. Calculations done with the new beam show we could gain 0.5% power at the sky if we could extend the mirrors as much as possible (see Figures 6.10 and 6.11).

Short Guard Rings This study was done with a model proposed by Vertex having a guard ring made of flat panels of length ~ 50cm. The angle of attack of the model was varied since originally it was too ineffective to send light to the sky. The new angle was set to 7 degrees. An all reflective guard ring showed an improvement of spillover of the order of 0.2%. See Figure 6.1 (right) for more detail.

Receiver baffle

Another baffling strategy that has been studied is the use of a screen around the receiver window. We have studied the case of a parabolic baffle which is helpful at directing rays from the center camera and center pixels to the sky. Variants of this scheme have been proposed due to practical considerations.

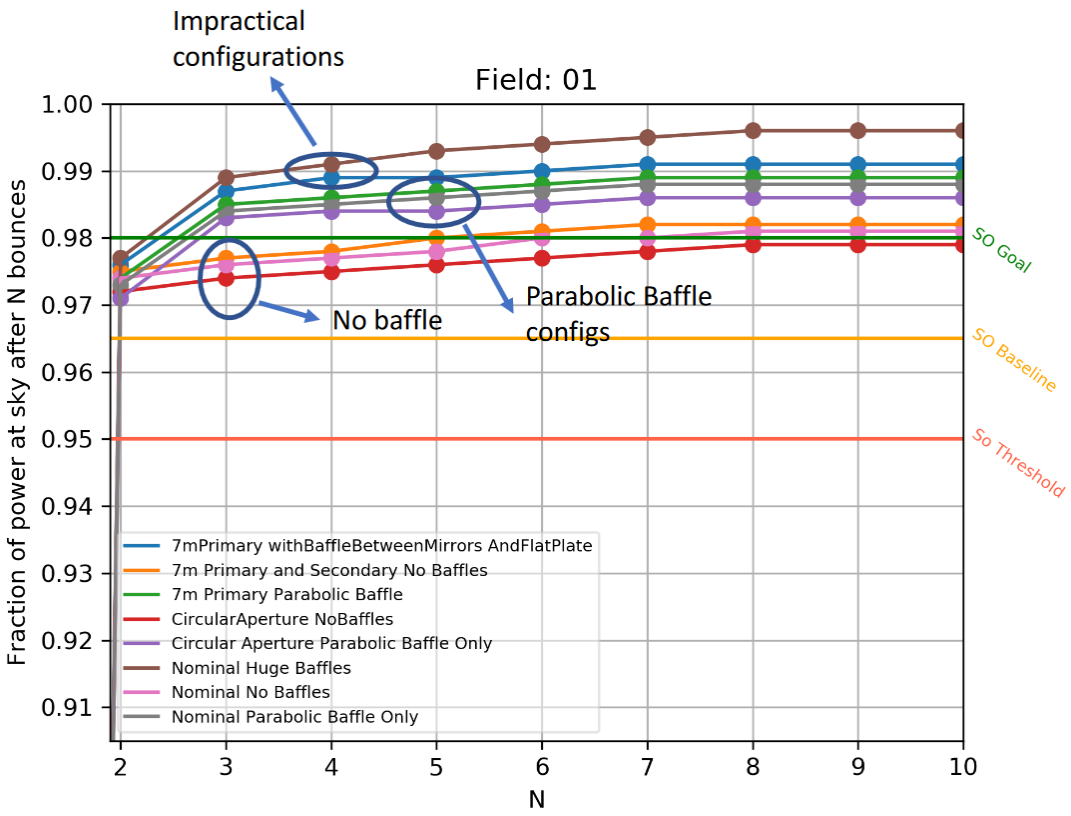

Figure 6.10: Comparison of various baffling configurations. This simulation was carried out with a 3% spillover beam. Configurations labeled 'impractical' have baffles that fill all the available space and have been disfavored for obstructing airflow, weight or cost. Configurations marked as 'No Baffle' show the improvement of extending the mirrors to 7m in diameter (0.5% gain). Configurations marked as 'Parabolic baffle' show the gain of adding a parabolic baffle around the camera entrance aperture in different variants: 7-meter mirrors, circular entrance aperture and the nominal 6m diameter primary.

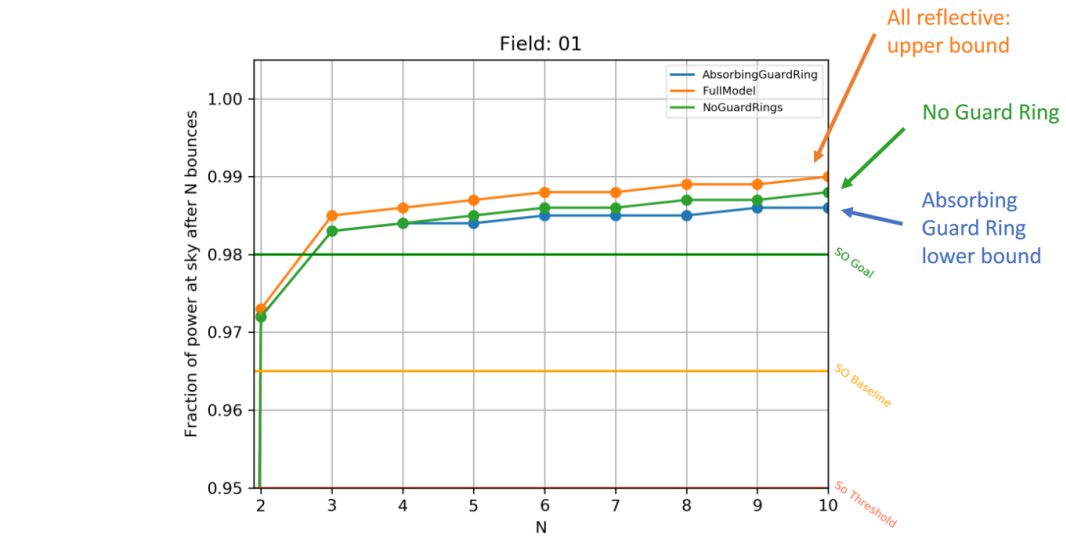

Figure 6.11: (right) Typical performance found simulating a guard ring of 0.5m made of flat panels provided by Vertex. The guard ring angle was varied to 7 degrees to allow light to find its way out of the elevation structure.

Parabolic baffle Simulations showed that including a parabolic baffle around the camera window would be the most efficient way of redirecting spilled light to the sky. Gains here are of order 1% for the center field (see Figure 6.12).

Conical baffle Comparisons of a parabolic vs conical short baffle showed that performance in these configurations is quite similar. With them being equal at the fifth bounce. Details shown in Figure 6.12. Comparisons where the length of the conical baffle is varied tend to prefer a longer baffle that cover all the available space between the camera and the elevation bearing (see Figure 6.14).

Conical segmented baffle Practical considerations lead us to plan building a conical baffle consisting of flat plates. This configuration was disfavored

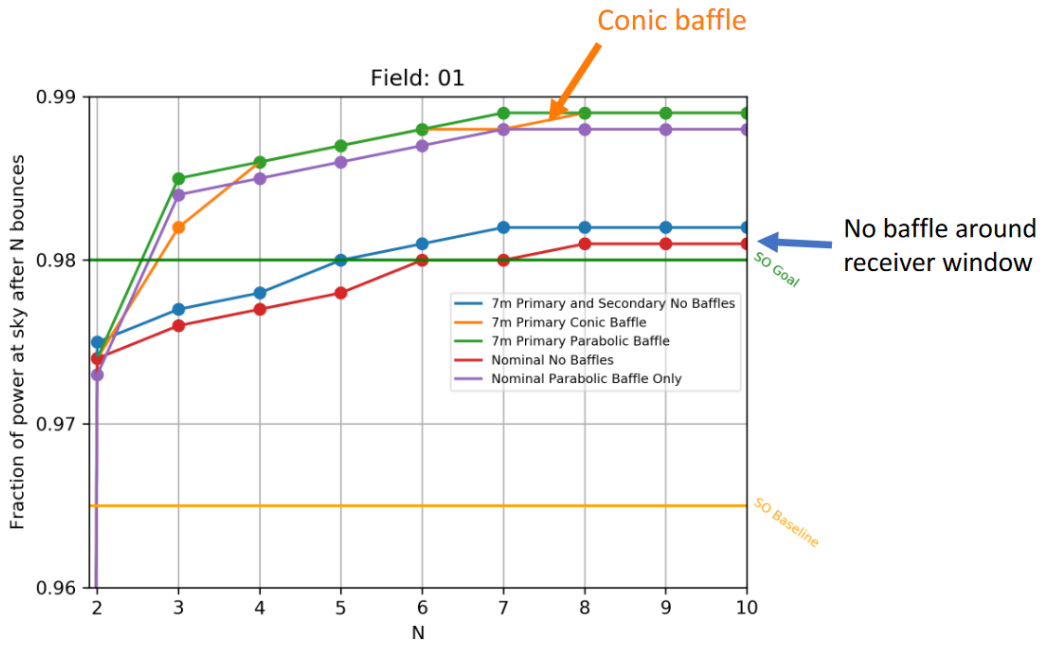

Figure 6.12: Conical and parabolic baffle comparison. Increase in energy at the sky is of order 0.8% compared to a no-baffle model.

after realizing the sidelobe pattern would preserve the symmetry of the broken down baffle at the sky, this segmented sidelobe at the sky would rotate as the telescope changes elevation see Figure 6.13.

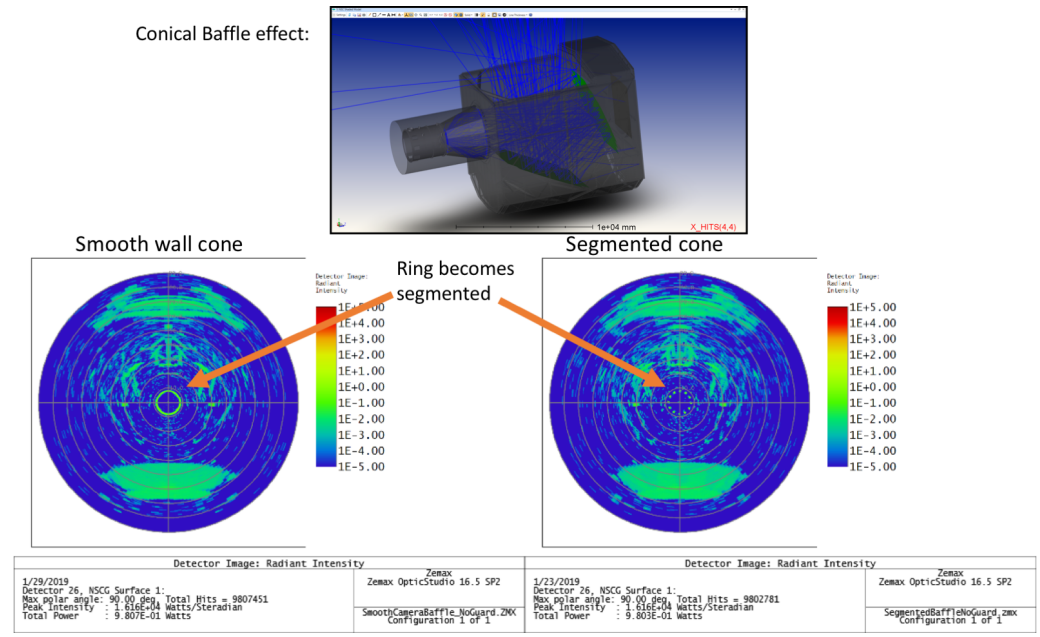

Figure 6.13: Smooth wall baffle produces a ring around 10 degrees from the boresight. The equivalent segmented side baffle produces discrete spots that would vary as the telescope points at different elevations. These spotted ring at the sky would rotate as the telescope changes in elevation.

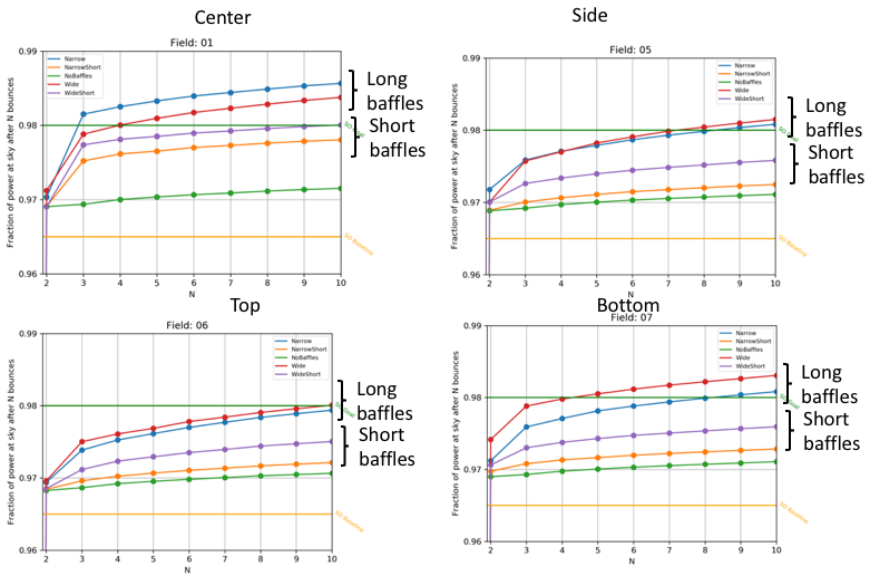

Figure 6.14: Comparison of four baffle designs. The case 'no baffle' is compared against long baffles that cover all the elevation bearing space. Opening angle at the camera exit is varied from a 2 meter aperture for the small side of the cone to a 2.45m meter. All simulations prefer the case with a longer baffle. The narrow baffle is preferred for the center field, while the wide baffle is preferred for the side fields.

6.7 Simons Observatory optical design analyses

In the context of the Simons Observatory, another set of analyses we took part on was the evaluation of optical designs for the large aperture receiver. The optical design of the Simons Observatory is the result of work from many people and is discussed in a set of papers [52, 16, 27]. The design benefited from input from SD, ML, PM, JM, MN, JG (to name a few). Here I show a small subset of that work.

Figure 6.15 shows the Simons Observatory large aperture telescope (right) and its optical path (left). The wide field of view (7.8 degrees) illuminates a two meter tall focal plane. Light from this focal plane is fed into the cryostat (shown on the right) that re-images the focal point onto a cryogenic detector focal plane.

Light from the secondary focuses at the entrance of the receiver window, which features a set of three silicon lenses and a Lyot stop as shown in Figure 6.16. This configuration is the result of 9 optical design iterations we reviewed and evaluated considering different aspects of the optical performance: image quality, optical footprints, F-Numbers, lens curvature, etc. Figure 6.17 shows the result of one of our analyses studying the optical quality of this design. The figure shows the Strehl ratios (a measure of optical quality) for the 13 optics tubes, colored are the areas of diffraction limited performance (Strehl > 0.8). Figure 6.18 shows how the beam ellipticity and beam full width at half maximum (FWHM) are correlated to the Strehl ratio. In this figure JG used Grasp to compute telescope beams using a physical optics calculation and I used a ray trace to compute the Strehl ratios. Results were published in [27].

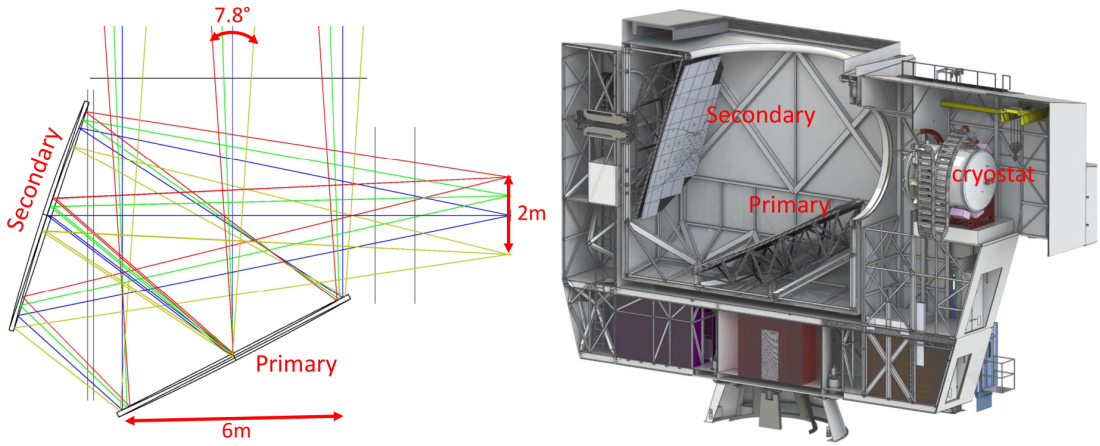

Figure 6.15: (left) Simons Observatory and CCAT-prime large aperture telescope optical design. (right) Simons Observatory large aperture telescope. Note that a field of view of 7.8 degrees is imaged to a 2 meter tall focal plane. This focal plane is then re-imaged by the cold optics onto a cryogenic detector focal plane. Figure taken from [16].

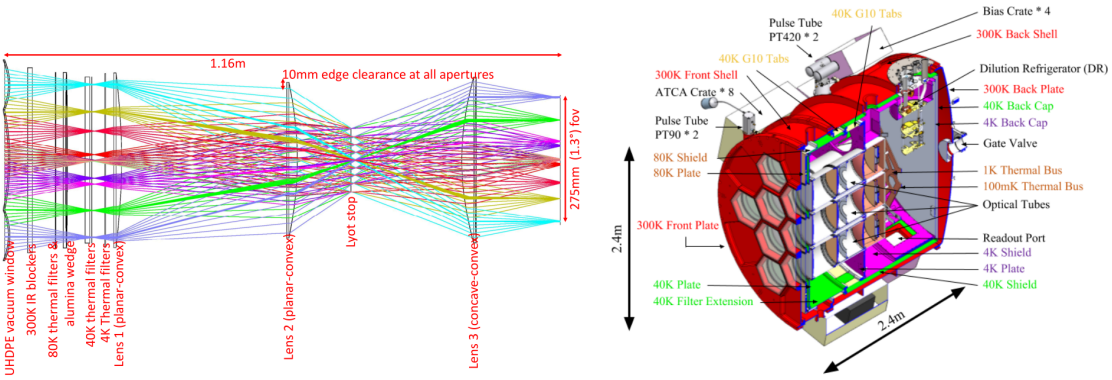

Figure 6.16: (left) The optical path of one of the Simons Observatory large aperture telescope cryogenic cameras. (right) One preliminary mechanical design of the receiver. Figure taken from [16].

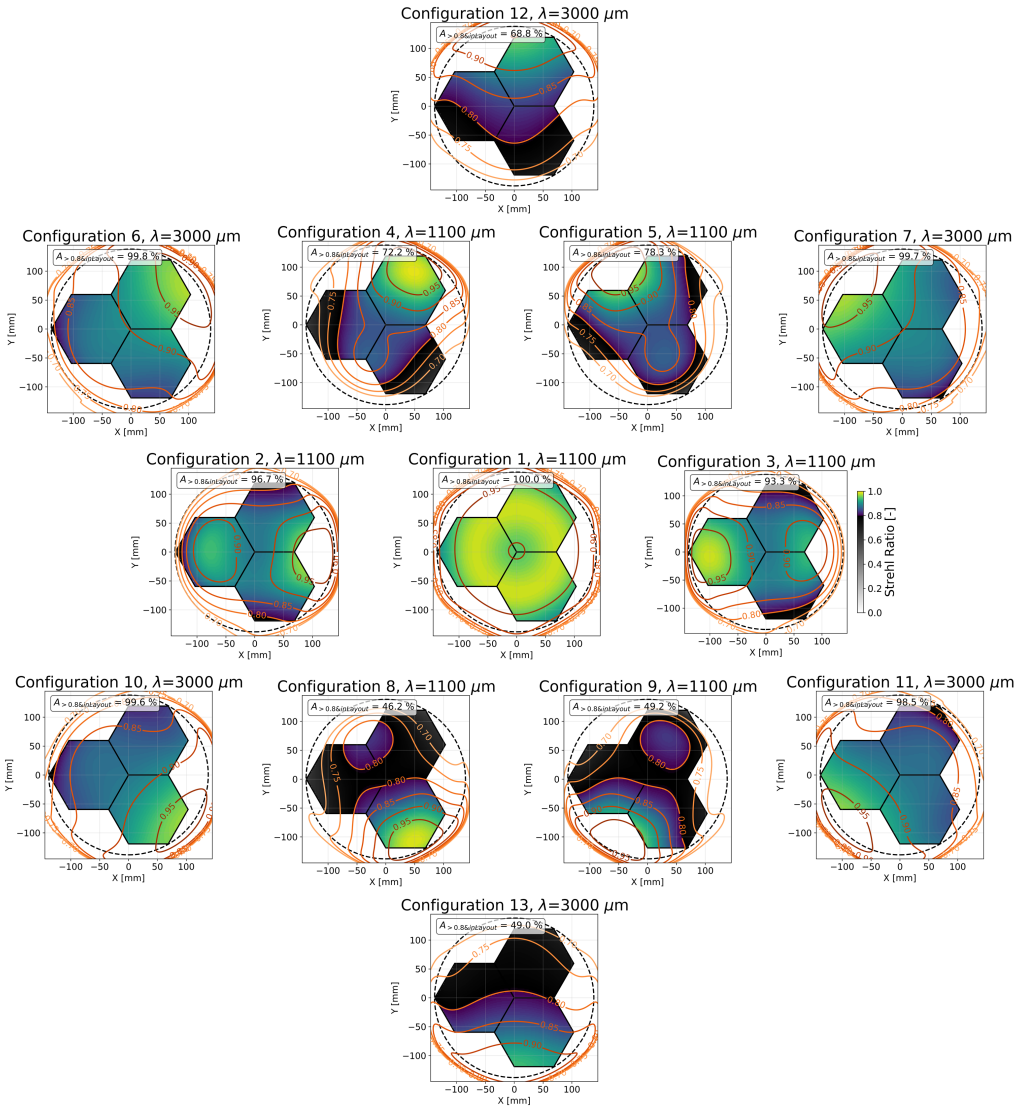

Figure 6.17: Simons Observatory design ID9 optical quality study. Figure shows the Strehl ratio (image quality) for the 13 optics tubes (named configurations). In color the region where diffraction limited performance is expected. Note that the inner tubes show better image quality than the outer tubes. Longer wavelength cameras are located in the periphery for this reason.

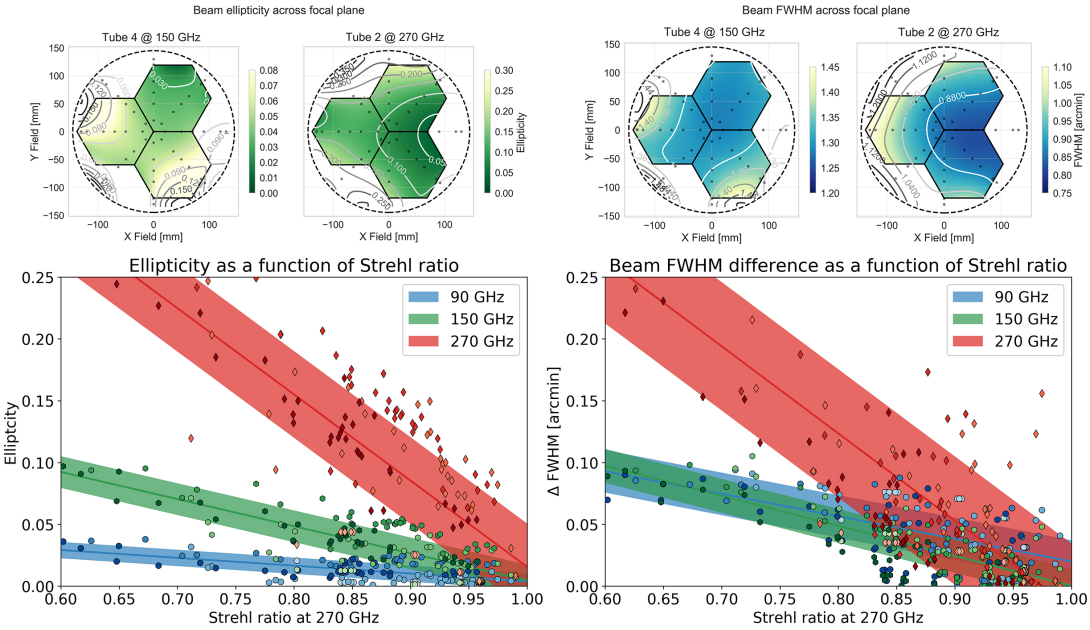

Figure 6.18: Simons Observatory ID9 design beam ellipticity, FWHM and Strehl Ratio comparisons [27]. (top) Beam ellipticity and beam FWHM across the focal plane for tube 2 and 4 at 270 and 150 GHz. (bottom) Correlation between beam ellipticity and FWHM as a function of Strehl ratio across the focal plane. FWHM and beam ellipticity were computed with PO tools, while Strehl ratio was computed with ray tracing.

CHAPTER 7

CONCLUSION

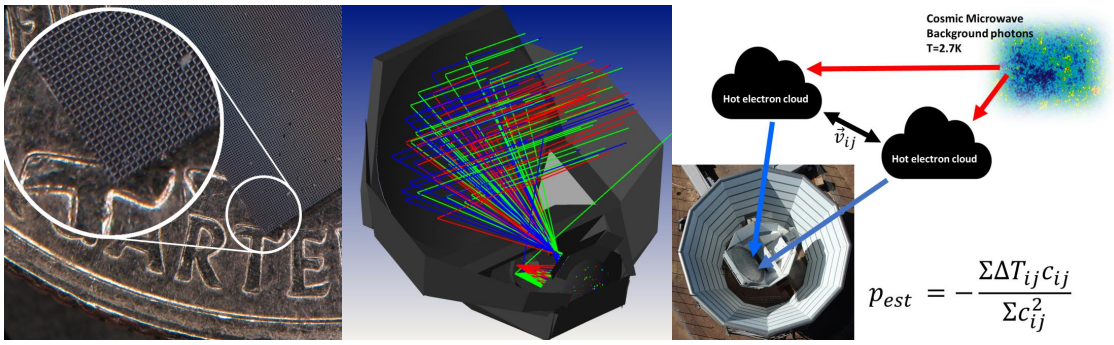

Observational cosmology is at the brink of a great increase of observational power. Current and future CMB experiments will provide volumes of data that have not been achieved before. As the we push the boundaries of sensitivity and coverage of current experiments new technologies are developed that make better use of existing techniques or that open new observational capabilities. I have had the privilege of working developing some of these techniques. Some of these developments through incremental improvements optimize current experiments and set precedent for future instruments. Other developments can be used in ways that have not been explored much to date, opening even more windows for our understanding of our universe through observation from ground based experiments.

In this dissertation I have presented work on a variety of fronts of experimental cosmology. I present work on sub-millimeter optics, optical modeling, detector testing and on large scale kinematics. We have demonstrated a technique to build meta-material anti-reflection coatings that can be used at very high frequencies in the sub-mm part of the spectrum. We measured the noise characteristics in the Advanced ACTPol receiver. We have modeled the optics

and obtained a detailed view of the impact of spillover in large aperture telescopes. Finally we presented measurements of the movements of galaxy clusters with data from the Atacama Cosmology Telescope.

7.1 Silicon deep reactive ion etched meta-material anti-reflection coatings

In millimeter-wave optics silicon is an interesting material as its high index of refraction enables the fabrication of fast lenses. This allows millimeter-wave receivers to be compact and enables high throughput camera optics. The high index of refraction of silicon, however produces reflections that, if left untreated degrade performance. One way of minimizing these reflections is through the use of an anti-reflection coating. Silicon has been used in cosmology experiments like ACTPol and Advanced ACTPol in the millimeter, where meta-material anti-reflection coatings can be fabricated via the use of a silicon dicing saw which cuts sub-wavelength features onto the silicon lens surface allowing the designer choose an effective dielectric constant for the coating.

In the sub-millimeter the fabrication of silicon diced anti-reflection coatings becomes more challenging as more cuts are needed per unit of area (compared to the millimeter regime) which increases the time needed to fabricate a sample.

In chapter 3 I discuss how deep reactive ion etching (DRIE) can be used to fabricate an anti-reflection coating that can be used at THz frequencies in the sub-millimeter. We also explore one technique to bond such a sample to another silicon substrate with minimal loss enabling the fabrication of composite

samples. DRIE is an efficient tool that allows the fabrication of samples rapidly, being useful for large formats or even mass production. This technique could be used also in the industry for millimeter wave communications.

Deep Reactive Ion Etching to build anti-reflection coatings is being used and expanded by NC to be deployed in the Fabry-Perot interferometer for the CCAT-prime telescope. Multi layer coatings are now possible using the DRIE technique and lithography tools are being used to add mesh filters to silicon substrates, expanding the range of applicability of nanofabrication tools to (sub-) millimeter wave optics.

7.2 Optimizing detector noise for Advanced ACTPol

One of the factors that can affect the speed at which one given experiment can map the CMB is detector noise. Aliasing is a phenomenon that adds noise to a detector system in the frequency domain as a consequence of sampling in the time domain. During my PhD studies we tested Advanced ACTPol detector prototypes with time domain multiplexing to determine their stability and measure their aliasing performance. In Chapter 4 we studied the aliasing characteristics of the Advanced ACTPol arrays as they are currently working in the field.

Time domain multiplexing is a mature and well understood multiplexing technology that allows to read thousands of detectors from an array. As the field moves to alternative technologies for reading out even larger numbers of detectors with less wiring like microwave multiplexing, noise characteristics will need to be compared to the state of the art. This study can be one point of

comparison for future performance evaluation and optimization.

7.3 Stray light and sidelobes

Stray light is detrimental to cosmology experiments as it loads the detectors with photon noise from warm surfaces. The projection of the stray light pattern on the sky via bounces on the telescope structure creates sidelobes, which are off-axis regions of the sky where the telescope can receive light (though attenuated by a factor of tens of millions). Sidelobes and their interaction with warm light around the scanning telescope introduce scan synchronous signals that need to be removed during the map making process.

In this work we have shown that the sidelobe pattern for a large aperture telescope is a consequence of the interaction of the camera stray light pattern and the telescope comoving structure. We also use the techniques here developed to make predictions of the sidelobe patterns of the Simons Observatory and CCAT-prime. In addition we use these calculations to develop baffling strategies to minimize loading.

In the future, the addition of Physical Optics tools will be of great value as we will be able to provide more detailed design metrics as ground pickup level or panel gap diffraction which will help planning the next generation of CMB telescopes, CMB-Stage 4.

7.4 Pairwise kSZ

In Chapter 5 we discussed the use of ACT data to improve measurements of the motions of clusters of galaxies through the use of the pairwise kinetic Sunyaev Zeldovich effect (kSZ). The kSZ effect is the Doppler shift of the inverse Compton scattered light from the CMB on the hot gas surrounding clusters of galaxies. This effect is small and study of the statistical properties of the estimator is important. The first detection with ACT data of the pairwise kSZ signal was presented in [32] and a second detection with higher confidence was done in [14], in this work we expand this work with yet higher confidence and larger sky coverage.

We have developed tools for estimating the pairwise kSZ decrement for a large patch of sky with samples of up to hundreds of thousands of galaxies, which was one limitation of previous studies. Work presented here was done in close collaboration with VC and EV. Results from these studies are being prepared for submission in two papers; one focused on the detection of the effect and another on estimates of τ from the kinetic as well as the thermal SZ effects.

Measurements of the pairwise kSZ effect continue to be refined and high precision measurements of the streaming velocities of clusters of galaxies are being used to probe the dynamics of the large scale structure of the universe. In the future precise measurements of the kinetic SZ effect will enable cosmological probes like tests of modified gravity theories or expansions to current models like tighter constraints on the sum of the neutrino masses.

BIBLIOGRAPHY

[1] PAR Ade, Y Akiba, AE Anthony, K Arnold, M Atlas, D Barron, D Boettger, J Borrill, S Chapman, and Y Chinone. A measurement of the cosmic microwave background B-mode polarization power spectrum at sub-degree scales with POLARBEAR. *The Astrophysical Journal*, 794(2):171, 2014.

[2] Peter AR Ade, N Aghanim, M Arnaud, M Ashdown, J Aumont, C Baccigalupi, AJ Banday, RB Barreiro, JG Bartlett, and N Bartolo. Planck 2015 results-xiii. cosmological parameters. *Astronomy & Astrophysics*, 594:A13, 2016.

[3] Peter AR Ade, Z Ahmed, RW Aikin, Kate Denham Alexander, D Barkats, SJ Benton, Colin A Bischoff, JJ Bock, JA Brevik, and I Buder. BICEP2/Keck array V: Measurements of B-mode polarization at degree angular scales and 150 GHz by the Keck array. *The Astrophysical Journal*, 811(2):126, 2015.

[4] Kazunori Akiyama. First M87 Event Horizon Telescope Results. I. The Shadow of the Supermassive Black Hole. *The Astrophysical Journal Letters*, page 17, 2019.

[5] A. J. Anderson, P. A. R. Ade, Z. Ahmed, J. E. Austermann, J. S. Avva, P. S. Barry, R. Basu Thakur, A. N. Bender, B. A. Benson, L. E. Bleem, K. Byrum, J. E. Carlstrom, F. W. Carter, T. Cecil, C. L. Chang, H. M. Cho, J. F. Cliche, T. M. Crawford, A. Cukierman, E. V. Denison, T. de Haan, J. Ding, M. A. Dobbs, D. Dutcher, W. Everett, A. Foster, R. N. Gannon, A. Gilbert, J. C. Groh, N. W. Halverson, A. H. Harke-Hosemann, N. L. Harrington, J. W. Henning, G. C. Hilton, G. P. Holder, W. L. Holzapfel, N. Huang, K. D. Irwin, O. B. Jeong, M. Jonas, T. Khaire, L. Knox, A. M. Kofman, M. Korman, D. Kubik, S. Kuhlmann, N. Kuklev, C. L. Kuo, A. T. Lee, E. M. Leitch, A. E. Lowitz, S. S. Meyer, D. Michalik, J. Montgomery, A. Nadolski, T. Natoli, H. Nguyen, G. I. Noble, V. Novosad, S. Padin, Z. Pan, J. Pearson, C. M. Posada, A. Rahlin, C. L. Reichardt, J. E. Ruhl, L. J. Saunders, J. T. Sayre, I. Shirley, E. Shirokoff, G. Smecher, J. A. Sobrin, A. A. Stark, K. T. Story, A. Suzuki, Q. Y. Tang, K. L. Thompson, C. Tucker, L. R. Vale, K. Vanderlinde, J. D. Vieira, G. Wang, N. Whitehorn, V. Yefremenko, K. W. Yoon, and M. R. Young. SPT-3g: A Multichroic Receiver for the South Pole Telescope. *Journal of Low Temperature Physics*, 193(5):1057–1065, December 2018.

[6] F. De Bernardis, S. Aiola, E. M. Vavagiakis, N. Battaglia, M. D. Niemack, J. Beall, D. T. Becker, J. R. Bond, E. Calabrese, H. Cho, K. Coughlin, R. Datta, M. Devlin, J. Dunkley, R. Dunner, S. Ferraro, A. Fox, P.A. Gallardo, M. Halpern, N. Hand, M. Hasselfield, S. W. Henderson, J. C. Hill,

G. C. Hilton, M. Hilton, A.D. Hincks, R. Hlozek, J. Hubmayr, K. Huffenberger, J. P. Hughes, K. D. Irwin, B. J. Koopman, A. Kosowsky, D. Li, T. Louis, M. Lungu, M. S. Madhavacheril, L. Maurin, J. McMahon, K. Moodley, S. Naess, F. Nati, L. Newburgh, J.P. Nibarger, L. A. Page, B. Partridge, E. Schaan, B. L. Schmitt, N. Sehgal, J. Sievers, S. M. Simon, D.N. Spergel, S. T. Staggs, J. R. Stevens, R. J. Thornton, A. van Engelen, J. Van Lanen, and E. J. Wollack. Detection of the pairwise kinematic Sunyaev-Zel'dovich effect with BOSS DR11 and the Atacama Cosmology Telescope. *Journal of Cosmology and Astroparticle Physics*, 2017(03):008, 2017.

[7] S. Biber, J. Richter, S. Martius, and L. P. Schmidt. Design of Artificial Dielectrics for Anti-Reflection-Coatings. In *Microwave Conference, 2003 33rd European*, pages 1115–1118, October 2003.

[8] Keck Array Collaboration BICEP and PAR Ade. BICEP2/Keck Array VI: Improved Constraints On Cosmology and Foregrounds When Adding 95 GHz Data From Keck Array. *arXiv preprint arXiv:1510.09217*, 2016.

[9] Michael R Blanton and Sam Roweis. K-corrections and filter transformations in the ultraviolet, optical, and near-infrared. *The Astronomical Journal*, 133(2):734, 2007.

[10] S. H. Christiansen, R. Singh, and U. Gosele. Wafer Direct Bonding: From Advanced Substrate Engineering to Future Applications in Micro/Nanoelectronics. *Proceedings of the IEEE*, 94(12):2060–2106, December 2006.

[11] The LIGO Scientific Collaboration and the Virgo Collaboration. Observation of Gravitational Waves from a Binary Black Hole Merger. *Physical Review Letters*, 116(6), February 2016. arXiv: 1602.03837.

[12] Nicholas F Cothard, Mahiro Abe, Thomas Nikola, Gordon J Stacey, German Cortes-Medellin, Patricio A Gallardo, Brian J Koopman, Michael D Niemack, Stephen C Parshley, and Eve M Vavagiakis. Optimizing the efficiency of Fabry-Perot interferometers with silicon-substrate mirrors. In *International Society for Optics and Photonics*, volume 10706, page 107065B. International Society for Optics and Photonics, 2018.

[13] R Datta, CD Munson, MD Niemack, JJ McMahon, J Britton, Edward J Wollack, J Beall, MJ Devlin, J Fowler, and P Gallardo. Large-aperture wideband antireflection-coated silicon lenses for millimeter wavelengths. *Applied optics*, 52(36):8747–8758, 2013.

[14] Francesco De Bernardis, S Aiola, EM Vavagiakis, N Battaglia, MD Niemack, J Beall, DT Becker, JR Bond, E Calabrese, and H Cho. Detection of the pairwise kinematic Sunyaev-Zel'dovich effect with BOSS DR11 and the Atacama Cosmology Telescope. *Journal of Cosmology and Astroparticle Physics*, 2017(03):008, 2017.

[15] Robert H Dicke, P James E Peebles, Peter G Roll, and David T Wilkinson. Cosmic Black-Body Radiation. *The Astrophysical Journal*, 142:414–419, 1965.

[16] SR Dicker, PA Gallardo, JE Gudmudsson, PD Mauskopf, A Ali, PC Ashton, G Coppi, MJ Devlin, N Galitzki, and SP Ho. Cold optical design for the large aperture Simons' Observatory telescope. In *SPIE*, volume 10700, page 107003E. International Society for Optics and Photonics, 2018.

[17] Scott Dodelson. *Modern cosmology*. Elsevier, 2003.

[18] Shannon M Duff, J Austermann, JA Beall, D Becker, R Datta, PA Gallardo, SW Henderson, GC Hilton, SP Ho, and J Hubmayr. Advanced actpol multichroic polarimeter array fabrication process for 150 mm wafers. *Journal of Low Temperature Physics*, 184(3-4):634–641, 2016.

[19] Rolando Dunner, Matthew Hasselfield, Tobias A Marriage, Jon Sievers, Viviana Acquaviva, Graeme E Addison, Peter AR Ade, Paula Aguirre, Mandana Amiri, and John William Appel. The Atacama cosmology telescope: Data characterization and mapmaking. *The Astrophysical Journal*, 762(1):10, 2012.

[20] Bradley Efron and Trevor Hastie. *Computer age statistical inference*, volume 5. Cambridge University Press, 2016.

[21] esa. History of cosmic structure formation / Planck / Space Science / Our Activities / ESA.

[22] P. G. Ferreira, R. Juszkiewicz, H. A. Feldman, M. Davis, and A. H. Jaffe. Streaming Velocities as a Dynamical Estimator of . *The Astrophysical Journal*, 515(1):L1–L4, April 1999.

[23] DJ Fixsen, ES Cheng, JM Gales, John C Mather, RA Shafer, and EL Wright. The cosmic microwave background spectrum from the full cobe* firas data set. *The Astrophysical Journal*, 473(2):576, 1996.

[24] Pedro Antonio Fluxa, Rolando Dnner, Loc Maurin, Steve K Choi, Mark J

Devlin, Patricio A Gallardo, Shuay-Pwu P Ho, Brian J Koopman, Thibaut Louis, and Jeffrey J McMahon. Far sidelobe effects from panel gaps of the Atacama Cosmology Telescope. In *SPIE*, volume 9914, page 99142Q. International Society for Optics and Photonics, 2016.

[25] Patricio Gallardo, Rolando Dunner, Edward Wollack, Fernando Henriquez, and Carlos Jerez-Hanckes. Mirror illumination and spillover measurements of the Atacama Cosmology Telescope. In Wayne S. Holland, editor, *SPIE*, page 845224, September 2012.

[26] Patricio A Gallardo, Nicholas F Cothard, Roberto Puddu, Rolando Dunner, Brian J Koopman, Michael D Niemack, Sara M Simon, and Edward J Wollack. Far sidelobes from baffles and telescope support structures in the Atacama Cosmology Telescope. In *SPIE*, volume 10708, page 107082L. International Society for Optics and Photonics, 2018.

[27] Patricio A Gallardo, Jon Gudmundsson, Brian J Koopman, Frederick T Matsuda, Sara M Simon, Aamir Ali, Sean Bryan, Yuji Chinone, Gabriele Coppi, and Nicholas Cothard. Systematic uncertainties in the Simons Observatory: optical effects and sensitivity considerations. In *SPIE*, volume 10708, page 107083Y. International Society for Optics and Photonics, 2018.

[28] Patricio A Gallardo, Brian J Koopman, Nicholas F Cothard, Sarah Marie M Bruno, German Cortes-Medellin, Galen Marchetti, Kevin H Miller, Brenna Mockler, Michael D Niemack, and Gordon Stacey. Deep reactive ion etched anti-reflection coatings for sub-millimeter silicon optics. *Applied optics*, 56(10):2796–2803, 2017.

[29] Ronald Gelaro, Will McCarty, Max J Surez, Ricardo Todling, Andrea Molod, Lawrence Takacs, Cynthia A Randles, Anton Darmenov, Michael G Bosilovich, and Rolf Reichle. The modern-era retrospective analysis for research and applications, version 2 (MERRA-2). *Journal of Climate*, 30(14):5419–5454, 2017.

[30] Guan, Yilun, and Fernando Zago. In prep. –, 56(10):tbd, 2019.

[31] U Gsele and Q-Y Tong. Semiconductor wafer bonding. *Annual review of materials science*, 28(1):215–241, 1998.

[32] Nick Hand, Graeme E Addison, Eric Aubourg, Nick Battaglia, Elia S Battistelli, Dmitry Bizyaev, J Richard Bond, Howard Brewington, Jon Brinkmann, and Benjamin R Brown. Evidence of galaxy cluster mo-

tions with the kinematic Sunyaev-Zeldovich effect. *Physical Review Letters*, 109(4):041101, 2012.

[33] Eugene Hecht. *Optics*. Addison-Wesley, Reading, Mass., 3rd ed. edition, 1998.

[34] S. W. Henderson, R. Allison, J. Austermann, T. Baildon, N. Battaglia, J. A. Beall, D. Becker, F. De Bernardis, J. R. Bond, E. Calabrese, S. K. Choi, K. P. Coughlin, K. T. Crowley, R. Datta, M. J. Devlin, S. M. Duff, J. Dunkley, R. Dnner, A. van Engelen, P. A. Gallardo, E. Grace, M. Hasselfield, F. Hills, G. C. Hilton, A. D. Hincks, R. Hlozek, S. P. Ho, J. Hubmayr, K. Huffenberger, J. P. Hughes, K. D. Irwin, B. J. Koopman, A. B. Kosowsky, D. Li, J. McMahon, C. Munson, F. Nati, L. Newburgh, M. D. Niemack, P. Niraula, L. A. Page, C. G. Pappas, M. Salatino, A. Schillaci, B. L. Schmitt, N. Sehgal, B. D. Sherwin, J. L. Sievers, S. M. Simon, D. N. Spergel, S. T. Staggs, J. R. Stevens, R. Thornton, J. Van Lanen, E. M. Vavagiakis, J. T. Ward, and E. J. Wollack. Advanced ACTPol Cryogenic Detector Arrays and Readout. *Journal of Low Temperature Physics*, 184(3-4):772–779, March 2016.

[35] Shawn W Henderson, Zeeshan Ahmed, Jason Austermann, Daniel Becker, Douglas A Bennett, David Brown, Saptarshi Chaudhuri, Hsiao-Mei Sherry Cho, John M D'Ewart, and Bradley Dober. Highly-multiplexed microwave SQUID readout using the SLAC microresonator radio frequency (SMuRF) electronics for future CMB and sub-millimeter surveys. In *Millimeter, Submillimeter, and Far-Infrared Detectors and Instrumentation for Astronomy IX*, volume 10708, page 1070819. International Society for Optics and Photonics, 2018.

[36] Shawn W Henderson, Jason R Stevens, Mandana Amiri, Jason Austermann, James A Beall, Saptarshi Chaudhuri, Hsiao-Mei Cho, Steve K Choi, Nicholas F Cothard, and Kevin T Crowley. Readout of two-kilopixel transition-edge sensor arrays for Advanced ACTPol. In *Millimeter, Submillimeter, and Far-Infrared Detectors and Instrumentation for Astronomy VIII*, volume 9914, page 99141G. International Society for Optics and Photonics, 2016.

[37] Charles A Hill, Sarah Marie M Bruno, Sara M Simon, Aamir Ali, Kam S Arnold, Peter C Ashton, Darcy Barron, Sean Bryan, Yuji Chinone, and Gabriele Coppi. BoloCalc: a sensitivity calculator for the design of Simons Observatory. In *Millimeter, Submillimeter, and Far-Infrared Detectors and Instrumentation for Astronomy IX*, volume 10708, page 1070842. International Society for Optics and Photonics, 2018.

[38] Matt Hilton, Matthew Hasselfield, Cristbal Sifn, Nicholas Battaglia, Simone Aiola, V Bharadwaj, J Richard Bond, Steve K Choi, Devin Crichton, and Rahul Datta. The Atacama Cosmology Telescope: the two-season ACTPol SunyaevZeldovich effect selected cluster catalog. *The Astrophysical Journal Supplement Series*, 235(1):20, 2018.

[39] Wayne Hu and Scott Dodelson. Cosmic microwave background anisotropies. *Annual Review of Astronomy and Astrophysics*, 40(1):171–216, 2002.

[40] Bernd Jhne. Digital Image Processing 5th revised and extended edition. *Berlin: Springer-Verlag, doi*, 10:3–540, 2002.

[41] R Keisler, S Hoover, N Harrington, JW Henning, PAR Ade, KA Aird, JE Austermann, JA Beall, AN Bender, and BA Benson. Measurements of sub-degree B-mode polarization in the cosmic microwave background from 100 square degrees of SPTpol data. *The Astrophysical Journal*, 807(2):151, 2015.

[42] Siu Kwan Lam, Antoine Pitrou, and Stanley Seibert. Numba: A llvm-based python jit compiler. In *Proceedings of the Second Workshop on the LLVM Compiler Infrastructure in HPC*, page 7. ACM, 2015.

[43] LIGO Scientific Collaboration, Virgo Collaboration, 1M2H Collaboration, Dark Energy Camera GW-EM Collaboration, DES Collaboration, DLT40 Collaboration, Las Cumbres Observatory Collaboration, VINROUGE Collaboration, and MASTER Collaboration. A gravitational-wave standard siren measurement of the Hubble constant. *Nature*, 551(7678):85–88, 2017.

[44] Thibaut Louis, Emily Grace, Matthew Hasselfield, Marius Lungu, Loc Maurin, Graeme E. Addison, Peter A. R. Ade, Simone Aiola, Rupert Allison, Mandana Amiri, Elio Angile, Nicholas Battaglia, James A. Beall, Francesco de Bernardis, J. Richard Bond, Joe Britton, Erminia Calabrese, Hsiao-mei Cho, Steve K. Choi, Kevin Coughlin, Devin Crichton, Kevin Crowley, Rahul Datta, Mark J. Devlin, Simon R. Dicker, Joanna Dunkley, Rolando Dnner, Simone Ferraro, Anna E. Fox, Patricio Gallardo, Megan Gralla, Mark Halpern, Shawn Henderson, J. Colin Hill, Gene C. Hilton, Matt Hilton, Adam D. Hincks, Rene Hlozek, S. P. Patty Ho, Zhiqi Huang, Johannes Hubmayr, Kevin M. Huffenberger, John P. Hughes, Leopoldo Infante, Kent Irwin, Simon Muya Kasanda, Jeff Klein, Brian Koopman, Arthur Kosowsky, Dale Li, Mathew Madhavacheril, Tobias A. Marriage, Jeff McMahon, Felipe Menanteau, Kavilan Moodley, Charles Munson, Sigurd Naess, Federico Nati, Laura Newburgh, John Nibarger, Michael D.

Niemack, Michael R. Nolta, Carolina Nunez, Lyman A. Page, Christine Pappas, Bruce Partridge, Felipe Rojas, Emmanuel Schaan, Benjamin L. Schmitt, Neelima Sehgal, Blake D. Sherwin, Jon Sievers, Sara Simon, David N. Spergel, Suzanne T. Staggs, Eric R. Switzer, Robert Thornton, Hy Trac, Jesse Treu, Carole Tucker, Alexander Van Engelen, Jonathan T. Ward, and Edward J. Wollack. The Atacama Cosmology Telescope: Two-Season ACTPol Spectra and Parameters. *Journal of Cosmology and Astroparticle Physics*, 2017(06):031–031, June 2017. arXiv: 1610.02360.

[45] Felipe Menanteau, Jorge Gonzlez, Jean-Baptiste Juin, Tobias A Marriage, Erik D Reese, Viviana Acquaviva, Paula Aguirre, John William Appel, Andrew J Baker, and L Felipe Barrientos. The Atacama Cosmology Telescope: Physical properties and purity of a galaxy cluster sample selected via the Sunyaev-Zel'dovich effect. *The Astrophysical Journal*, 723(2):1523, 2010.

[46] Eva-Maria Mueller, Francesco De Bernardis, Rachel Bean, and Michael D Niemack. Constraints on gravity and dark energy from the pairwise kinematic sunyaevzeldovich effect. *The Astrophysical Journal*, 808(1):47, 2015.

[47] Naes and Sigurd. In prep. *tbd*, –(1):tbd, 2019.

[48] Sigurd Naess. A rectangular pixel map manipulation and harmonic analysis library derived from Sigurd Naess' enlib.: simonsobs/pixell, July 2019. original-date: 2018-05-17T22:59:16Z.

[49] NASA. LAMBDA - Legacy Archive for Microwave Background Data.

[50] Sigurd Kirkevold Nss. *Maximum likelihood analysis with the Q/U Imaging ExperimenT*. PhD thesis, University of Oslo, 2012.

[51] Alan V. Oppenheim. *Signals & systems*. Prentice Hall, Upper Saddle River, N.J., 2nd ed. edition, 1997.

[52] Stephen C. Parshley, Michael Niemack, Richard Hills, Simon R. Dicker, Rolando Dnner, Jens Erler, Patricio A. Gallardo, Jon E. Gudmundsson, Terry Herter, Brian J. Koopman, Michele Limon, Frederick T. Matsuda, Philip Mauskopf, Dominik A. Riechers, Gordon J. Stacey, and Eve M. Vavagiakis. The optical design of the six-meter CCAT-prime and Simons Observatory telescopes. In *Ground-based and Airborne Telescopes VII*, volume 10700, page 1070041. International Society for Optics and Photonics, July 2018.

[53] Arno A Penzias and Robert Woodrow Wilson. A measurement of excess antenna temperature at 4080 Mc/s. *The Astrophysical Journal*, 142:419–421, 1965.

[54] Adam G Riess, Stefano Casertano, Wenlong Yuan, Lucas M Macri, and Dan Scolnic. Large Magellanic Cloud Cepheid Standards Provide a 1% Foundation for the Determination of the Hubble Constant and Stronger Evidence for Physics Beyond CDM. *The Astrophysical Journal*, 876(1):85, 2019.

[55] Matthew Rocklin. Dask: Parallel computation with blocked algorithms and task scheduling. In *python in science conference*. Citeseer, 2015.

[56] Barbara Ryden. *Introduction to cosmology*. Cambridge University Press, 2017.

[57] Dorothea Samtleben, Suzanne Staggs, and Bruce Winstein. The cosmic microwave background for pedestrians: A review for particle and nuclear physicists. *Annu. Rev. Nucl. Part. Sci.*, 57:245–283, 2007.

[58] R. Stengl, K.-Y. Ahn, and U. Gsele. Bubble-Free Silicon Wafer Bonding in a Non-Cleanroom Environment. *Japanese Journal of Applied Physics*, 27(Part 2, No. 12):L2364–L2366, December 1988.

[59] D. S. Swetz, P. A. R. Ade, M. Amiri, J. W. Appel, E. S. Battistelli, B. Burger, J. Chervenak, M. J. Devlin, S. R. Dicker, W. B. Doriese, R. Dunner, T. Essinger-Hileman, R. P. Fisher, J. W. Fowler, M. Halpern, M. Hasselfield, G. C. Hilton, A. D. Hincks, K. D. Irwin, N. Jarosik, M. Kaul, J. Klein, J. M. Lau, M. Limon, T. A. Marriage, D. Marsden, K. Martocci, P. Mauskopf, H. Moseley, C. B. Netterfield, M. D. Niemack, M. R. Nolta, L. A. Page, L. Parker, S. T. Staggs, O. Stryzak, E. R. Switzer, R. Thornton, C. Tucker, E. Wollack, and Y. Zhao. The Atacama Cosmology Telescope: The Receiver and Instrumentation. *The Astrophysical Journal Supplement Series*, 194(2):41, June 2011. arXiv: 1007.0290.

[60] R. J. Thornton, P. A. R. Ade, S. Aiola, F. E. Angile, M. Amiri, J. A. Beall, D. T. Becker, H.-M. Cho, S. K. Choi, P. Corlies, K. P. Coughlin, R. Datta, M. J. Devlin, S. R. Dicker, R. Dunner, J. W. Fowler, A. E. Fox, P. A. Gallardo, J. Gao, E. Grace, M. Halpern, M. Hasselfield, S. W. Henderson, G. C. Hilton, A. D. Hincks, S. P. Ho, J. Hubmayr, K. D. Irwin, J. Klein, B. Koopman, Dale Li, T. Louis, M. Lungu, L. Maurin, J. McMahon, C. D. Munson, S. Naess, F. Nati, L. Newburgh, J. Nibarger, M. D. Niemack, P. Niraula, M. R. Nolta, L. A. Page, C. G. Pappas, A. Schillaci, B. L. Schmitt, N. Sehgal, J. L. Sievers, S. M. Simon, S. T. Staggs, C. Tucker, M. Uehara, J. van Lanen, J. T. Ward,

and E. J. Wollack. The Atacama Cosmology Telescope: The polarization-sensitive ACTPol instrument. *arXiv:1605.06569 [astro-ph]*, May 2016. arXiv: 1605.06569.

[61] Wikipedia. I/O bound, March 2019. Page Version ID: 887663727.

[62] Kenneth C Wong, Sherry H Suyu, Geoff C-F Chen, Cristian E Rusu, Martin Millon, Dominique Sluse, Vivien Bonvin, Christopher D Fassnacht, Stefan Taubenberger, and Matthew W Auger. H0licow XIII. A 2.4% measurement of H0 from lensed quasars: 5.3 sigma tension between early and late-Universe probes. *arXiv preprint arXiv:1907.04869*, 2019.

[63] Banqiu Wu, Ajay Kumar, and Sharma Pamarthy. High aspect ratio silicon etch: A review. *Journal of applied physics*, 108(5):9, 2010.

[64] Pochi Yeh. *Optical waves in layered media*. Wiley series in pure and applied optics. Wiley, New York, 1988.

[65] Donald G York, J Adelman, John E Anderson Jr, Scott F Anderson, James Annis, Neta A Bahcall, JA Bakken, Robert Barkhouser, Steven Bastian, and Eileen Berman. The sloan digital sky survey: Technical summary. *The Astronomical Journal*, 120(3):1579, 2000.

[66] Ya. B. Zeldovich and R. A. Sunyaev. The interaction of matter and radiation in a hot-model universe. *Astrophysics and Space Science*, 4(3):301–316, July 1969.